Technische Universität München
TUM School of Natural Sciences

Electronic Couplings from Density Functional Theory: Quantitative Approaches

Simiam Andreas Ghan

Dissertation

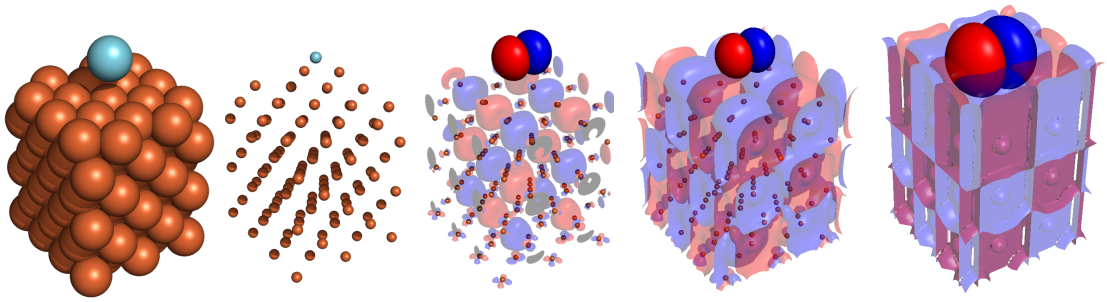

Technische Universität München
TUM School of Natural Sciences

Electronic Couplings from Density Functional Theory: Quantitative Approaches

Simiam Andreas Ghan

Vollständiger Abdruck der von der TUM School of Natural Sciences der Technischen Universität München zur Erlangung des akademischen Grades eines

Doktors der Naturwissenschaften (Dr. rer. nat.)

genehmigten Dissertation.

Vorsitz: Priv.-Doz. Dr. Friedrich Esch

Prüfer*innen der Dissertation:

1. Prof. Dr. Karsten Reuter
2. Prof. Dr. Christopher Stein

Die Dissertation wurde am 22.05.2023 bei der Technischen Universität München eingereicht und durch die TUM School of Natural Sciences am 22.06.2023 angenommen.

Cover Image: Orbital representation of an adatom on (in) a surface.

Prédire n'est pas expliquer/To predict is not to explain.

–René Thom–

Preface

This doctoral thesis summarizes work begun in the Chair of Theoretical Chemistry of the Technical University of Munich TUM (2017-2021) and continued at the Fritz-Haber Institute of the Max-Planck Society, Berlin (2021-2023) under the supervision of Prof. Dr. Karsten Reuter. Parts of this dissertation have been published before in Reference [1] and other parts have been submitted for publication as Reference [2].

Berlin, May 2023

Simiam Ghan

Abstract

This work addresses the calculation of electronic coupling parameters H_{ad} from Kohn-Sham Density Functional Theory (DFT). Although ubiquitous in theoretical descriptions, electronic coupling matrix elements are challenging to calculate in practice due to their non-observable nature and formally non-unique definition. As a result, H_{ad} are often approximated and used qualitatively. Extracting electronic couplings from DFT requires a projection of the *adiabatic* electronic structure onto localized *diabatic* fragments. In the context of charge transfer, this localization procedure is known as diabatization. While numerous diabatization schemes have been developed for the study of e.g. charge hopping between pairs of molecules, electronic coupling on surfaces has been less well explored.

In this work, we concern ourselves with a method called Projection-Operator Diabatization (POD). Similar to other local projections of DFT, such as Mulliken partial charge analysis, the original POD method suffers from instability with respect to the atomic orbital basis set. By first modifying this with a Gram-Schmidt (GS) orthogonalization procedure, we provide an improved method (POD2GS) which is demonstrated with the Hab11 benchmark of molecular dimers. Next, we develop similar diabatization methods for adsorbates on surfaces. We validate these methods by calculating ultrafast electron transfer lifetimes for core-excited Argon adsorbates on transition metal surfaces. For this, we use the couplings to construct a first-principles Newns-Anderson chemisorption function, a coupling-weighted density of states (WDOS) which gives the line broadening of an adsorbate frontier orbital on a surface. This line broadening is interpreted as an ultrafast electron transfer lifetime with Fermi's Golden Rule, yielding results in excellent agreement with experiment.

The use of first-principles electronic couplings within a Newns-Anderson chemisorption function is found to be highly advantageous. The chemisorption function is highly interpretable, containing rich information on the phase and symmetry of interacting orbitals and their role in the electron transfer. Furthermore, we find that a proper Brillouin-zone integration of the couplings yields a chemisorption function which is convergent with respect to the finite size of the periodic slab model. The couplings are also found to be reasonably stable with respect to the atomic basis set and with respect to the (non-unique) choice of diabatization scheme. Such convergence aspects are widely known to be nontrivial in the local representation of DFT, with the result that many insightful schemes, such as the projected density of states, are used mainly in a qualitative sense. In contrast, this work presents the chemisorption function and electronic couplings as viable *quantitative* tools with high interpretive power.

Considering the prevalence of electronic couplings in theoretical models, the diabatization methods developed in this work have potential application in a broad array of phenomena. The present schemes are demonstrated in weakly interacting or physisorbed systems. Challenges in the treatment of e.g. fully chemisorped systems are discussed.

Zusammenfassung

Diese Arbeit befasst sich mit der Berechnung der elektronischen Kopplungsparameter H_{ad} aus der Kohn-Sham-Dichtefunktionaltheorie (DFT). Obwohl sie in theoretischen Beschreibungen allgegenwärtig sind, ist die Berechnung elektronischer Kopplungsmatrixelemente in der Praxis aufgrund ihrer nicht beobachtbaren Natur und formal nicht eindeutigen Definition schwierig. Infolgedessen werden H_{ad} oft approximiert und qualitativ verwendet. Die Extraktion elektronischer Kopplungen aus der DFT erfordert eine Projektion der *adiabatischen* elektronischen Struktur auf lokalisierte *diabatische* Fragmente. Im Zusammenhang mit der Ladungsübertragung wird dieses Lokalisierungsverfahren als Diabatisierung bezeichnet. Während zahlreiche Diabatisierungsschemata für die Untersuchung von z.B. Ladungssprüngen zwischen Molekülpaaren entwickelt wurden, ist die elektronische Kopplung auf Oberflächen weniger gut erforscht.

In dieser Arbeit beschäftigen wir uns mit einer Methode namens Projection-Operator Diabatization (POD). Ähnlich wie andere lokale Projektionen der DFT, z. B. die partielle Ladungsanalyse nach Mulliken, leidet die ursprüngliche POD-Methode an Instabilität in Bezug auf den Atomorbital-Basissatz. Indem wir diese Methode zunächst mit einem Gram-Schmidt (GS) Orthogonalisierungsverfahren modifizieren, stellen wir eine verbesserte Methode (POD2GS) bereit, die mit dem Hab11 Benchmark von molekularen Dimeren demonstriert wird. Anschließend entwickeln wir ähnliche Diabatisierungsmethoden für Adsorbate auf Oberflächen. Wir validieren diese Methoden durch die Berechnung ultraschneller Elektronentransfer-Lebensdauern für kernangeregte Argon-Adsorbate auf Übergangsmetalloberflächen. Dazu verwenden wir die Kopplungen, um eine Newns-Anderson Chemisorptionsfunktion aus ersten Prinzipien zu konstruieren, eine kopplungsgewichtete Zustandsdichte (WDOS), die die Linienverbreiterung eines Adsorbat-Grenzorbitals auf einer Oberfläche angibt. Diese Linienverbreiterung wird als ultraschnelle Elektronentransfer-Lebensdauer mit Hilfe der Goldenen Regel von Fermi interpretiert, was zu Ergebnissen führt, die hervorragend mit dem Experiment übereinstimmen.

Die Verwendung ab initio elektronischer Kopplungen im Rahmen einer Newns-Anderson-Chemisorptionsfunktion erweist sich als äußerst vorteilhaft. Die Chemisorptionsfunktion ist in hohem Maße interpretierbar und enthält reichhaltige Informationen über die Phase und Symmetrie der interagierenden Orbitale und ihre Rolle beim Elektronentransfer. Darüber hinaus stellen wir fest, dass eine geeignete Brillouin-Zonen-Integration der Kopplungen eine Chemisorptionsfunktion ergibt, die in Bezug auf die endliche Größe des periodischen Superzellen-Modells konvergent ist. Die Kopplungen erweisen sich auch als einigermaßen stabil in Bezug auf den atomaren Basissatz und in Bezug auf die (nicht eindeutige) Wahl des Diabatisierungsschemas. Es ist allgemein bekannt, dass solche Konvergenzaspekte in der lokalen Darstellung der DFT nicht trivial sind, was dazu führt, dass viele aufschlussreiche Schemata, wie die projizierte Zustandsdichte, hauptsächlich in einem qualitativen Sinne verwendet werden. Im Gegensatz dazu werden in dieser Arbeit die Chemisorptionsfunktion und die elektronischen Kopplungen als brauchbare Textitquantitative Werkzeuge mit hoher Interpretationskraft eingeführt.

In Anbetracht der weiten Verbreitung elektronischer Kopplungen in theoretischen Modellen haben die in dieser Arbeit entwickelten Diabatisierungsmethoden potenzielle Anwendungsmöglichkeiten für eine breite Palette von Phänomenen. Die vorliegenden Schemata werden in schwach wechselwirkenden oder physisorbierten Systemen demonstriert. Die Herausforderungen bei der Behandlung von z.B. vollständig chemisorbierten Systemen werden diskutiert.

Contents

Prologue: Local Representation of the Electronic Structure

The effort to understand physical and chemical systems over recent decades has profited from the rise of sophisticated quantum mechanical models combined with growing capabilities in high-performance computing. Due to an advantageous combination of accuracy and efficiency, Kohn-Sham Density Functional Theory (DFT) has emerged as a staple method for the simulation of condensed matter systems *ab initio* from first-principles [3]. What initially began as an analytical, mathematical *model* of a quantum many-body system – the Schrödinger Equation – has evolved into sophisticated computer *simulations* capable of approximatively describing systems with thousands of atoms and electrons.

The rise of such capabilities has been accompanied necessarily by schemes to extract meaningful chemical information from the often complex solution. Indeed, a simple mathematical or graphical *model* may even be invoked to rationalize the behavior of the *simulated* result, when this alone cannot be clearly understood. This is because, in addition to achieving the *accuracy* of a predicted result, it remains desirable among scientists to *understand* the result [4].

Towards this end, it is commonplace in the interpretation of the electronic structure to employ a *local* representation. That is, to project the electronic structure upon a suitable auxiliary basis of localized states. This is done implicitly when invoking a graphical representations, such as Figure 1, or can be computational, as in Figure 2. Local representations allow meaningful information on e.g. the bonding between fragments to be extracted. In first-principles plane-wave calculations, for example, a projection upon atomic orbitals [5–7] is a prerequisite to gain access to local parameters such as atomic partial charges or bond order analyses. Within methods which already use a local (atomic) basis set, further projection upon a specifically designed auxiliary basis can also be desirable. In the study of charge transfer on surfaces, a projection upon local charge transfer states (called *diabats*) – for example, the molecular orbitals of the adsorbate and the bands of the surface – may be performed, and the coupling between them calculated (Figure 2). Further local schemes include the partial charge analysis of e.g. Robert Mulliken (Nobel prize in Chemistry, 1966) [8], the atomic projected density of states [3], the Crystal Orbital Overlap Population (COOP) [4, 9–11] bond analysis (Roald Hoffmann, Nobel Prize in Chemistry 1981) and Crystal Orbital

Hamilton Population (COHP) bond analysis schemes [7, 12–14]. The COHP is of particular interest in this work, as it employs a weighting of the density of states, where weights are the signed Hamiltonian (coupling) matrix elements between atomic orbitals. Localization of the DFT electronic structure is also necessary in the study of specific properties such as core-hole excitations [15], polarons [16], and in the preparation of states such as localized molecular orbitals [17], or maximally-localized Wannier functions [18, 19] for the purpose of studying highly-correlated physics in specific regions of the system.

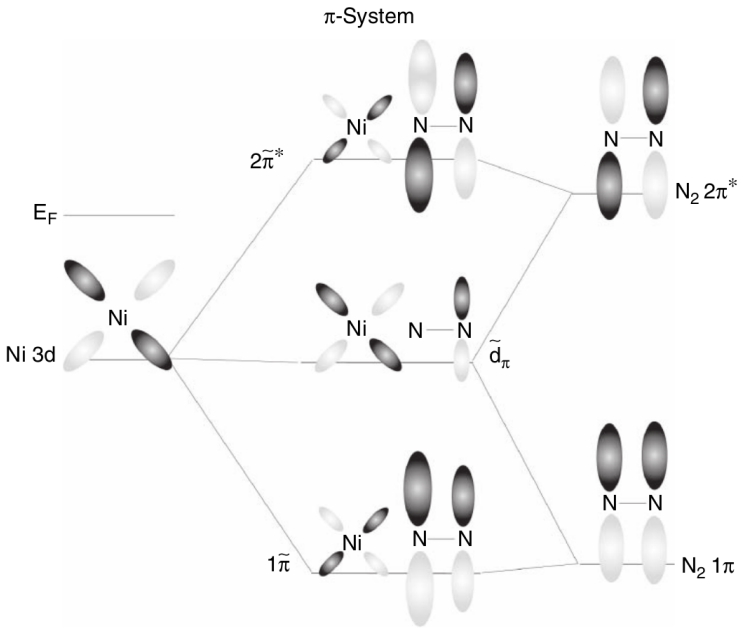

Figure 1: A qualitative frontier orbital interaction diagram describing the chemisorption of a Nitrogen molecule onto a Nickel substrate. π-interactions from N 2*p* and Ni 3*d* orbitals are shown. Figure reused with permission from Reference [20]. Copyright 2008 Elsevier. Original image from Reference [21]. Copyright 2004 Elsevier. Reused with permission.

The local representation of the electronic structure is clearly highly advantageous, as was perhaps first recognized by the ancient Greeks with their *atomos*. Diagrams of local orbital interactions, such as those of Figure 1, indeed constitute the very language of chemistry and have been championed for their instructive value – in an era dominated by complex calculations – by pedagogues such as Roald Hoffmann [10, 11]. The electronic structure provided by DFT, however, is generally delocalized: the single-particle orbitals are often distributed over the whole system under consideration, complicating their interpretation (Figure 2). Localization schemes, which define the states for the local descriptions above, have historically served as a bridge between the chemical (atomic) and physical (Bloch) viewpoints, and have followed the growth of DFT in their sophistication [3, 7–9, 12].

A common challenge among localization schemes, however, is the non-unique choice of the localized states, and the resulting dependence of any calculated quantities (e.g. atomic

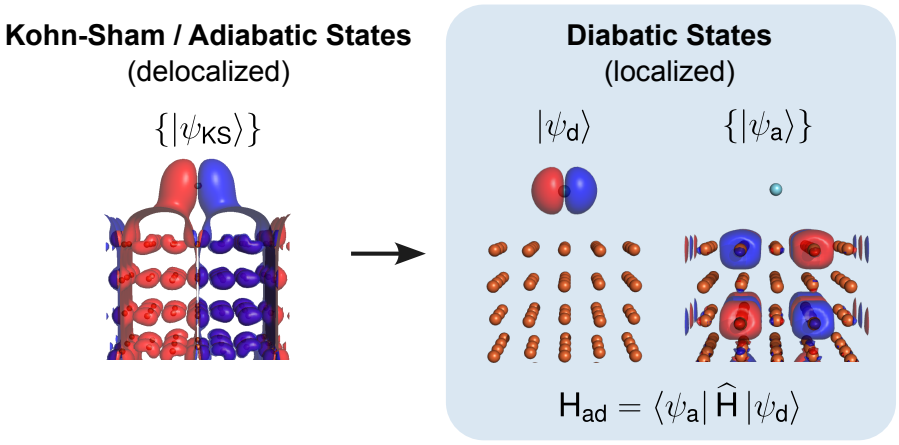

Figure 2: A scheme for *quantitative* computation of frontier orbital interactions. Left: an example Kohn-Sham eigenstate (**k**=Γ) from the Ar/Fe(110) system, with significant presence on one of the Ar 3p HOMO orbitals. Right: states which have been localized on either adsorbate or surface in a *diabatic* or local representation.

partial charge, bond orders, or electronic coupling) on the localization scheme employed [3, 12, 13]. The principal dilemma is that the separation of the *adiabatic* electronic structure into fragments, such as individual atoms, is ambiguous. This is particularly challenging when the fragments are bonded and share electron density. Unlike Kohn-Sham states, which are calculated through a variational minimization of the total energy, local states for projection schemes may be defined (indeed, designed) at will for the property of interest, with the result that numerous schemes are available for each application. The diverse array of partial charge analysis schemes is one example of this dilemma, with Mulliken [8], Hirshfeld [22] and Bader [23] methods all commonly used and compared. Numerous methods for the calculation of diabatic charge transfer states (known as *diabatization* methods) also exist: the diabats can in the simplest case be the orbitals of isolated fragments, or alternatively calculated as the orbitals of interacting fragments within a partitioned Hamiltonian [24].

A separate but related problem is the dependence of localization schemes on the choice of underlying (atomic) basis set. Mulliken partial charge analysis, as well as the atomic projected density of states (PDOS), are for example well known to be sensitive to (even *divergent*) with respect to respect to the choice of atomic orbital basis set, due to superposition effects [3, 12]. The bond order analysis schemes COOP [9–12] and COHP [7, 12, 13], as well as plane-wave projection schemes [5–7] and diabatization schemes for the electronic coupling [1, 24, 25], all report similar challenges with respect to atomic basis sets.

It is the fundamental ambiguity in local representations, originating from their non-uniqueness as well as basis set sensitivity, which commonly limits their use to the qualitative, or at most semi-quantitative sense. Nevertheless, these computational schemes, as well as simple diagrams like Figure 1, form today's staple methods for interpreting complex electronic structure calculations and are the source of valuable insights.

The interpretive advantages of local representations raises the question of whether such

schemes – even the graphical schemes of Figure 1 – could be applied in a *quantitative* sense, e.g. to generate useful descriptors for computational screening studies. Recent works have indeed explored such quantitative applications. In the study of electron transfer, the coupling between diabatic states localized on donor and acceptor fragments (Figure 2) serves as a key parameter in quantitative hopping models of charge mobility [24, 26–28]. First-principles electronic couplings have been used e.g. in the study and design of dye candidates for sensitized solar cells or photocatalysis [24, 25, 29]. The Hamiltonian (coupling) matrix elements between atomic orbitals within COHP analysis have recently been demonstrated as a quantitative chemical bonding descriptor for adsorbates on surfaces, suggesting suitability for this representation in the machine-guided search for new catalysts [14]. Electronic couplings are also used semi-quantitatively to study the chemical modulation of Kondo physics [30, 31] in highly-correlated molecular adsorbates, for quantum information applications.

The desire for quantitative applications, however, quickly confronts the limitations posed by the nontrivial (and at times even divergent) convergence behaviors which are conveniently dismissed in qualitative applications. In the calculation of electronic coupling matrix elements, the need for careful consideration of different localization [6, 7, 13, 30] (diabatization [1, 32]) schemes, basis set dependencies [1, 12, 30], finite size effects [30, 33] and the differences between periodic and cluster approaches [30] has been recognized. Careful consideration of such aspects is a prerequisite for the quantitative use of these parameters.

The challenge faced by quantitative approaches is further exemplified by the fact that local projection schemes rarely yield observable quantities which can be compared to experiment. Even when experimental data is available, for example in the form of measured electron transfer lifetimes, which can be related to electronic coupling matrix elements, there is still the chance of a fortituous agreement if convergence is not first properly demonstrated.

In summary, local representations are essential and wide-spread in the qualitative interpretation of the electronic structure. However, nontrivial convergence aspects may limit the quantitative application of these useful schemes, particularly when predicting sensitive properties such as electron transfer lifetimes. A comparison of the many local representations of DFT – and how respective schemes manage inherent ambiguities – would be worth its own seperate study. In this work, we shall focus on the development of quantitative diabatization schemes for the calculation of electronic couplings and charge transfer. The insights reported here however carry possible implications for other local schemes.

1 Introduction

1.1 The Electronic Coupling

The electronic coupling

$$H_{ad} = \langle \psi_a | \hat{H} | \psi_d \rangle \tag{1.1}$$

is a central quantity in the physical and chemical theory [10] which forms our understanding of the world at the quantum scale. This includes materials and phenomena of high technological importance, such as photochemistry and photovoltaics [34–36], as well as heterogeneous catalysis [37–40]. Coupling is central in the theory of the chemical bond and is routinely invoked *qualitatively* in the frontier orbital interaction diagrams championed by e.g. Roald Hoffmann. [10, 11] Furthermore, electronic coupling is central in the interpretation of fundamental physical experiments, including those related to charge transfer, where it is used to understand e.g. non-adiabatic excited-state dynamics [41–43], desorption induced by (multiple) electronic transitions (DIET/DIMET) [44, 45], scanning-tunneling microscopy (STM) [46–51], and pump-probe and core-hole clock spectroscopies [52].

The Newns-Anderson model [53], for example, uses the electronic couplings to describe the chemisorption of adsorbates on surfaces, and has been widely used to explain e.g. the catalytic activity of transition metals [20, 37–40, 54–59]. The importance of such processes cannot be understated: The Haber-Bosch catalytic process alone consumes between 1-2% of world's energy production and is approximately 60% energy efficient [60, 61]. This produces fertilizer which feeds 70% of the world's population. An improvement in the energy efficiency of such processes would therefore have great ecological benefits. In the ongoing search for more efficient catalysts, Newns-Anderson-based models remain relevant to understanding the role of the electronic structure in catalysis [37, 40, 56, 59, 62–67]. This is true despite relying on an approximative treatment of the electronic coupling, as described below.

The calculation of electronic couplings from first principles requires a representation of the electronic structure in terms of localized donor and acceptor states. This is illustrated in Figure 2. The process of identifying and projecting upon these states, diabatization, is similar to localization schemes employed elsewhere in the interpretation of the electronic strucure. The non-unique definition of the diabatic states (diabats) however leaves the door open for

many possible strategies for the calculation of electronic couplings. Diabatization schemes within DFT include constrained DFT (CDFT) [32, 68], fragment-orbital DFT (FODFT) [69, 70] and Projection-Operator Diabatization (POD) [24, 71]. The POD method can be advantageous, as it extracts diabatic states from the Kohn-Sham Hamiltonian of the combined system and thus includes interactions which are missing from schemes based on isolated fragments.

A large number of works have sought to calculate the electronic coupling quantitatively for surface systems using the POD method. For example, POD has been used to calculate coupling and ultrafast electron transfer (ET) rates between photo-excited adsorbates and semiconducting substrates in dye-sensitized solar cell and photocatalytic systems [24, 25, 29, 71–73]. These works have demonstrated the utility of first-principles electronic couplings – and diabatization generally – in models of ET. However, they openly acknowledge a significant sensitivity of the POD method to the underlying atomic basis set (indeed, it is found to diverge rather than converge with increasingly diffuse basis sets [1]). Furthermore, they use non-periodic cluster models which exclude the possible role of band structure in the ET process. Hence, questions remain about the suitability of POD for the quantitative prediction of electronic couplings. Due to a lack of experimental ET data for many systems, it is often difficult to assess the integrity of diabatization schemes and couplings beyond the qualitative sense. The Hab11 [74] and Hab7 [75] benchmarks offer a welcome proving ground to test diabatization schemes, although only for molecular dimers.

In the context of surface chemistry, recent applications of the Newns-Anderson model have settled for approximations to the electronic coupling, targeting qualitative rather than quantitative descriptions [63, 65, 66, 76]. This has still sufficed to provide a phenomenological explanation of catalytic reactivity trends, explaining for example why Gold is the "most noble of metals"[38]. The use of approximate electronic couplings (derived e.g. from effective medium theory [37]) comes with limitations, however, and understanding outliers to Newns-Anderson models, such as adsorbates and surfaces which break anticipated scaling behaviors of the "*d*-band model" [39, 54, 63], has become its own undertaking [59, 64, 65]. Here, the explicit and first-principles calculation of H_{ad} may prove useful but has not, to our knowledge, been attempted.

It is also possible to study the quantitative *effect* of electronic couplings indirectly: lineshapes of core-excited adsorbates have been successfully predicted with surface Green's function methods [27, 28, 33, 77, 78]. While the couplings themselves are not calculated here explicitly, they are related to the energy broadening (hybridization) of the adsorbate frontier state by Newns [53]. This line broadening is in turn related to the lifetime of an electron promoted to the state, which can be determined experimentally in ultrafast charge transfer measurements. Core-hole clock spectroscopy is one such method which can measure electron transfer lifetimes at the sub-femtosecond time scale. For example the ET lifetime for core-excited Sulfur atoms S[$2s^{-1}3p_z^1$] on Ru(0001) was measured at 320$\pm$90 attoseconds. The method combining DFT and Green's function methods yielded a prediction of 630$\pm$150 attoseconds, which is considered highly accurate [78]. However, the interpretation of the accurate *predictions* of this method is not trivial, relying on a simplified *model* based on

the free-electron-like *s* and *p*-bands of the transition metal surface. Thus, the otherwise accurate prediction leaves many questions open as to the mechanism of electron transfer, such as the role of the transition metal *d*-band. Interpretable *ab initio* models - capable of handling the complexity of such systems, which contain many atoms, have been called for for decades by both the experimental [79, 80] and theoretical [27, 28, 81–83] communities.

The motivation to attempt a fully first-principles – and quantitatively robust – description of electronic coupling on surfaces thus emerges both from the heterogeneous catalysis community, as well as from the ultrafast ET community. The situation is further complicated by the extended nature of surface systems. It has been argued [24, 28, 33] that the finite slab models used in periodic DFT simulations –which contain a discrete quasi-continuum of states rather than a proper continuum – would be prone to finite size effects prohibiting the prediction of fine properties such as lineshapes. In contrast, other properties such as the variational total energy or e.g. adsorbtion energies are routinely calculated with high accuracy in finite, periodic slab models [3]. Such concerns have indeed been the motivation for development of methods with include the effect of the infinite surface with Green's function techniques [24, 28, 33, 77].

These finite size effects, combined with the ambiguities related to the choice of diabats and the atomic basis set outlined above, will constitute the principal challenges for the quantitative, first-principles calculation of electronic coupling on surfaces.

1.2 This Work

This work summarizes efforts to develop numerically stable and quantitatively robust Projection-Operator Diabatization schemes for the calculation of electronic couplings. These schemes are demonstrated for molecular dimers in the Hab11 benchmark [1, 74], and on surfaces, validated against electron transfer measurements of core-excited Argon on transition metals [2].

In this work we shall directly confront aspects which are known to limit the quantitative application of electronic couplings (and which are common to many local representations of DFT, as described above):

1. We address the non-unique choice of a diabatic basis, identifying and comparing multiple diabatization schemes and their effect on couplings and electron transfer predictions.

2. We study the inherent sensitivity of the diabatization schemes with respect to the underlying atomic orbital basis set. Crucially, by virtue of an orthogonalization strategy, we correct the divergent behavior of POD and offer POD2GS (Gram-Schmidt) and POD2L (Löwdin) methods which are stable across a range of basis sets [1], demonstrated in molecular dimers.

3. We demonstrate, within a periodic model of Argon physisorbed on transition metals, the calculation of electronic couplings between adsorbate and surface throughout the

Brillouin Zone. The proposed diabatization schemes are termed ($frag_d$,$frag_a$)GS and ($POD2_d$,$frag_a$)GS and combine both fragment and POD2 approaches developed for molecules.

4. We demonstrate the construction of a first-principles Newns-Anderson Chemisorption function from the (**k**-dependent) couplings. A suitable integration of couplings over the Brillouin Zone is shown to be necessary to achieve a chemisorption function which is robust against finite slab size effects [2], in contrast with earlier works employing a Γ-point approximation [71]. This resolves previous concerns about the inadequacy of finite slab models [28, 33].

Beyond the demonstration of convergence properties, we demonstrate the utility of the resulting quantitative scheme in elucidating the electron transfer process on surfaces. While the present method benefits from the weakly physisorped nature of Argon, the outcome overall demonstrates strong potential for diabatic representations in the first-principles study of adsorbed systems, and provides a foundation for further developments in chemisorped systems.

In the following, we first summarize the necessary equations of Density Functional Theory and the Newns-Anderson model. We then describe the Projection-Operator Diabatization methods and the implementation of the Newns-Anderson Chemisorption Function within periodic boundary conditions. Results for both molecular and surface systems are then presented and finally discussed.

2 Theory

2.1 The Adiabatic Picture: Kohn-Sham Density Functional Theory

A mean-field, single-particle solution to the many-body Schrödinger Equation is given by Kohn-Sham Density Functional Theory (DFT) [84]. This treats the electronic problem, with nuclei treated classically under the Born-Oppenheimer approximation. This is an *adiabatic* description as it provides a single ground-state potential energy surface upon which the nuclei may evolve. Kohn-Sham DFT builds on the theorems of Hohenberg and Kohn [85], which provide the basis for the treatment of the many-body problem in terms of the electron *density* rather than the many-body wavefunction. The total energy of a system in the ground state can be expressed as a unique functional of the ground state electron density. According to the variational theorem, the ground-state electron density can thus be found by minimizing the total energy. Kohn-Sham Density Functional Theory provides a practical protocol for this, which has achieved wide-spread use due to its advantageous combination of accuracy and numerical tractability. We here summarize the key equations and refer the reader to standard references for further detail [3, 86].

We first review the Kohn-Sham equations as summarized by Perdew [87] for a non-periodic, molecular system in vacuum. The many-body electronic problem is reformulated as an auxiliary one-electron Schrödinger equation,

$$\left(-\frac{\nabla^2}{2} + v(\mathbf{r}) + u([n];\mathbf{r}) + v_{\mathrm{xc}}^{\sigma}([n_{\uparrow}, n_{\downarrow}];\mathbf{r})\right)\psi_{\sigma \mathrm{i}}(\mathbf{r}) = \epsilon_{\sigma \mathrm{i}}\psi_{\sigma \mathrm{i}}(\mathbf{r}) \tag{2.1}$$

with the electron density for each spin direction σ defined as

$$n_{\sigma}(\mathbf{r}) = \sum_{\mathrm{i}} \theta(\mu - \epsilon_{\sigma \mathrm{i}})|\psi_{\sigma \mathrm{i}}(\mathbf{r})|^2. \tag{2.2}$$

The single-particle Hamiltonian operator in Equation (2.1) includes a classical Hartree potential, which captures the Coulomb interaction of an electron with the mean field given by

the density of *all* electrons:

$$u([n];\mathbf{r}) = \int d^3r' \frac{n(\mathbf{r}')}{|\mathbf{r}-\mathbf{r}'|}. \tag{2.3}$$

Here, the total electron density consists of a sum of spin components:

$$n(\mathbf{r}) = n_\uparrow(\mathbf{r}) + n_\downarrow(\mathbf{r}). \tag{2.4}$$

The term $v^\sigma_{\mathrm{xc}}([n_\uparrow, n_\downarrow];\mathbf{r})$ in Equation (2.1) is the spin-dependent exchange-correlation potential which includes the many-body effects not present in a mean field model. The term $v(\mathbf{r})$ is the electron-nuclear interaction (an external potential). The total energy is written as a functional of the density:

$$E[n_\uparrow, n_\downarrow] = T_s[n_\uparrow, n_\downarrow] + \int d^3r n(\mathbf{r}) v(\mathbf{r}) + U[n] + E_{\mathrm{xc}}[n_\uparrow, n_\downarrow]. \tag{2.5}$$

Here, the nuclear-nuclear Coulomb repulsion is omitted and is implicit. The first term is the kinetic energy, defined as

$$T_s[n_\uparrow, n_\downarrow] = \sum_\sigma \sum_{\mathrm{i}} \theta(\mu - \epsilon_{\sigma\mathrm{i}}) \left\langle \psi_{\sigma\mathrm{i}} \right| -\frac{\nabla^2}{2} \left| \psi_{\sigma,\mathrm{i}} \right\rangle . \tag{2.6}$$

The kinetic energy term is indeed one of the main innovations of the Kohn-Sham framework, as it is formulated in terms of single-particle orbitals, whereas deriving kinetic energy from density alone would be much less straight-forward. Only occupied states contribute to the kinetic energy, as determined by the step function θ and the chemical potential μ.

The next term is the Hartree electrostatic self-repulsion, defined as

$$U[n] = \frac{1}{2} \int d^3r' \int d^3r \frac{n(\mathbf{r})n(\mathbf{r}')}{|\,\mathbf{r}-\mathbf{r}'|} \tag{2.7}$$

The final term of Equation (2.5) is the exchange-correlation functional, which must be approximated, for example with the the generalized-gradient approximation (GGA) [88]:

$$E^{\mathrm{GGA}}_{\mathrm{xc}}[n_\uparrow, n_\downarrow] = \int d^3r f(n_\uparrow, n_\downarrow, \nabla n_\uparrow, \nabla n_\downarrow). \tag{2.8}$$

In the Hamiltonian operator of Equation (2.1), the exchange-correlation potential is defined as the functional derivative of the exchange-correlation energy functional:

$$v^\sigma_{\mathrm{xc}}([n_\uparrow, n_\downarrow];\mathbf{r}) = \frac{\delta E_{\mathrm{xc}}}{\delta n_\sigma(\mathbf{r})}. \tag{2.9}$$

The total energy of Equation (2.5) can also be expressed in terms of the sum of single-particle energies from the eigenproblem of Equation (2.1) :

$$E = \sum_{\sigma\mathrm{i}} \theta(\mu - \epsilon_{\sigma\mathrm{i}})\epsilon_{\sigma\mathrm{i}} - U[n] - \int d^3r n(\mathbf{r}) v^\sigma_{\mathrm{xc}}([n_\uparrow, n_\downarrow];\mathbf{r}) + E_{\mathrm{xc}}[n]. \tag{2.10}$$

The total energy is not equal to the sum of single-particle energies, but must be corrected to account for double counting in the electrostatic term, and the exchange-correlation potential energy (which is already included in the eigenvalues) is replaced by the exchange-correlation density functional which is correct for the total energy.

Equations (2.1)-(2.10) form the self-consistent Kohn-Sham method. In practice, an initial guess for the density of a system, Equation (2.2), is made. A reasonable guess is often simply the superposition of atomic densities. The Kohn-Sham Hamiltonian is then constructed for the system, and the Kohn-Sham eigenproblem of (2.1) is solved. A new density is calculated from the resulting Kohn-Sham states $\psi_{\sigma i}$, and the self-consistent field (SCF) cycle iterates until convergence. Finally, the total energy of the system is calculated from Equation (2.5), and can be used e.g. to explore the ground-state potential energy surface of the system.

Basis Set

In practice, the scheme above is implemented in a basis set of either plane-waves or atomic orbitals. In the FHI-aims electronic structure package [89, 90], numeric, atom-centered (NAO) basis functions are used. We describe this package in the following.

Defining the single-particle Hamiltonian operator as above as

$$\hat{h}_{KS} = \hat{t}_s + \hat{v}_{ext} + \hat{v}_{xc}, \tag{2.11}$$

the single-particle Kohn-Sham eigenproblem is written as

$$\hat{h}_{KS} |\psi_l\rangle = \epsilon_l |\psi_l\rangle . \tag{2.12}$$

In the basis of atom-centered basis functions $\varphi_i(\mathbf{r})$, the Kohn-Sham eigenstates $\psi_l(\mathbf{r})$ are written as

$$\psi_l(\mathbf{r}) = \sum_i^{N_b} c_{il} \varphi_i(\mathbf{r}) \tag{2.13}$$

and the eigenproblem takes the form

$$\sum_j h_{ij} c_{jl} = \epsilon_l \sum_j s_{ij} c_{jl}. \tag{2.14}$$

The matrix elements are constructed by numerical integration in real space, with the Hamiltonian elements taking the form

$$h_{ij} = \int d^3r [\varphi_i^*(\mathbf{r}) \hat{h}_{KS} \varphi_j(\mathbf{r})] \tag{2.15}$$

and the basis set overlap matrix taking the form

$$s_{ij} = \int d^3r [\varphi_i^*(\mathbf{r}) \varphi_j(\mathbf{r})] \tag{2.16}$$

In general, matrix elements may be complex.

Periodic Boundary Conditions

For a system with periodic boundary conditions, such as an adsorbate on an extended metal surface, the above equations become dependent on the quasi-momentum **k** and are evaluated at desired **k**–points in the Brillouin zone. Properties such as the total energy and density are now acquired by averaging over the Brillouin zone [3]. In FHI-aims [89, 90], Bloch-like generalized basis functions $\chi_{i,\mathbf{k}}(\mathbf{r})$ are defined from the real-space, atom-centered basis functions $\varphi_i(\mathbf{r})$, which are centered in unit cells shifted by translation vectors **T**(**N**), [**N**=(N_1, N_2,N_3)]:

$$\chi_{i,\mathbf{k}}(\mathbf{r}) = \sum_{\mathbf{N}} \exp[i\mathbf{k}\cdot\mathbf{T}(\mathbf{N})]\cdot\varphi_i[\mathbf{r}-\mathbf{R}_{at}+\mathbf{T}(\mathbf{N})] \tag{2.17}$$

The Kohn-Sham Hamiltonian matrix is then defined at each **k**–point:

$$\begin{aligned} h_{ij}(\mathbf{k}) &= \left\langle \chi_{i,\mathbf{k}} \middle| \hat{h}_{KS} \middle| \chi_{j,\mathbf{k}} \right\rangle \\ &= \sum_{\mathbf{M},\mathbf{N}} \exp\{i\mathbf{k}\cdot[\mathbf{T}(\mathbf{N})-\mathbf{T}(\mathbf{M})]\} \left\langle \varphi_{i,\mathbf{M}} \middle| \hat{h}_{KS} \middle| \varphi_{j,\mathbf{N}} \right\rangle, \end{aligned} \tag{2.18}$$

$$\tag{2.19}$$

with an equivalent (complex) matrix $s_{ij}(\mathbf{k})$ generated for the overlap. In practice, due to the cutoff radius of the atom-centered basis functions (typically 6 Å), terms in the sum of Equation (2.19) become zero for unit cells which are far apart, and only a small number of translation vectors **M**,**N** need to be considered.

Kohn-Sham eigenstates $\psi_{l,\mathbf{k}}(\mathbf{r})$ (now Bloch states) are solved at desired **k**-points by diagonalizing the Hamiltonian matrix of Equation (2.19), and e.g. the band structure can thus be determined.

In periodic calculations, system properties such as the electron density or the total energy are calculated by averaging over the Brillouin zone. In practice, this is approximated by using e.g. a Monkhorst-Pack [3, 91, 92] mesh of discrete **k**-points. By considering symmetry, it is possible to identify irreducible **k**-points in the Brillouin zone (IBZ) and thus save computational expense. The Brillouin-zone integral (average) of some quantity F is thus approximated by a weighted sum over the irreducible k-points [3]:

$$F_0 \approx \sum_{\mathbf{k}}^{IBZ} w_{\mathbf{k}} F_{\mathbf{k}} \tag{2.20}$$

where the weights $w_{\mathbf{k}}$ sum up to 1. For example, the electron density becomes an average over occupied states over the Brillouin zone:

$$n(\mathbf{r}) = \sum_{\mathbf{k}}^{IBZ} w_{\mathbf{k}} \sum_{l}^{N_{occ}} \theta(\epsilon_{Fermi}-\epsilon_{l,\mathbf{k}})|\psi_{l,\mathbf{k}}(\mathbf{r})|^2. \tag{2.21}$$

The Fermi level ϵ_{Fermi} is determined by charge neutrality. The density of states is likewise an average over the Brillouin zone:

$$\text{DOS}(\epsilon) = \sum_{\mathbf{k}}^{\text{IBZ}} w_{\mathbf{k}} \sum_{\text{I}}^{\text{N}_{\text{acc.}}} \delta_\sigma(\epsilon - \epsilon_{\text{I},\mathbf{k}}). \tag{2.22}$$

For practical reasons, i.e. to yield a smoothe DOS curve, the δ function is often replaced by a Gaussian or Lorentzian distribution with an energetic broadening parameter σ.

Upon solution of the **k**-integrated electron density, the total energy (from a similar **k**-integration of Equation (2.10)) can be evaluated, and if not converged, a new Hamiltonian operator (Equation (2.11)) and from it new **k**-dependent Hamiltonian matrices (Equation (2.19) are constructed and diagonalized. The scheme iterates to self-consistency as in the non-periodic case. A more detailed description is available in standard works [3, 89].

The protocol, upon reaching convergence, gives the single-particle ground-state electronic structure of the system. In addition to providing the total energy and density of the system, the Kohn-Sham eigenstates can be interpreted meaningfully despite their auxiliary role in the framework. These orbitals are formally only mathematical constructs, with sound physical meaning only ascribed to the most diffuse occupied orbital (the HOMO for molecules) [86]. Important properties such as the density of states of a system, its band structure and measures of bonding and hybridization [7, 13] are routinely extracted from an analysis of the adiabatic Kohn-Sham spectrum [3]. Below, we will even interpret the geometric (phase and symmetry) properties of the Kohn-Sham orbitals to yield the electronic coupling between subsystems.

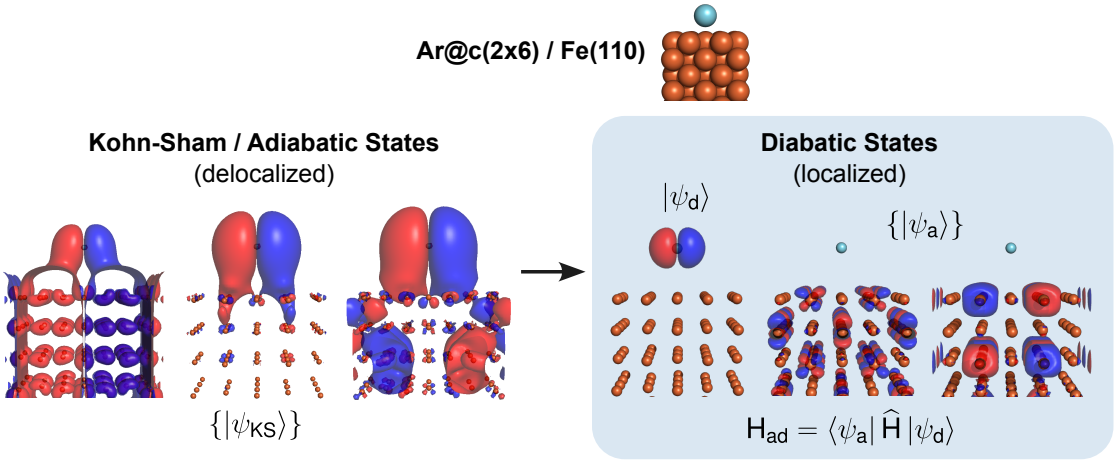

Figure 2.1: Illustration of the adiabatic versus diabatic descriptions of the adsorbed Ar/Fe(110) surface system. Left: example Kohn-Sham states (**k**=Γ) with significant presence on the Argon 3p HOMO are shown. Right: localized Argon and slab states, and their coupling, may be achieved with diabatization schemes.

2.2 The Newns-Anderson Model

The adiabatic Kohn-Sham picture above provides the single-particle eigenstates, energy and density of the full system under consideration. Kohn-Sham states are typically delocalized over the full system, as shown in Figure (2.1). It can be advantageous, however, to consider subsystems and their interactions, such as the electronic coupling. Such a picture is necessary for e.g. the description of open quantum systems interacting with an environment [93, 94]. The problem of a discrete state interacting with a continuum of bath states is indeed classic in physics, and was addressed by e.g. Anderson in his theory of magnetic impurities in alloys [95]. Newns [53] applied the Anderson impurity model to the study of isolated adsorbates on surfaces in his model of chemisorption.

We summarize here the highly successful Newns-Anderson model. A more complete description is available in the literature [53, 58]. Afterwards, we will show how this useful qualitative *model* can be implemented as a *method* within a modern first-principles DFT framework.

Consider a system consisting of a surface and an adsorbate. The Hamiltonian can be written in second-quantized form,

$$H = \epsilon_d \hat{n}_d + \sum_a \epsilon_a \hat{n}_a + \sum_a (H_{da} \hat{b}_d^\dagger \hat{b}_a + H_{ad} \hat{b}_a^\dagger \hat{b}_d),$$

where ϵ_d is the energy of the adsorbate frontier state (e.g. the HOMO or LUMO), which we refer to as the donor and label d, and ϵ_a are the unperturbed Bloch states of the surface, which we refer to as acceptors and label with a. The states interact via the electronic coupling H_{ad}. $\hat{n}_i = \hat{b}_i^\dagger \hat{b}_i$ is a number operator and $\hat{b}_i^\dagger$, $\hat{b}_i$ are creation and annihilation operators.

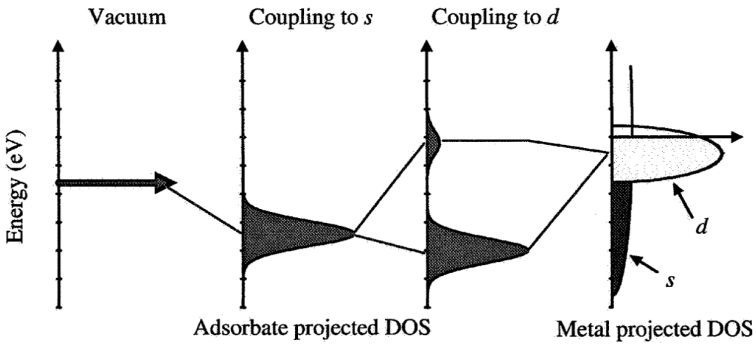

Figure 2.2: A schematic of the electronic structure of adsorption, showing broadening and subsequent hybridization of the adsorbate frontier orbital. Reused by permission from Reference [96]. Copyright 2005 Springer Nature.

Upon interaction with the surface states ϕ_a, the adsorbate frontier orbital ϕ_d is energetically broadened and is no longer discrete. This is illustrated in Figures 2.2 and 2.3. The energetic line shape of ϕ_d is given by the projected density of states:

$$n_d(\epsilon) = \sum_a |\langle\phi_a|\phi_d\rangle|^2 \delta(\epsilon - \epsilon_a). \tag{2.23}$$

This can be rewritten in the Green function formalism as:

$$\begin{aligned} n_d(\epsilon) &= -\frac{1}{\pi} \mathrm{Im} \sum_a \frac{\langle\phi_d|\phi_a\rangle \langle\phi_a|\phi_d\rangle}{\epsilon - \epsilon_a + i\delta} \\ &= -\frac{1}{\pi} \mathrm{Im} G_{dd}(\epsilon), \end{aligned} \tag{2.24}$$

where δ is a small positive number, and the single-particle Green function is

$$G_{dd}(\epsilon) = \frac{1}{\epsilon - \epsilon_d - \Sigma(\epsilon)}. \tag{2.25}$$

This contains the self-energy $\Sigma(\epsilon) = \Lambda(\epsilon) + i\Delta(\epsilon)$ which consists of the *chemisorption functions*

$$\begin{aligned} \Delta(\epsilon) &= -\mathrm{Im} \sum_a \left[\frac{|H_{da}|^2}{\epsilon - \epsilon_a + i\delta} \right] \\ &= \pi \sum_a |H_{da}|^2 \delta(\epsilon - \epsilon_a) \end{aligned} \tag{2.26}$$

and

$$\Lambda(\epsilon) = \frac{P}{\pi} \int_{-\infty}^{\infty} \frac{\Delta(\epsilon')d\epsilon'}{\epsilon - \epsilon'}. \tag{2.27}$$

P denotes the Cauchy principle value.

Combining the above, the projected density of states for the adsorbate frontier orbital can now be written in the form

$$n_d(\epsilon) = \frac{1}{\pi} \frac{\Delta(\epsilon)}{[\epsilon - \epsilon_d - \Lambda(\epsilon)]^2 + \Delta^2(\epsilon)}. \tag{2.28}$$

We see that the chemisorption function $\Delta(\epsilon)$ emerges as a crucial component of the Newns-Anderson model, and serves both as an important quantitative and qualitative tool. The chemisorption function is a coupling-weighted density of states, also called the WDOS in the literature [97] or the (imaginary component of the) hybridization function [30]. While the function $\Lambda(\epsilon)$ describes the shift in energy of the adsorbate state, the chemisorption function $\Delta(\epsilon)$ gives the line shape of the adsorbate state – a crucial indicator of e.g. bonding behavior – expressed in terms of the electronic couplings H_{ad}. Formally, the chemisorption function –also knows as the linewidth function– yields the half-width at half-maximum (HWHM) of a Lorentzian distribution. For a weakly interacting system, with weak couplings H_{ad}, the adsorbate frontier state is thus broadened into a (narrow) Lorentzian line shape (Figure 2.2). For stronger couplings, however, the lineshape predicted by Equation (2.28) may be more complex, and hybridization may lead to the formation of bonding and anti-bonding peaks (Figure 2.3). The width of the interacting bands plays a role in this effect, with *s* and *p* bands typically treated in a wide-band and the *d*-band in so-called narrow band approximations [63]. A narrow band may be approximated by an effective two-level model [55, 57].

The chemisorption function (onwards, we mean by this the function $\Delta(\epsilon)$) can also be understood from the perspective of resonant electron transfer. In the weak coupling regime, such as a physisorped adsorbate which couples primarily to the *s* and *p* states of the surface (commonly termed the wide-band approximation), the line broadening is weak and closely resembles a single Lorentzian distribution. A promoted electron populating the LUMO donor state can thus be assumed to experience an exponential decay process, with a lifetime determined by the width of the Lorentzian. Importantly, such an interpretation allows for the prediction of ultrafast electron transfer lifetimes which can then be compared to experimental measurements. This provides a crucial route to validate a Newns-Anderson model and the electronic couplings used in its construction, which are not themselves physical observables. Furthermore, the energy-dependence of the equations (2.26) and (2.28) provides also for the treatment of systems in the strong-coupling regime, such as fully chemisorped adsorbates coupled to the *d*-band of transition metals. Here, an electron transfer model assuming a single exponential decay process determined by a single Lorentzian line shape (e.g. the perturbative Golden Rule approach) is likely inappropriate (Figure 2.3).

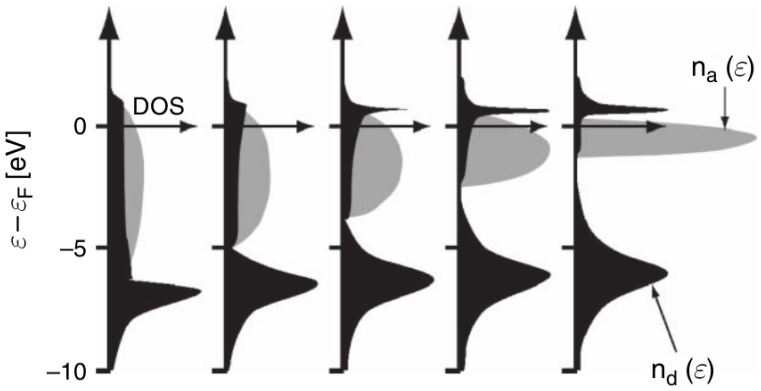

Figure 2.3: A schematic of the projected DOS of the adsorbate frontier state (black) upon interaction with wide or narrow bands of the surface (grey). A wide surface band (left) only broadens the adsorbate level. A narrow band (right) may cause hybridization as in a two-level system. Reused by permission from Reference [57]. Copyright 2008 Elsevier.

3 Methods

Having presented the theory, we now address the question of how the coupling parameters H_{ad} may be calculated from first-principles DFT, and how the chemisorption function may thus be constructed in a practical and quantitative method.

3.1 The Diabatic Picture: Projection-Operator Diabatization

We discuss here a number of approaches to calculate the electronic coupling H_{ad} from density functional theory, first in molecular dimers and then on surfaces. These are referred to as *diabatization* schemes as they seek to identify coupled *diabatic* states within the *adiabatic* electronic structure of DFT. In general, such diabatic states are not uniquely defined, and a number of methods are available to create them and calculate their couplings [26, 32, 36]. The Projection-Operator Diabatization (POD) approach [24, 25, 71–73] is a *deductive* strategy which seeks to extract these couplings from the single Hamiltonian of the combined system. In contrast, a *constructive* strategy will calculate the couplings by considering isolated, non-interacting fragments as the diabats, which then interact via the Hamiltonian of the combined system. An example of such a scheme is fragment-orbital DFT (FODFT) [70].

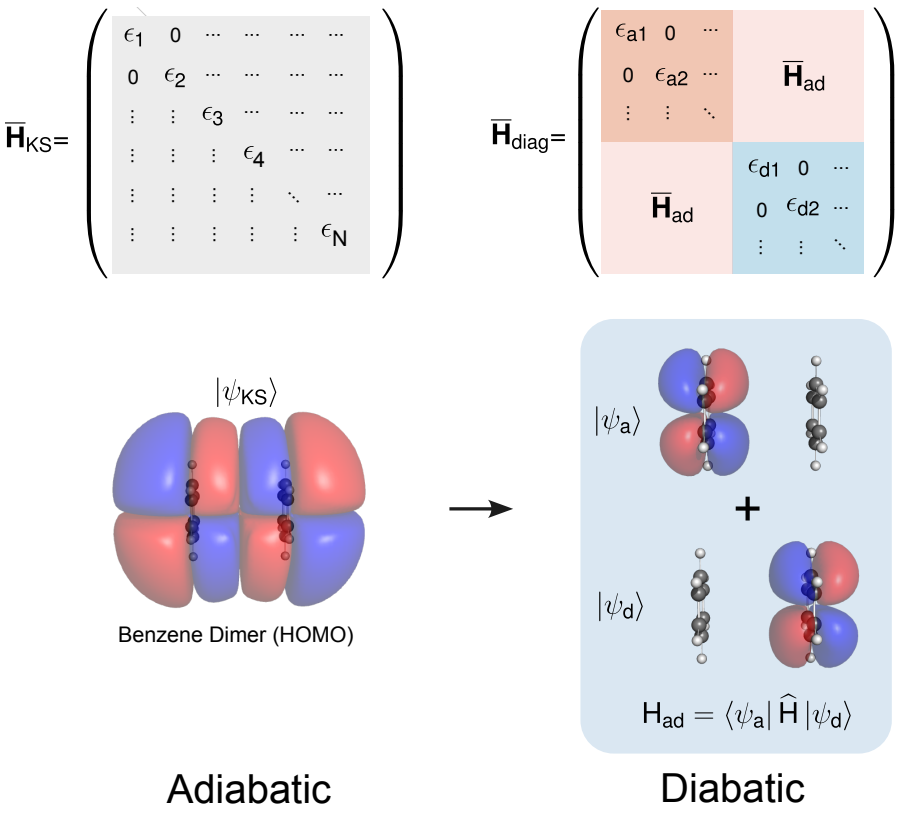

Figure 3.1: Illustration of two descriptions of the Benzene dimer system.

3.1.1 Molecular Systems

Parts of the following section are reproduced with permission from Reference [1]. Copyright 2020 American Chemical Society.

Variations of the POD scheme will first be demonstrated and tested on molecular dimer systems of the Hab11 benchmark set [74]. Here all HOMO-HOMO H_{ad} values have been calculated using the Multi-Reference Configuration Interaction method with Davidson correction (MRCI+Q). The couplings are calculated by applying the energy splitting principle to the adiabatic dimer states:

$$H_{ad} = \frac{\Delta E}{2} \tag{3.1}$$

Here, the coupling of the HOMO orbitals of the fragments is seen to be half of the energy difference ΔE between the bonding and antibonding combinations of these states in the dimer. For example, the adiabatic HOMO of the Benzene dimer is shown in Figure 3.1, and is the anti-bonding combination of the monomer HOMO states. ΔE is thus termed the *adiabatic level splitting*. The energy splitting principle is valid for symmetric dimers.

Qualitatively, the criteria for a successful projection of adiabatic states onto a diabatic basis

include 1) the diabats should be well-localized on donor or acceptor fragments and not change appreciably with the geometry of the system [32] and 2) the diabats of respective fragments should be orthogonal to each other [34, 98, 99]. The argument of well-localized diabats is particularly relevant and natural for the case of weakly bound donor-acceptor systems such as molecular dimers or molecules physisorbed on surfaces. This quality also aids in the interpretability of CT models. The orthogonality requirement, in turn, originates from a tight-binding picture and will be detailed below.

As a common example, FODFT and the closely-related Dimer Projection (DIPRO) method [99] identify diabats as the adiabatic KS states of isolated acceptor (a) and donor (d) fragments which are then combined and orthogonalized via a Löwdin transformation. Respective couplings are finally calculated as the expectation value of the Hamiltonian operator of the combined system: [69, 70]

$$H_{ad} = \langle \psi_a | \hat{H} | \psi_d \rangle \tag{3.2}$$

Constrained DFT (CDFT), on the other hand, relies on self-consistent adiabatic calculations in which the charge carrier is constrained to either fragment within the KS self-consistent cycle [26, 32, 68, 74]. In this work, we pursue a third popular method, the DFT-based Projection-Operator Diabatization (POD) scheme, [24, 25, 71, 72, 100, 101] often also known as block-diagonalization [26, 102, 103]. It relies on a partitioning of the Hilbert space of the adiabatic KS Hamiltonian [24]. Here, the converged Hamiltonian is partitioned (as illustrated in Figure 3.1) based on atom-centered basis functions, and diabatic states emerge as eigenstates of donor and acceptor blocks in the Hamiltonian matrix. This method, unlike FODFT, captures interactions such as polarization between fragments, as the interacting adiabatic Hamiltonian is used to generate diabats.

POD provides formally orthogonal diabats by construction. As already recognized in the original work [24], there is a slight delocalization of diabats over fragments though, as partitioning is carried out only after symmetric orthogonalization of the full Hamiltonian. In the following, we demonstrate that this property of the POD scheme results in non-convergent behavior with respect to the choice of basis set, somewhat arbitrarily limiting its use to small basis sets. On the other hand, the POD method is relatively simple to implement and apply, given that it only requires a post-processing of a converged KS Hamiltonian for the combined system. Indeed, it has seen wide use and fared well in comparisons to FODFT and CDFT in both accuracy and computational efficiency [103]. Yet, as we will show below, POD does indeed fail to produce meaningful results for some cases, especially for DFT codes with naturally quite spatially extended basis sets.

In this work we therefore extend the descriptive power of the method by resolving the basis set convergence issue, allowing for more interpretable and reliable results in different chemical systems and improving the overall accuracy. We address in detail the features of locality and orthogonalization in the POD method through a number of proposed variations to its central equations. These features are thoroughly assessed using the Hab11 benchmark of molecular dimers for hole transport [74], and by examining the benzene dimer as a specific

example. The effect of basis sets and exact exchange is discussed in terms of the accuracy of couplings and their decay behavior over increasing separations. We compare the developed POD flavors to the FODFT and energy-splitting approaches, and conclude with a discussion of some theoretical points and an outlook.

The Projection-Operator Diabatization (POD) Method

The POD approach [104, 105] has been applied to study electronic couplings in the single-particle picture by Thoss *et al.* [24] and has seen frequent application to molecular dimer [71, 101] and surface adsorbate systems [25, 72, 100, 103, 106]. The method is summarized in Figure 3.2 and for completeness we briefly review it here. While we will discuss the case of hole transport, analogue arguments apply for electrons.

Within a single-particle mean-field picture such as DFT, the Hamiltonian of a combined donor-acceptor system is approximated by the Kohn-Sham matrix $\mathbf{H}_{\mathrm{KS}}$. Thereby, we assume the use of an atomic orbital basis set $\{\varphi_\mu\}$ consisting of linearly independent but generally non-orthogonal [107] functions φ_μ with the overlap matrix elements $S_{\mu\upsilon} = \langle\varphi_\mu|\varphi_\upsilon\rangle$.

The KS eigenproblem in this basis is of the generalized form

$$\mathbf{H}_{\mathrm{KS}}\mathbf{C} = \mathbf{SCE} \quad , \tag{3.3}$$

where $\mathbf{C}$ is a matrix containing the KS orbital eigenvectors as columns and $\mathbf{E}$ is a diagonal matrix containing the KS eigenenergies.

The basis set is conveniently orthogonalized with the method of Löwdin [107, 108]:

$$|\widetilde{\varphi}_n\rangle = \sum_j (\mathbf{S}^{-1/2})_{jn}\,|\varphi_j\rangle \quad , \tag{3.4}$$

with the new orthogonal basis functions $\{\widetilde{\varphi}_n\}$ minimally distorted from the original $\{\varphi_j\}$ in a least-squares sense [107]. The KS eigenfunctions can now be projected onto the new orthogonal basis using the transformation matrix $\mathbf{X} = \mathbf{S}^{-1/2}$:

$$\widetilde{\mathbf{C}} = \mathbf{X}^{-1}\mathbf{C} \quad , \tag{3.5}$$

where the notation $\widetilde{\mathbf{C}}$ henceforth generally indicates representations in the orthogonal basis. Inserting Equation (3.5) into (3.3) yields

$$\widetilde{\mathbf{H}}\widetilde{\mathbf{C}} = \widetilde{\mathbf{C}}\mathbf{E} \quad , \tag{3.6}$$

where

$$\begin{aligned}\widetilde{\mathbf{H}} &= \mathbf{X}^{\dagger}\mathbf{H}_{\mathrm{KS}}\mathbf{X} \\ &= \mathbf{S}^{-1/2}\mathbf{H}_{\mathrm{KS}}\mathbf{S}^{-1/2}\end{aligned} \tag{3.7}$$

is the Hamiltonian expressed in the new basis.

To identify diabatic charge-transfer states, the Hilbert space of the system is now partitioned into donor and acceptor regions. This is achieved by identifying blocks in $\widetilde{\mathbf{H}}$ associated with (orthogonalized) basis functions on the donor or acceptor atoms:

$$\widetilde{\mathbf{H}} = \begin{pmatrix} \widetilde{\mathbf{H}}_{\mathrm{aa}} & \widetilde{\mathbf{H}}_{\mathrm{ad}} \\ \widetilde{\mathbf{H}}_{\mathrm{da}} & \widetilde{\mathbf{H}}_{\mathrm{dd}} \end{pmatrix} \quad . \tag{3.8}$$

It is assumed here that the atom centers of the new basis functions $\{\widetilde{\varphi}_j\}$ are unchanged after orthogonalization. The donor and acceptor blocks $\widetilde{\mathbf{H}}_{\mathrm{dd}}$ and $\widetilde{\mathbf{H}}_{\mathrm{aa}}$ can be treated separately, forming their own eigenproblems:

$$\begin{aligned} \widetilde{\mathbf{H}}_{\mathrm{aa}}\widetilde{\mathbf{C}}_{\mathrm{a}} &= \widetilde{\mathbf{C}}_{\mathrm{a}}\mathbf{E}_{\mathrm{a}} \\ \widetilde{\mathbf{H}}_{\mathrm{dd}}\widetilde{\mathbf{C}}_{\mathrm{d}} &= \widetilde{\mathbf{C}}_{\mathrm{d}}\mathbf{E}_{\mathrm{d}} \end{aligned} \quad . \tag{3.9}$$

Here, $\mathbf{E}_{\mathrm{a}}$ and $\mathbf{E}_{\mathrm{d}}$ are diagonal matrices with fragment eigenenergies $\epsilon_{\mathrm{a},i}$ and $\epsilon_{\mathrm{d},j}$, respectively. Following convention [24], we label energy matrices $\mathbf{E}_{\mathrm{a}}$, $\mathbf{E}_{\mathrm{d}}$ without tilde as they are unchanged by basis transformations.

These eigenstates differ from those of the isolated systems, as they include interactions between the fragments. The resulting fragment eigenvectors, contained in $\widetilde{\mathbf{C}}_{\mathrm{a}}$ and $\widetilde{\mathbf{C}}_{\mathrm{d}}$, then define a transformation matrix

$$\widetilde{\mathbf{C}}_{\mathbf{t}} = \begin{pmatrix} \widetilde{\mathbf{C}}_{\mathrm{a}} & \mathbf{0} \\ \mathbf{0} & \widetilde{\mathbf{C}}_{\mathrm{d}} \end{pmatrix}, \tag{3.10}$$

which can be used to project the Hamiltonian $\widetilde{\mathbf{H}}$ of the combined system onto the basis of diabatic fragment eigenstates

$$\overline{\mathbf{H}}_{\mathrm{diag}} = \widetilde{\mathbf{C}}_{\mathbf{t}}^{\dagger}\widetilde{\mathbf{H}}\widetilde{\mathbf{C}}_{\mathbf{t}} \quad , \tag{3.11}$$

yielding the partially-diagonalized form

$$\overline{\mathbf{H}}_{\mathrm{diag}} = \left(\begin{array}{ccc|ccc} \epsilon_{\mathrm{a},1} & 0 & \cdots & & & \\ 0 & \epsilon_{\mathrm{a},2} & \cdots & & \overline{\mathbf{H}}_{\mathrm{ad}} & \\ \vdots & \vdots & \ddots & & & \\ \hline & & & \epsilon_{\mathrm{d},1} & 0 & \cdots \\ & \overline{\mathbf{H}}_{\mathrm{da}} & & 0 & \epsilon_{\mathrm{d},2} & \cdots \\ & & & \vdots & \vdots & \ddots \end{array}\right) \quad . \tag{3.12}$$

Diabatic orbital energies $\epsilon_{\mathrm{a},i}$, $\epsilon_{\mathrm{d},j}$ appear in the diagonal blocks of $\overline{\mathbf{H}}_{\mathrm{diag}}$ and are the same as those in Equation (3.9), while the off-diagonal blocks $\overline{\mathbf{H}}_{\mathrm{da}}$ and $\overline{\mathbf{H}}_{\mathrm{ad}}$ now contain diabatic donor-acceptor couplings.

In the global orthogonal basis, diabatic donor and acceptor eigenstates $|\widetilde{\psi}_{\mathrm{d},j}\rangle$,$|\widetilde{\psi}_{\mathrm{a},i}\rangle$ are contained as columns of $\widetilde{\mathbf{C}}_{\mathbf{t}}$, which we shall label $\widetilde{\mathbf{C}}'_{\mathrm{a},i}$, $\widetilde{\mathbf{C}}'_{\mathrm{d},j}$. Using Equation (3.5), the diabats and couplings can then also be rewritten in the original non-orthogonal basis:

$$\begin{aligned}\overline{\mathbf{H}}_{\mathrm{ad},ij} &= \widetilde{\mathbf{C}}'^{\dagger}_{\mathrm{a},i}\widetilde{\mathbf{H}}\widetilde{\mathbf{C}}'_{\mathrm{d},j} \\ &= (\mathbf{S}^{1/2}\mathbf{C}_{\mathrm{a},i})^{\dagger}\widetilde{\mathbf{H}}(\mathbf{S}^{1/2}\mathbf{C}_{\mathrm{d},j}) \\ &= \mathbf{C}^{\dagger}_{\mathrm{a},i}\mathbf{S}^{1/2}\widetilde{\mathbf{H}}\mathbf{S}^{1/2}\mathbf{C}_{\mathrm{d},j} \\ &= \mathbf{C}^{\dagger}_{\mathrm{a},i}\mathbf{H}_{\mathrm{KS}}\mathbf{C}_{\mathrm{d},j}\end{aligned} \quad . \tag{3.13}$$

Table 3.1: Diabatic POD wavefunctions for a Benzene dimer and using the PBE functional. Shown is the acceptor state on the Benzene on the left at a dimer separation of 5Å separation for Dunning cc-pVNZ basis sets. Tail contributions are visible on the donor Benzene fragment on the right at the low plotted isovalue contour at 0.0003 [$a_0^{-3/2}$]. The respective coupling values are given in meV below. The reference value from the Hab11 database is 51.7 meV [74]. Reused with permission from Reference [1]. Copyright 2020 American Chemical Society.

cc-pVDZ	cc-pVTZ	cc-pVQZ
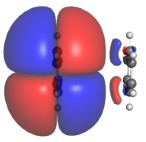	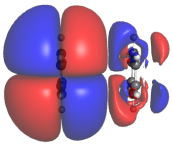	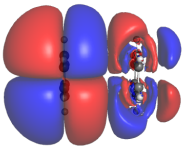
33.9	34.8	30.4

By construction, the POD diabats $\mathbf{C}_{\mathrm{a},i}$ and $\mathbf{C}_{\mathrm{d},j}$ (equivalent to $\widetilde{\mathbf{C}}'_{\mathrm{a},i}$ and $\widetilde{\mathbf{C}}'_{\mathrm{d},j}$) are orthogonal. However, they are in general not confined to their respective fragments. We see from Equation (3.4) that a basis function $\widetilde{\varphi}_n$ centered on one fragment may contain contributions from φ_j on the opposing fragment. Orthogonalization introduces a small but finite amount of mixing in the fragments' respective basis sets, meaning diabatic states constructed as the solutions to the respective blocks of Equation (3.9) are not strictly localized. The coupling element in Equation (3.13) thus represents the coupling between these slightly delocalized diabats. Similarly, eigenvalues $\epsilon_{\mathrm{a},i}$, $\epsilon_{\mathrm{d},j}$ are energies of these delocalized states.

This is demonstrated in Table 3.1 which shows the diabatic POD acceptor state for a dimer of Benzene.

We use the Dunning correlation-consistent basis sets [109] for demonstration purposes, as these contain progressively more diffuse functions from cc-pVDZ to cc-pV5Z and are convenient for comparison with other studies. As we consider hole transport, the acceptor state considered here is the diabatic highest-occupied molecular orbital (HOMO) of the left fragment of the dimer. A very small isovalue has been chosen to reveal the acceptor wavefunction tails which clearly contain contributions from basis functions of the donor atoms. As

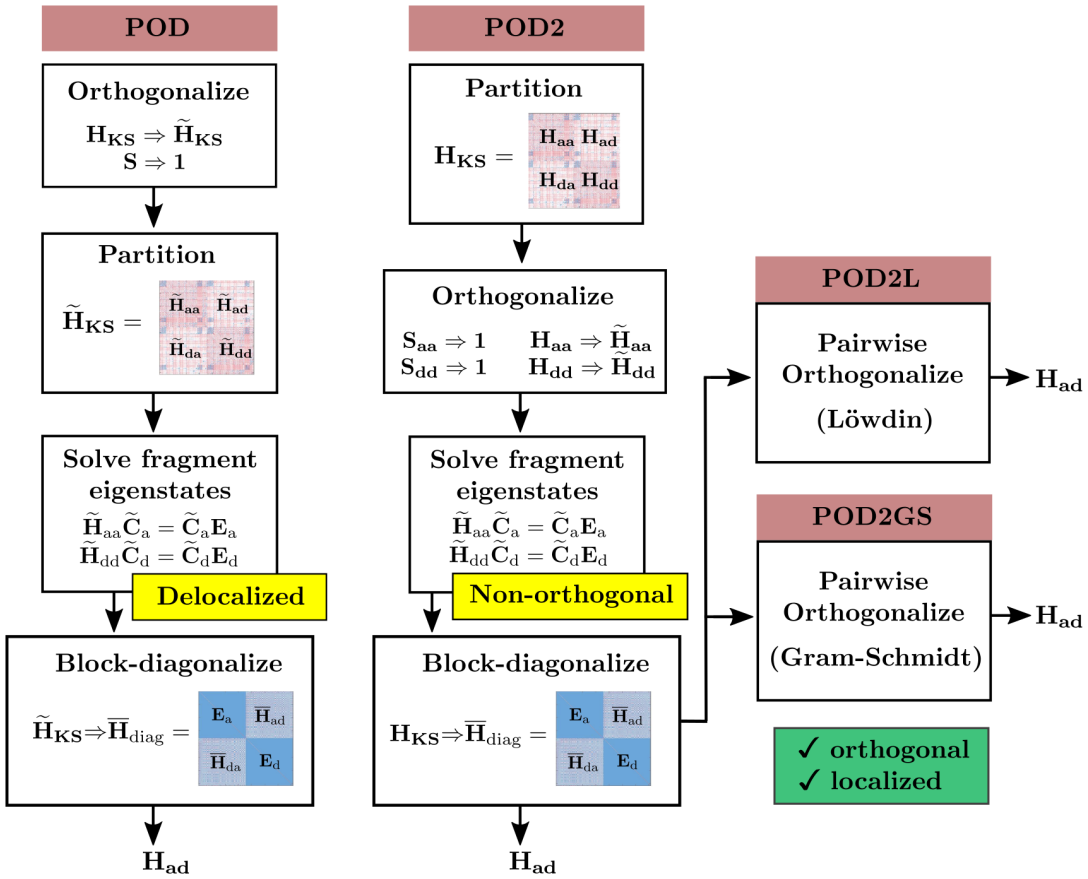

Figure 3.2: Flowcharts of four projection-operator diabatization schemes to calculate diabatic states and couplings from the Kohn-Sham Hamiltonian. Reused with permission from Reference [1]. Copyright 2020 American Chemical Society.

the basis set becomes more diffuse, from cc-pVDZ to cc-pVQZ, there is a greater degree of mixing in the basis and concomitant delocalization of the diabat. This further leads to a nontrivial change in coupling strength H_{ad} which, notably, seems to show no convergence with basis size.

We can generally expect the severity of this mixing in POD to depend on the fragment separation, with well-separated fragments experiencing less mixing. This is again demonstrated in Figure 3.3 for the Benzene dimer. While the more compact cc-pVDZ basis has reasonable accuracy at all separations, the inclusion of more diffuse basis functions leads to an underestimation of couplings, with the effect magnified at smaller separations. This issue of mixing basis functions has been recognized since the inital publication of the method [24], where the authors point out that care should be taken to check the character of diabatic states.

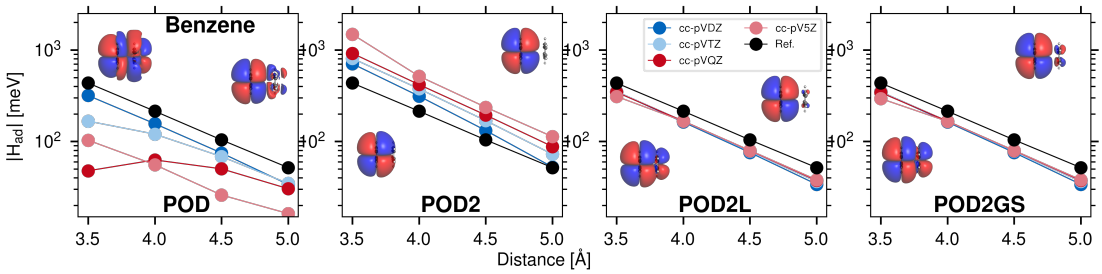

Figure 3.3: Calculated coupling values for the Benzene dimer at various distances. Shown is data for Dunning basis sets, the PBE functional and the different POD and POD flavors discussed in the text. The black data points correspond to the reference from the Hab11 database.[74] Also shown are the diabatic acceptor HOMO states for cc-pVTZ basis at 3.5 and 5Å separations. Reused with permission from Reference [1]. Copyright 2020 American Chemical Society.

Table 3.2: Diabatic acceptor state for a Benzene dimer at 5Å separation, and using the PBE functional and an extensive cc-pVTZ basis. Shown are the results for POD and the different POD flavors discussed in the text. The same isocontour value of 0.0003 [$a_0^{-3/2}$] as in Table I is used for comparison, revealing the varying degree of tail intermixing obtained in the different flavors. The respective coupling values are given in meV below. The reference value from the Hab11 database is 51.7 meV [74]. Reused with permission from Reference [1]. Copyright 2020 American Chemical Society.

POD	POD2	POD2L	POD2GS
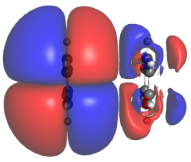	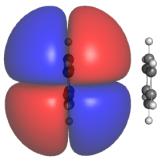	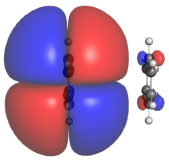	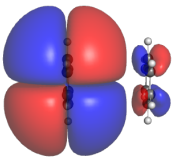
34.8	72.5	36.4	36.4

POD2: A localization-enforced flavor

Given these shortcomings, it is natural to ask whether the steps in POD could be rearranged to improve the partitioning of Hilbert space and avoid mixing of the fragments' basis functions. In this spirit, we try an augmented POD flavor which we name POD2 and summarize in Figure 3.2.

In contrast to POD, the Hilbert space and thus the KS Hamiltonian $\mathbf{H}_{\mathrm{KS}}$ and overlap $\mathbf{S}$ matrices are partitioned into donor and acceptor blocks before orthogonalization.

$$\mathbf{H}_{\mathrm{KS}} = \begin{pmatrix} \mathbf{H}_{\mathrm{aa}} & \mathbf{H}_{\mathrm{ad}} \\ \mathbf{H}_{\mathrm{da}} & \mathbf{H}_{\mathrm{dd}} \end{pmatrix} \qquad \mathbf{S} = \begin{pmatrix} \mathbf{S}_{\mathrm{aa}} & \mathbf{S}_{\mathrm{ad}} \\ \mathbf{S}_{\mathrm{da}} & \mathbf{S}_{\mathrm{dd}} \end{pmatrix} \quad . \tag{3.14}$$

Acceptor and donor blocks then form their own generalized eigenproblems in the nonorthogonal atom-centered basis:

$$\begin{aligned} \mathbf{H}_{\mathrm{aa}}\mathbf{C}_{\mathrm{a}} &= \mathbf{S}_{\mathrm{aa}}\mathbf{C}_{\mathrm{a}}\mathbf{E}_{\mathrm{a}} \\ \mathbf{H}_{\mathrm{dd}}\mathbf{C}_{\mathrm{d}} &= \mathbf{S}_{\mathrm{dd}}\mathbf{C}_{\mathrm{d}}\mathbf{E}_{\mathrm{d}} \end{aligned} \quad . \tag{3.15}$$

These local eigenproblems are consecutively transformed for convenience into their own orthogonal basis with the Löwdin [108] scheme:

$$\begin{aligned} \mathbf{X}_{\mathrm{a}} &= \mathbf{S}_{\mathrm{aa}}^{-1/2} & \mathbf{X}_{\mathrm{d}} &= \mathbf{S}_{\mathrm{dd}}^{-1/2} \\ \widetilde{\mathbf{C}}_{\mathrm{a}} &= \mathbf{X}_{\mathrm{a}}^{-1}\mathbf{C}_{\mathrm{a}} & \widetilde{\mathbf{C}}_{\mathrm{d}} &= \mathbf{X}_{\mathrm{d}}^{-1}\mathbf{C}_{\mathrm{d}} \end{aligned} \quad . \tag{3.16}$$

Similarly, the local Hamiltonians are transformed to the local orthogonal basis:

$$\begin{aligned} \widetilde{\mathbf{H}}_{\mathrm{aa}} &= \mathbf{X}_{\mathrm{a}}^{\dagger}\mathbf{H}_{\mathrm{aa}}\mathbf{X}_{\mathrm{a}} \\ \widetilde{\mathbf{H}}_{\mathrm{dd}} &= \mathbf{X}_{\mathrm{d}}^{\dagger}\mathbf{H}_{\mathrm{dd}}\mathbf{X}_{\mathrm{d}} \end{aligned} \tag{3.17}$$

Thus we have the new local eigenproblems

$$\begin{aligned} \widetilde{\mathbf{H}}_{\mathrm{aa}}\widetilde{\mathbf{C}}_{\mathrm{a}} &= \widetilde{\mathbf{C}}_{\mathrm{a}}\mathbf{E}_{\mathrm{a}} \\ \widetilde{\mathbf{H}}_{\mathrm{dd}}\widetilde{\mathbf{C}}_{\mathrm{d}} &= \widetilde{\mathbf{C}}_{\mathrm{d}}\mathbf{E}_{\mathrm{d}} \end{aligned} \quad . \tag{3.18}$$

Here, $\mathbf{E}_{\mathrm{d}}$, $\mathbf{E}_{\mathrm{a}}$ are diagonal matrices containing local eigenenergies $\epsilon_{\mathrm{d},j}$, $\epsilon_{\mathrm{a},i}$, which are again unchanged by the orthogonalization. Matrices $\widetilde{\mathbf{C}}_{\mathrm{d}}$, $\widetilde{\mathbf{C}}_{\mathrm{a}}$ contain the diabatic eigenvectors in their respective orthogonal basis set. Again, these differ from isolated fragment states as they originate from the Hamiltonian of the combined system.

The fragment eigenstates can be represented in the original non-orthogonal basis: $\mathbf{C}_{\mathrm{a}} = \mathbf{S}_{\mathrm{aa}}^{-1/2}\widetilde{\mathbf{C}}_{\mathrm{a}}$. We now form the transformation matrix

$$\mathbf{C}_{\mathbf{t}} = \begin{pmatrix} \mathbf{C}_{\mathrm{a}} & \mathbf{0} \\ \mathbf{0} & \mathbf{C}_{\mathrm{d}} \end{pmatrix} \tag{3.19}$$

and project the original Hamiltonian $\mathbf{H}_{\mathrm{KS}}$ onto the fragment eigenstates in the original basis:

$$\overline{\mathbf{H}}_{\mathrm{diag}} = \mathbf{C}_{\mathbf{t}}^{\dagger}\mathbf{H}_{\mathrm{KS}}\mathbf{C}_{\mathbf{t}} \quad . \tag{3.20}$$

This yields the partially-diagonalized form

$$\overline{\mathbf{H}}_{\mathrm{diag}} = \left(\begin{array}{ccc|ccc} \epsilon_{\mathrm{a},1} & 0 & \cdots & & & \\ 0 & \epsilon_{\mathrm{a},2} & \cdots & & \overline{\mathbf{H}}_{\mathrm{ad}} & \\ \vdots & \vdots & \ddots & & & \\ \hline & & & \epsilon_{\mathrm{d},1} & 0 & \cdots \\ & \overline{\mathbf{H}}_{\mathrm{da}} & & 0 & \epsilon_{\mathrm{d},2} & \cdots \\ & & & \vdots & \vdots & \ddots \end{array}\right) \quad , \tag{3.21}$$

where the adiabatic Hamiltonian $\mathbf{H}_{\mathrm{KS}}$ has been expressed in the basis of diabatic fragment eigenstates with energies $\epsilon_{\mathrm{a},i}$ and $\epsilon_{\mathrm{d},j}$. Off-diagonal elements $\overline{\mathbf{H}}_{\mathrm{ad}}$ emerge as the diabatic couplings.

The advantage of the POD2 flavor is that the partitioning of basis functions before orthogonalization prevents any inter-fragment mixing, and diabatic states are well localized to their respective fragments. This is clearly seen in Table 3.2, where diabats for the Benzene dimer are compared. The eigenvalues $\epsilon_{\mathrm{d},i}$, $\epsilon_{\mathrm{a},j}$ now also correspond to localized diabatic states. However, some ambiguity in the definition of the couplings results. Considering the coupling between two states, we find, in contrast to Equation (3.13) that

$$\begin{aligned} \overline{\mathbf{H}}_{\mathrm{ad,ij}} &= \mathbf{C}_{\mathrm{a,i}}^{\dagger}\mathbf{H}_{\mathrm{ad}}\mathbf{C}_{\mathrm{d,j}} \\ &= (\mathbf{S}_{\mathrm{a}}^{-1/2}\widetilde{\mathbf{C}}_{\mathrm{a,i}})^{\dagger}\mathbf{H}_{\mathrm{ad}}(\mathbf{S}_{\mathrm{d}}^{-1/2}\widetilde{\mathbf{C}}_{\mathrm{d,j}}) \\ &= \widetilde{\mathbf{C}}_{\mathrm{a,i}}^{\dagger}\mathbf{S}_{\mathrm{a}}^{-1/2}\mathbf{H}_{\mathrm{ad}}\mathbf{S}_{\mathrm{d}}^{-1/2}\widetilde{\mathbf{C}}_{\mathrm{d,j}} \\ &\neq \widetilde{\mathbf{C}}_{\mathrm{a,i}}^{\dagger}\widetilde{\mathbf{H}}\widetilde{\mathbf{C}}_{\mathrm{d,j}} \end{aligned} \quad . \tag{3.22}$$

The couplings thus cannot be expressed according to their definition: as an integral of two states over some global Hamiltonian operator in a common basis. The donor and acceptor eigenstates exist in different bases and, notably, are not orthogonal. Consequently, the cross terms $\overline{\mathbf{H}}_{\mathrm{ad}}$ are not as well-defined as in Equation (3.13) of the original POD method.

In summary, while POD offers well-defined couplings between orthogonal but delocalized diabats, POD2 now offers localized but non-orthogonal diabats, with some ambiguity in the meaning of the couplings. Nevertheless, Figure 3.3 shows that while POD2 overestimates couplings, it already exhibits a more consistent behavior than POD with respect to the basis set.

Methods POD2L and POD2GS

The situation for POD2 and its non-orthogonal, fragment-localized states resembles that of the FODFT [69, 70] and DIPRO [99] schemes, where diabatic couplings are derived simply from the (non-orthogonal) molecular orbitals of the isolated fragments. Motivated by the success of FODFT, and the close resemblance of our POD2 diabats to actual fragment MOs, we adopt a similar approach [98, 99]. Specifically, FODFT performs an orthogonalization of the fragment-based diabats in order to achieve couplings and on-site energies which resemble the physical parameters of a tight-binding model and better match experiment.

Similarly, we here parametrize a tight-binding Hamiltonian by using the diabats of POD2. In the block-diagonalized Hamiltonian of Equation (3.21) we can already identify site energies, couplings and state overlaps for the diabatic frontier states (ψ_a,ψ_d) which correspond to $\epsilon_{\{a,d\}}$, $H_{\{ad,da\}}$ and $S_{\{ad,da\}}$ in a two-state Hamiltonian.

$$\mathbf{H} = \begin{pmatrix} \epsilon_a & H_{ad} \\ H_{da} & \epsilon_d \end{pmatrix} \qquad \mathbf{S} = \begin{pmatrix} 1 & S_{ad} \\ S_{da} & 1 \end{pmatrix} \quad . \tag{3.23}$$

The meaning of H_{ad} and $\epsilon_{a,d}$ are not the same as in a tight-binding model, however, as the POD2 orbitals are not orthogonal. This can be addressed by performing a Löwdin-transformation to a basis of orthogonal molecular orbitals , yielding an effective matrix:

$$\widetilde{\mathbf{H}}^{\text{eff}} = \mathbf{S}^{-1/2}\mathbf{H}\mathbf{S}^{-1/2} \tag{3.24}$$

Effective coupling elements H_{ad}^{eff} which are consistent with those in tight-binding can now be extracted from $\widetilde{\mathbf{H}}^{\text{eff}}$ or, equivalently, solved directly from the original terms:

$$H_{ad}^{\text{eff}} = \frac{H_{ad} - \frac{1}{2}(\epsilon_a + \epsilon_d)S_{ad}}{1 - S_{ad}^2} \quad . \tag{3.25}$$

We see that the effective coupling H_{ad}^{eff} reduces to H_{ad} if the original states are orthogonal (S_{ad}=0). Given their now orthogonal diabatic basis, the effective couplings H_{ad}^{eff} can be directly compared to the couplings H_{ad} calculated with POD or POD2. We will refer to this Löwdin modification of the POD2 scheme as POD2L, and we will henceforth refer to the effective couplings H_{ad}^{eff} as H_{ad} of the POD2L flavor. The advantage over FODFT is now that these POD2-based coupling elements originate from a converged dimer Hamiltonian and should therefore carry some physics of the inter-fragment interactions.

Alternatively, one could achieve orthogonalization of the POD2 diabatic basis (ψ_a, ψ_d) through the Gram-Schmidt procedure, which for a simple 2-state case yields

$$\begin{aligned} \psi'_d &= \begin{bmatrix} 1 \\ 0 \end{bmatrix} \\ \psi'_a &= \frac{1}{\sqrt{M}} \left(\begin{bmatrix} 0 \\ 1 \end{bmatrix} - S_{ad} \begin{bmatrix} 1 \\ 0 \end{bmatrix} \right) \end{aligned} \tag{3.26}$$

in the basis (ψ_a, ψ_d). The wavefunction ψ'_a requires normalization, indicated here by *M*. We can then create a (2×2) transformation matrix $\mathbf{C_t}$ containing as columns the orthogonalized vectors ψ'_d and ψ'_a:

$$\mathbf{C_t} = \begin{pmatrix} 1 & \psi'_{a,1} \\ 0 & \psi'_{a,2} \end{pmatrix} \tag{3.27}$$

Finally, the transformed Hamiltonian in this basis is

$$\widetilde{\mathbf{H}}^{\text{eff}} = \mathbf{C_t^\dagger H C_t} \tag{3.28}$$

from which effective couplings and on-site energies can again be read. We will call this flavor POD2GS and also refer to these effective couplings simply as H_{ad} ongoing.

The advantage of GS orthogonalization is that it preserves the fragment-localized character of the state ψ_d (here the donor) perfectly, shifting any distortion to the acceptor ψ'_a. For asymmetric systems such as e.g. surfaces with adsorbates, this allows us to give preferential treatment to the diabat of the smaller fragment, which under Löwdin would experience a proportionally much higher distortion of its character.

Table 3.2 also compiles the afore discussed acceptor diabats for the Benzene dimer showcase for the POD2L and POD2GS flavors. Due to the orthogonalization, the states are a bit delocalized over both fragments, yet less so than in the original POD method. In POD2L, acceptor and donor (not shown) diabats are symmetric. For POD2GS, we have chosen to preserve the character of the donor orbital ψ'_d (not shown), which then remains identical to that of POD2. Due to the asymmetry of the Gram-Schmid orthogonalization, in POD2GS the acceptor state ψ'_a is slightly more delocalized than in the POD2L case. As seen in Figure 3.3, POD2L and POD2GS are well-behaved over different separations and basis sets, and, as shown below, their accuracy will depend now primarily on the choice of exchange-correlation functional. Furthermore, even though not in the focus of this work, both flavors additionally yield effective site-energies.

We consider next how these methods may be applied on surface systems.

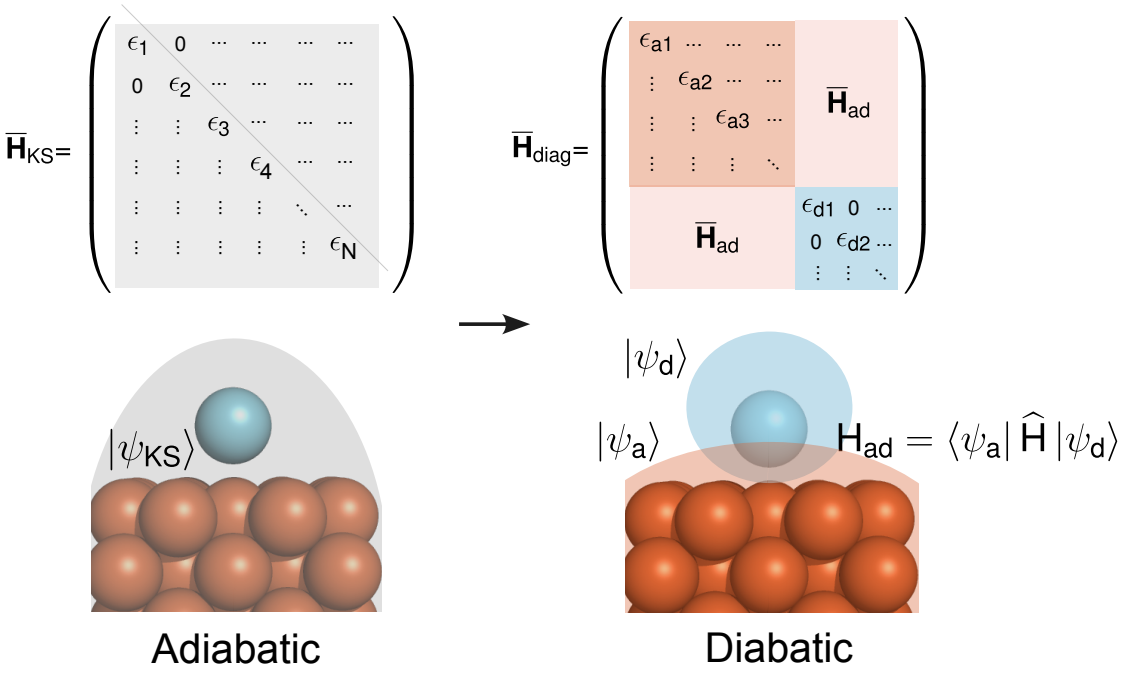

Figure 3.4: Diabatic description of an adsorbed system.

3.1.2 Surface Systems

The following section is adapted with permission from Reference [2] and has been submitted for publication. After it is published, it will be found at The Journal of Chemical Physics.

For periodic surface systems, we may apply the improved Projection Operator Diabatization schemes developed for molecules above with some modification. The asymmetric nature of the Gram-Schmidt orthogonalization method makes it well suited to treating adsorbates on surfaces. On a metal, a quasi-continuum of acceptor states must be considered. We manage this by considering each donor-acceptor state pair seperately.

The diabatic donor $|\psi_d\rangle$ and acceptor $\{|\psi_a\rangle\}$ states are the key inputs to compute the desired diabatic site energies and couplings, which are now $\mathbf{k}$-dependent:

$$\epsilon_{a,\mathbf{k}} = \langle\psi_{a,\mathbf{k}}|\hat{H}_{\mathbf{k}}|\psi_{a,\mathbf{k}}\rangle \tag{3.29a}$$

$$\epsilon_{d,\mathbf{k}} = \langle\psi_{d,\mathbf{k}}|\hat{H}_{\mathbf{k}}|\psi_{d,\mathbf{k}}\rangle \tag{3.29b}$$

$$H_{ad,\mathbf{k}} = \langle\psi_{a,\mathbf{k}}|\hat{H}_{\mathbf{k}}|\psi_{d,\mathbf{k}}\rangle\,. \tag{3.29c}$$

Newns [53] originally defined $|\psi_d\rangle$ and $\{|\psi_a\rangle\}$ simply as the eigenfunctions of non-interacting (isolated) donor and acceptor fragments. We will term this the ($frag_d$,$frag_a$) diabatic basis, consisting in the present application case of the eigenstates of an infinitely periodic isolated Argon layer and an isolated metal surface, both described in a periodic-boundary condition supercell.

For a more quantitative description of the ET process, we instead here rely on a diabatization procedure, which accounts for some weak hybridization between the donor and acceptor system. Specifically, we will draw on our previously described Projection-Operator Diabatization approach, which is based on the partitioning and block-diagonalization of the Kohn-Sham DFT Hamiltonian of the full interacting system (POD2), and the subsequent orthogonalization of the diabats via a Gram-Schmidt (GS) procedure (POD2GS) [1].

To calculate the electron transfer (ET) from weakly physisorbed Argon to a metal surface, we thus generate a POD2 diabatic spectrum $\{|\psi_{\mathrm{d}}\rangle\}$ for the Argon donor by extracting and diagonalizing its block in the Hamiltonian of the combined system (Figures 3.4 and **??**b below). This POD2 spectrum is found to contain a suitable Argon 4*s*-like lowest unoccupied molecular orbital (LUMO) state, and we refer to this donor state as $\mathrm{POD2_d}$. Keeping to the original spirit of Newns, this is combined with the eigenstates of the isolated surface to yield the ($\mathrm{POD2_d}$,$\mathrm{frag_a}$) diabatic basis. Note that a full POD2-based approach where also the acceptor is described in the interacting picture ($\mathrm{POD2_d}$,$\mathrm{POD2_a}$) would not show appreciable differences to the ($\mathrm{POD2_d}$,$\mathrm{frag_a}$) representation, due to the acceptor being only very weakly influenced by the donor.

In neither the ($\mathrm{frag_d}$,$\mathrm{frag_a}$) nor the ($\mathrm{POD2_d}$,$\mathrm{frag_a}$) basis, the donor and acceptor states are necessarily orthogonal to each other, as they should be for a numerically stable and formally correct value of $\mathrm{H_{ad}}$ according to tight binding theory [1, 98, 99]. To remove any finite overlap

$$\mathrm{S_{ad,\mathbf{k}}} = \langle \psi_{\mathrm{a},\mathbf{k}} | \psi_{\mathrm{d},\mathbf{k}} \rangle \tag{3.30}$$

we therefore GS orthogonalize each donor-acceptor state pair [1]. As a consequence, the acceptor acquires a small orthogonalization tail, and the acceptor states are no longer orthogonal with respect to each other. For the present application, the effect of this orthogonalization is relatively small though. Consistent with earlier work [82], the $\mathrm{POD2_d}$ donor state has a slightly hybridized $4s4p_z$ nodal structure (cf. Figure 4.12 below) and is already nearly orthogonal to the surface as a response to Pauli repulsion interactions. The orthogonalization leads thus only to a slight reduction of the electronic couplings, similar to the findings in earlier studies of molecular systems [1, 98]. The effect of orthogonalization on couplings is shown in Figure B3. In the following we shall refer to the two orthogonalized diabatic basis sets as ($\mathrm{frag_d}$,$\mathrm{frag_a}$)GS and ($\mathrm{POD2_d}$,$\mathrm{frag_a}$)GS and compare the effect of the diabatization on the electronic couplings and ET lifetimes below.

Orthogonalization Procedure

The orthogonalization of diabats is found in the surface as well as molecular dimer systems to reduce the magnitude of couplings and improve their agreement with reference values [1, 98]. The chemical significance of overlap and orthogonalization is discussed widely in the literature [108, 110]. In the orthogonalization procedure of ($\mathrm{POD2_d}$,$\mathrm{frag_a}$)GS, the effective couplings formally become dependent on the donor site energy ϵ_{d}, as well as the overlap matrix element [1]: $\mathrm{H_{ad}^{eff}}$=$\mathrm{H_{ad}^{eff}}(\mathrm{H_{ad}}, \mathrm{S_{ad}}, \epsilon_{\mathrm{d}})$. The interpretation of the WDOS as a

resonant ET rate is thus formally valid at the resonance energy ϵ_d, and approximative elsewhere. Meanwhile, the chemisorption function/WDOS itself remains well-defined over the full energy scale.

Prior to orthogonalization, we have the non-orthogonal donor $|\psi_d\rangle$ and acceptor state $|\psi_a\rangle$, their site energies ϵ_a and ϵ_d, their coupling H_{ad} and their overlap $S_{ad} = \langle\psi_a|\psi_d\rangle \neq 0$, $S_{ad}=\overline{S_{da}}$, $\mathbf{S} = \mathbf{S}^\dagger$, as defined in equations (5-6) of the main text. This 2-state system forms a (complex-valued) 2×2 matrix:

$$\mathbf{H} = \begin{pmatrix} \epsilon_a & H_{ad} \\ H_{da} & \epsilon_d \end{pmatrix} \qquad \mathbf{S} = \begin{pmatrix} 1 & S_{ad} \\ S_{da} & 1 \end{pmatrix} \quad . \tag{3.31}$$

A simple 2-state Gram-Schmidt orthogonalization process, where the acceptor is orthogonalized with respect to the donor, is

$$\begin{aligned} \psi'_d &= \begin{bmatrix} 0 \\ 1 \end{bmatrix} \\ \psi'_a &= \frac{1}{\sqrt{1-|S_{ad}|^2}} \left(\begin{bmatrix} 1 \\ 0 \end{bmatrix} - S_{da} \begin{bmatrix} 0 \\ 1 \end{bmatrix} \right) \end{aligned} \tag{3.32}$$

in the basis (ψ_a, ψ_d), after which $\langle\psi'_a|\psi'_d\rangle$=0. We can then create a (2×2) transformation matrix $\mathbf{C_t}$ containing as columns the orthogonalized vectors ψ'_a and ψ'_d:

$$\mathbf{C_t} = \begin{pmatrix} \psi'_{a,1} & 0 \\ \psi'_{a,2} & 1 \end{pmatrix} \tag{3.33}$$

Finally, the transformed Hamiltonian in this basis is

$$\widetilde{\mathbf{H}}^{\text{eff}} = \mathbf{C_t^\dagger H C_t} \tag{3.34}$$

from which effective couplings of Equation (5c) and on-site energies of equations (5a) and (5b) of the main text can again be read.

In this scheme, the donor wavefunction and site energy are preserved: $\psi'_d = \psi_d$, $\epsilon'_d = \epsilon_d$. The acceptor wavefunction has changed, and now contains a contribution on the donor. The acceptor site energy and effective coupling will thus change from their original values according to the strength of the distortion, as determined by the overlap S_{ad}. It is straightforward to show that the effective site energy and coupling are

$$\epsilon'_a = \frac{1}{1-|S_{ad}|^2}(\epsilon_a + \epsilon_d |S_{da}|^2 - H_{ad}S_{da} - H_{da}S_{ad}) \tag{3.35}$$

and

$$H'_{ad} = H^{\text{eff}}_{ad} = \frac{1}{\sqrt{1-|S_{ad}|^2}}(H_{ad} - S_{ad}\epsilon_d). \tag{3.36}$$

Here we see how the effective couplings are reduced in magnitude from their value prior to orthogonalization, by a factor determined by the overlap S_{ad} and the site energy of the donor ϵ_d. Important here is how couplings vary with the site energy of the resonance. This is key to the interpretation of the chemisorption (described below), which has been calculated for a fixed value of the parameter ϵ_d) as a resonant ET rate at energies other than the resonance ϵ_d. For small S_{ad} and at energies near ϵ_d, it is justified to view the chemisorption function (described below) as an approximate ET rate. However, formally the Golden Rule interpretation is only valid at ϵ_d. For the present hybridized $4s4p_z$ POD2 donor state, which has small overlap with the surface, the interpretation of the WDOS as an ET rate near the resonance is justified. In the more general case, however, caution should be exercised.

Our orthogonalization procedure, which is applied in pair-wise fashion, leaves the ($frag_a$, $POD2_d$)GS acceptor spectrum formally non-orthogonal to itself. The acceptor block of the Hamiltonian is thus only approximately diagonalized while the $POD2_d$ donor block is perfectly diagonalized (Figure 3.4). As such, this is only an approximative orthogonalization scheme. We observe overlaps within the acceptor spectrum to be small, however, and thus consider it a secondary concern. It is rather more important to ensure the orthogonality between the donor and acceptor diabats. Enforcing the orthogonality among the acceptor diabats themselves will be relegated to future work. Future applications in systems with stronger donor-acceptor overlap (e.g. chemisorped systems) may need a more rigorous treatment of orthogonalization.

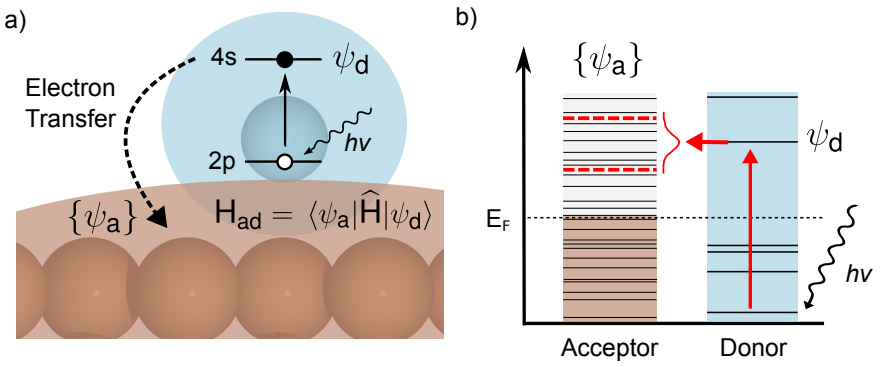

Figure 3.5: a) Diagram of the core-excited electron transfer system of an Ar atom adsorbed on a transition metal surface. Ar is thereby optically core-excited into a 4s donor state ψ_d which can then decay into the spectrum of surface acceptor states $\{\psi_a\}$ b) Schematic energy diagram of the process. This figure has been reused with permission from Reference [2] and has been submitted for publication. After it is published, it will be found at The Journal of Chemical Physics.

3.2 The Newns-Anderson Chemisorption Function

The following section is adapted with permission from Reference [2] and has been submitted for publication. After it is published, it will be found at The Journal of Chemical Physics.

Having above described the calculation of electronic couplings on surfaces, we may now consider how these may be used in the calculation of a Newns-Anderson chemsiorption function within a periodic DFT framework. We will simultaneously be describing the core-excited electron transfer system of Figure 3.5.

The chemisorption function (Equation 2.26) describes the energetic broadening or linewidth of an adsorbate frontier state $|\psi_d\rangle$ (donor) as it interacts with a continuum of states $\{|\psi_a\rangle\}$ (acceptors) on a surface, as in Figure 3.5:

$$\begin{aligned}\Delta(\epsilon) &= \pi \sum_a |\langle\psi_a|\hat{H}|\psi_d\rangle|^2 \delta(\epsilon - \epsilon_a) \\ &= \pi \sum_a |H_{ad}|^2 \delta(\epsilon - \epsilon_a). \end{aligned} \tag{3.37}$$

Here, $\hat{H}$ is the Hamiltonian of the full system and ϵ_a the energy of the acceptor states. Its relation to CT processes is given, in a weak coupling regime, by the Golden Rule transition for a donor state of energy ϵ_d:

$$\Gamma_{d\to a}(\epsilon_d) = \frac{2}{\hbar}\Delta(\epsilon = \epsilon_d)\ , \tag{3.38a}$$

with the lifetime then given by

$$\tau_d(\epsilon_d) = \Gamma_{d\to a}(\epsilon_d)^{-1}\ . \tag{3.38b}$$

The chemisorption function thus emerges as the half-width at half-maximum (HWHM) of a Lorentzian broadening of the energy level ϵ_d. It is also referred to as the weighted density of states (WDOS) [97], as well as a hybridization function [**Bahlke2021**], which emphasizes that it can in principle be evaluated at any energy ϵ. Of course, the relation to the lifetime of the donor state strictly holds only for $\Delta(\epsilon_d)$, but approximately one can also evaluate the chemisorption function for other energies, for example at the experimental resonance energy rather at a computed donor state energy ϵ_d.

Importantly, the chemisorption function thus allows to approximately explore and predict the lifetime as a function of the energy of the donor state. To adapt its definition for practical use in a periodic DFT supercell model for the extended metal surface, two modifications are needed. First, due to the finite nature of periodic slab models and the employed basis set, only a discrete quasicontinuum of N levels is present. We therefore replace the Dirac δ-functions in equation (3.37) by artificial broadening functions, $g_\sigma(\epsilon - \epsilon_a)$, to give $\Delta(\epsilon)$ a smooth and continuous behavior. Specifically, we choose a Lorentzian distribution with half-width at half-maximum (HWHM) σ=0.2 eV, and demonstrate that the determined lifetimes do not depend on the choice of the latter parameter. Second, addressing the Bloch description of the electronic states in supercell models, the explicit state summation in equation (3.37) needs to be replaced by an appropriate integration over the system's Brillouin zone (BZ) [111]. Already including the Lorentzian smoothing, we correspondingly arrive at **k**-resolved chemisorption functions

$$\Delta_{\mathbf{k}}(\epsilon) = \pi \sum_{a}^{N} |H_{ad,\mathbf{k}}|^2 g_\sigma(\epsilon_{\mathbf{k}} - \epsilon_{a,\mathbf{k}}) \,, \tag{3.39}$$

with the full chemisorption then resulting from BZ integration [112]

$$\Delta(\epsilon) = \frac{1}{\Omega_{BZ}} \int_{\Omega_{\mathbf{BZ}}} \Delta_{\mathbf{k}}(\epsilon) d\mathbf{k} \,. \tag{3.40}$$

In practice, this integral is performed by summing over the **k**-points with weights $w_{\mathbf{k}}$ of a regular Monkhorst-Pack grid in the irreducible BZ [91].

Interpretation as an Electron Transfer Rate When considering the meaning of the chemisorption function in the context of electron transfer, it is worthwhile to recall that standard works [53, 58] define the chemisorption function as a function of energy ϵ and not as a function of donor energy ϵ_d. That is, it uses the same energy scale as the DOS. The donor energy ϵ_d is a fixed parameter of the adsorbate, which shifts upon adsorption. Our WDOS can thus without trouble be seen as a function of energy ϵ, at a fixed value of the donor energy ϵ_d. The WDOS is not to be seen as a function of donor energy ϵ_d but rather of energy generally, E or ϵ.

Thereby the interpretation of the WDOS as a resonant ET rate is only strictly valid at the donor energy ϵ_d present in the (effective) couplings. The effective couplings in our chemisorption function have been evaluated in the Gram-Schmidt orthogonalization scheme

for a specific donor state of energy ϵ_d. Formally, therefore, the couplings are now functions of the other variables: $H^{eff}_{ad,\mathbf{k}} = H^{eff}_{ad,\mathbf{k}}(H_{ad,\mathbf{k}}, S_{ad,\mathbf{k}}, \epsilon_{d,\mathbf{k}})$.

At the donor resonance energy, the WDOS may be interpreted as an ET rate as follows:

$$\Gamma_{d\to a} = \frac{2}{\hbar}\Delta(\epsilon_d) \tag{3.41}$$

This is consistent with a (pertubative) Golden Rule [113] model of a resonant electron transfer process at the energy ϵ_d . It is nevertheless possible to use the WDOS as an approximate ET rate at energies other than ϵ_d, using the effective couplings determined with ϵ_d. The quality of this approximation is determined by the overlap S_{ad}, as seen in Equation (3.36).

Experiments have reported an energy dependence in the measured electron transfer lifetimes. We will use the approximation above and interpret the chemisorption function as an ET rate near the predicted resonance, in order to compare to experimental trends. This provides a validation of the slope of the chemisorption function near resonance. To assess and validate the behavior of the chemisorption function (and couplings) over the remainder of the energy scale, such as below the Fermi level, where no experimental data exists, we will use qualitative phase cancellation arguments from scanning-tunneling microscopy [47, 49].

3.3 Interpretive Tools

The chemisorption function contains rich information on the local interaction between the adsorbate and surface. The interpretation of the chemisorption function proceeds in a manner similar to the density of states, i.e. by studying contributions from the angular momentum channels of the surface. Additionally, the couplings themselves can be analyzed, identifying dominant states and correlating the character of acceptor states with the coupling strength. Phase effects are important in the interpretation of the chemisorption function over the energy scale.

3.3.1 Mulliken Analysis

To determine the angular-momentum decomposition of the chemisorption function, and to measure the character of the donor and acceptor states, we use the Mulliken population of states on the basis functions [8, 89]. Mulliken population analysis is known to be dependent on the basis set, but provides important qualitative insights.

Consider the diabatic (or adiabatic) state $|\psi_a\rangle = \Sigma_i^N C_{a,i}\,|\phi_i\rangle$, expanded with coefficients $\mathbf{C}_a$ in the non-orthogonal basis set {N} of the adsorbed system. For brevity, **k**-dependence is omitted in the following equations but is implicitly assumed. The overlap of the basis functions ϕ_i is $S_{ij} = \langle\phi_i|\phi_j\rangle \neq 0$ and generally has a complex value: S_{ij}=$\overline{S_{ji}}$. The state is

normalized with respect to the overlap matrix of the basis set:

$$\begin{aligned}\langle\psi_a|\psi_a\rangle &= \mathbf{C}_a^\dagger \mathbf{S}\mathbf{C}_a \\ &= \sum_{i,j}^{N} \overline{C_{a,i}} S_{ij} C_{a,j} \\ &= \sum_{i}^{N} |C_{a,i}|^2 + \sum_{i\neq j}^{N} \overline{C_{a,i}} S_{ij} C_{a,j} \\ &= 1.\end{aligned} \tag{3.42}$$

The basis functions are assumed to be normalized. The first term in Equation 3.42 corresponds to the net population: the probability density of the state on the basis functions. The second term is the overlap population: the probability density of the state between pairs of basis functions, which is shared.

We may similarly define a normalization with respect to a subset $\{\mu\}$ of the full basis set {N}. The subset $\{\mu\}$ may be composed of atomic orbitals of a specific angular momentum, $\mu \in \{s, p, d, ...\}$, or be functions localized on specific atoms, e.g. in the surface and bulk of the slab: $\mu \in$ {bulk, surf}.

The Mulliken population of the state on (and among) these basis function is:

$$\begin{aligned}M_{a,\mu} &= \left(\mathbf{C}_a^\dagger\right)_\mu (\mathbf{S}\mathbf{C}_a)_\mu \\ &= \sum_{i\in\{\mu\}} \overline{C_{a,i}} \, (\mathbf{S}\mathbf{C}_a)_i \\ &= \sum_{i\in\{\mu\}} \sum_{j}^{N} \overline{C_{a,i}} S_{ij} C_{a,j} \\ &= \sum_{i\in\{\mu\}} |C_{a,i}|^2 + \sum_{i\in\{\mu\}} \sum_{j\neq i}^{N} \overline{C_{a,i}} S_{ij} C_{a,j}.\end{aligned} \tag{3.43}$$

For the trivial case where the basis subset $\{\mu\}$ is equivalent to the full basis set {N}, the expression M_μ reduces to the normalization condition of Equation (3.42). Note that in the Brillouin zone $M_{a,\mu}$ is in general complex-valued, even if the full normalization yields the real value of 1:

$$\sum_{\{\mu\}} M_{a,\mu} = \langle\psi_a|\psi_a\rangle = 1 \tag{3.44}$$

The sum is taken over non-intersecting subsets $\{\mu\}$ of the full basis $\{N\}$. The overlap populations in Equation (3.43) are complex-valued, while the net populations have real value.

As a result, any decomposition scheme based on this analysis, such as a projected-DOS, would also be complex valued while the DOS remains real-valued. For interpretability, we therefore use the absolute value $|M_{a,\mu}|$ to represent the character of a state. As a result, the components may not add up perfectly to 1, but only approximatively so:

$$\sum_{\{\mu\}} |M_{a,\mu}| \simeq \langle \psi_a | \psi_a \rangle = 1 \tag{3.45}$$

The approximation is suitable for the case where Mulliken populations are dominated by the net population, with relatively small overlap populations. In practice, it is found in this work to be well behaved below the vacuum energy level, where overlaps are small.

In this way, the angular-momentum-projected DOS (PDOS) is calculated below. Also, the character of e.g. the Argon donor wavepacket can be described by **k**–averaged Mulliken weights ($|M_{d,s}|$, $|M_{d,p}|$), which sum up approximately to 1.

3.3.2 Angular-Momentum Decomposition

The chemisorption function is closely related to the conventional density of states and can be analyzed similarly [89]. The density of states is defined as an integral over the Brillouin zone, achieved in practice by sampling the points of the irreducible Brillouin zone using Monkhorst Pack grid and weights [91, 92]. For smoothness, a normalized distribution $g_\sigma(\epsilon - \epsilon_a)$ (in this work, a Lorentzian) is applied:

$$\mathrm{DOS}(\epsilon) = \sum_{\mathbf{k}}^{\mathrm{IBZ}} w_{\mathbf{k}} \sum_{a}^{N_{acc.}} g_\sigma(\epsilon - \epsilon_{a,\mathbf{k}}), \tag{3.46}$$

The DOS under this definition has the units of [states/eV/cell], and is thus dependent on the number of atoms in the cell. The sum is taken, in our case, over the N_{acc} acceptor states of the substrate. The angular-momentum-projected DOS of a system may be defined using the Mulliken population weights above, which describe the normalized character of each state. Each state of the system $|\psi_{a,\mathbf{k}}\rangle$ may be assigned the weights $M_{a,s}, M_{a,p}, M_{a,d}$, etc., using Equation (3.43) which are now **k**-dependent:

$$\mathrm{PDOS}_\mu(\epsilon) = \sum_{\mathbf{k}}^{\mathrm{IBZ}} w_{\mathbf{k}} \sum_{a}^{N_{acc.}} |M_{a,\mu,\mathbf{k}}| g_\sigma(\epsilon - \epsilon_{a,\mathbf{k}}), \qquad \mu \in \{s, p, d \ldots\} \tag{3.47}$$

The angular-momentum-projected DOS (we call this the PDOS) describes the *spd*–hybridized character of the states over the energy scale, again with units [states/eV/-cell]. The weights $|M_{a,\mu}|$ should ideally sum up to 1 for each acceptor state $|\psi_{a,\mathbf{k}}\rangle$, and the decomposition should sum up to the original DOS:

$$\mathrm{DOS}(\epsilon) \simeq \sum_{\{\mu\}} \mathrm{PDOS}_\mu(\epsilon) \tag{3.48}$$

As described above, this is only approximately true, and PDOS is generally used for qualitative interpretation[89].

Using the same notation, the chemisorption function of Equation 3.40 takes the form

$$\Delta(\epsilon) = \pi \sum_{\mathbf{k}}^{\mathrm{IBZ}} w_{\mathbf{k}} \sum_{a}^{N_{acc.}} |H_{ad,\mathbf{k}}|^2 g_\sigma(\epsilon - \epsilon_{a,\mathbf{k}}). \tag{3.49}$$

and has the units of [eV/cell]. The sum runs over the diabatic states of the surface (acceptor) subsystem. The chemisorption function gives the energy broadening of the adsorbate state $|\psi_d\rangle$, and is shown to be independent of cell size in the low coverage limit, thanks to the local nature of the couplings.

To describe the contributions of each angular-momentum channel to the broadening of the donor, it is possible to define a decomposition of the chemisorption function in the same way as the PDOS, using the Mulliken characters of each surface state:

$$\Delta_\mu(\epsilon) = \pi \sum_{\mathbf{k}}^{\mathrm{IBZ}} w_{\mathbf{k}} \sum_{a}^{N_{acc.}} |M_{a,\mu,\mathbf{k}}||H_{ad,\mathbf{k}}|^2 g_\sigma(\epsilon - \epsilon_{a,\mathbf{k}}), \qquad \mu \in \{s, p, d \ldots\}, \tag{3.50}$$

with

$$\Delta(\epsilon) \simeq \sum_{\{\mu\}} \Delta_\mu(\epsilon) \tag{3.51}$$

Expression (3.50), which we term the angular-momentum-projected WDOS or pWDOS, is perhaps best viewed as a coupling-weighted PDOS. It contains information about the hybridized character of the states, weighted by their coupling. The chemisorption function is a weighted DOS, which consists of the DOS component and the couplings. The pWDOS contains information about the character decomposition of the DOS component, but importantly, not about the decomposition of the couplings themselves. Thus, the Equation (3.50) must be carefully interpreted. The relationship between coupling strength H_{ad} and the character of the acceptor state is highly nontivial due to symmetry and phase effects. Therefore, the relationship between the PDOS and pWDOS will also be nontrivial.

We note that our PDOS is based on the projection of the $N_{acc.}$ *diabatic* surface states $\psi_{a,\mathbf{k}}$ upon the atomic orbital basis functions, and we employ it for a decomposition of the slab angular momentum channels. Our PDOS uses the Mulliken populations as weights. This is suitable for a decomposition of the diabatic acceptor DOS in terms of subsets of the basis.

It is possible, however, to define the PDOS in the *adiabatic* system and with respect to other projection functions, such as the frontier molecular orbital of an adsorbate. In this way, the character of the delocalized, adiabatic DOS can be analyzed and the energetic broadening and hybridization of the molecular state understood:[53, 58]

$$\mathrm{PDOS}_{ads.}(\epsilon) = \sum_{\mathbf{k}}^{\mathrm{IBZ}} w_{\mathbf{k}} \sum_{i}^{N_{\text{Kohn-Sham}}} |\langle \psi_i | \psi_{\text{ads.}} \rangle|^2 g_\sigma(\epsilon - \epsilon_{i,\mathbf{k}}). \tag{3.52}$$

Here, the sum is over the adiabatic Kohn-Sham spectrum. Indeed, it is this *adiabatic* PDOS of the adsorbate which the Newns-Anderson model, in Equation 2.28, predicts in terms of the *diabatic* couplings.

4 Results

4.1 Electronic Coupling in Molecular Dimers

We demonstrate here the calculation of electronic couplings in molecular dimers. Parts of this section have been reused with permission from Reference [1], Copyright 2020 American Chemical Society.

4.1.1 Computational Details

Geometries for all systems were taken from reference structures of the Hab11 database [74] and kept without relaxation. Dimers are provided at four different separations from 3.5 to 5Å. The exponential decay constant β of the coupling values was calculated by a least-squares fit to $\log(|H_{ad}|)$ over these 4 separations. Self-consistent KS Hamiltonians were calculated by and exported from the all-electron DFT package FHI-aims [89] using the PBE [88], B3LYP [114], PBE0 [115, 116] and LC-ωPBE [117, 118] exchange-correlation functionals. Additionally, we modify PBE0 to contain 50% exact exchange and label this as PBE50 as in previous work [119].

Basis sets used are the Numeric Atom-Centered Orbital (NAO) [90] functions with default Tight integration grid and tier settings, as well as the NAO-VCC-NZ and Dunning correlation-consistent cc-pVNZ basis sets [109] provided with FHI-aims. The NAO Light extended basis is also used. This, denoted Light+, is a default Light "tier 1" basis with light integration settings plus selected additional 2nd tier functions added for Hydrogen and Carbon. This has been used alongside the default Tight basis throughout to facitilitate comparison to earlier FODFT calculations [70, 120]. For comparison, the light tier-1 NAO basis has been found to yield total energies comparable to the split-valence triple-ζ plus polarization Dunning gaussian-type basis pVTZ [121]. Generally, the NAO basis sets used are of greater spatial extent, containing functions with lower decay exponents than the Dunning cc-pVNZ functions and hence offer a useful addition.

All POD, POD flavors and energy-splitting results are based on converged, self-consistent dimer Kohn-Sham Hamiltonians. Dimer systems are neutral (not charged as in some work [71]). In order to facilitate a closer comparison, we also perform FODFT calculations using converged dimer Hamiltonians. Original work on FODFT [69] was based on converged

dimers while more recent FODFT [70] and DIPRO [99] implementations use alternatively an unconverged dimer density, formed from the superposition of fragment densities. For clarity, we label our converged-dimer FODFT results as cFODFT.

All POD flavors and cFODFT were implemented as post-processing routines using NumPy [122] and SciPy [123] libraries in python version 2.7.9.

Error statistics for $y = H_{ad}$ or β are analyzed with the mean signed and unsigned errors: MSE=$\frac{1}{N}\sum_i y_i - y_{\mathrm{ref},i}$ MUE=$\frac{1}{N}\sum_i |y_i - y_{\mathrm{ref},i}|$, MAXUE=max$\{|y_i - y_{\mathrm{ref},i}|\}$, and mean relative signed and unsigned errors MRSE=$\frac{1}{N}\sum_i \frac{y_i - y_{\mathrm{ref},i}}{y_{\mathrm{ref},i}}$, MRUE=,$\frac{1}{N}\sum_i \frac{|y_i - y_{\mathrm{ref},i}|}{y_{\mathrm{ref},i}}$. In accordance with earlier studies, [70] the signs of the couplings H_{ad} are neglected to avoid over-interpretation of the results in view of the essentially random phases of the diabatic wavefunctions.

The range-corrected hybrid functional LC-ωPBE was parametrized using a non-empirical ionization-potential (IP) tuning method. Here, the range-separation parameter ω is tuned for each monomer such that the ΔSCF ionization potential (calculated as the difference in energy between neutral and cationic monomers) matches the molecular HOMO energy for individual neutral monomers [117, 118].

4.1.2 Results and Discussion

Benzene Dimer

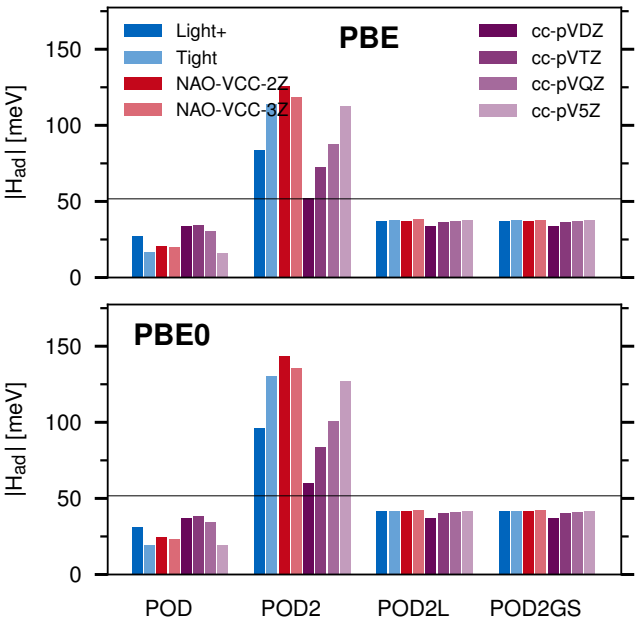

Figure 4.1: Benzene dimer couplings at 5Å separation for the different POD flavors and various basis sets, for the PBE functional (upper pannel) and the PBE0 functional (lower panel). The reference value from the Hab11 database is shown by the horizontal, black line. Figure reused with permission from Reference [1]. Copyright 2020 American Chemical Society.

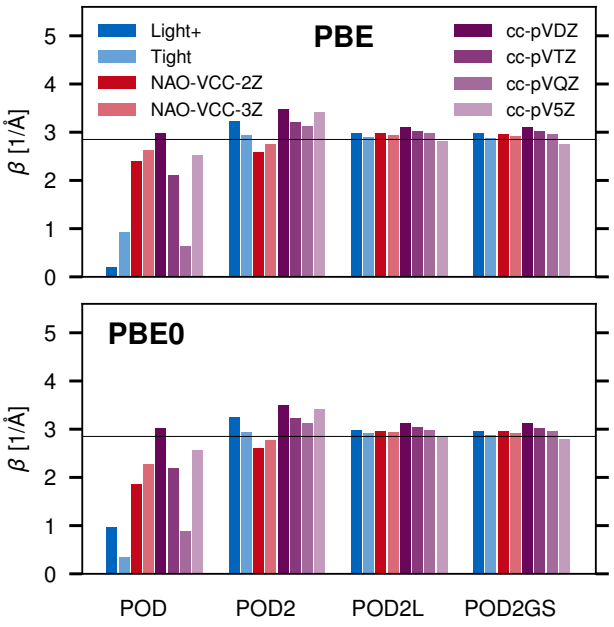

Figure 4.2: Decay constants β for the Benzene dimer for the different POD flavors and various basis sets, for the PBE functional (upper pannel) and the PBE0 functional (lower panel). The reference value from the Hab11 database is shown by the horizontal, black line. Figure reused with permission from Reference [1]. Copyright 2020 American Chemical Society.

In order to highlight the differences between the different POD flavors, we continue with a quantitative analysis of the Benzene dimer showcase. Figure 4.1 depicts the donor-acceptor hole coupling H_{ad} at a single dimer geometry of 5Å separation. Owing to the non-orthogonality of the resulting diabatic states, POD2 clearly overestimates the coupling. Valeev [98] notes that couplings H_{ad} of non-orthogonal diabats, such as those in eq. (3.31), can differ from the effective couplings H_{ad}^{eff} by as much as a factor of 2. Indeed this is the case when comparing POD2 with the effective POD2GS and POD2L couplings. POD2 thus cannot be considered a useful method for production calculations, but is included here nevertheless for comparison.

Figure 4.1 also shows for both tested functionals a significant, non-trivial variation in the POD couplings over the different basis sets. H_{ad} varies more strongly with the basis than it does between the two functionals. Light+, Tight and the NAO-VCC-NZ basis sets contain the most diffuse functions and hence show the greatest error in POD. The most compact basis set, cc-pVDZ, shows indeed quite small errors. Further Dunning sets up to cc-pV5Z show a progressively lower coupling element for POD and PBE, with similarly unstable behavior under the hybrid PBE0. Not only does the accuracy decrease, but it appears the coupling values diverge as the basis grows more diffuse. As the mixing in the basis set becomes

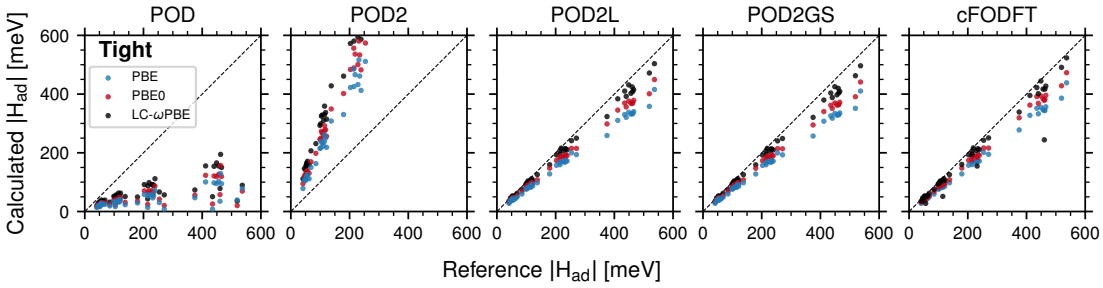

Figure 4.3: Performance of the various POD flavors vs. the Hab11 benchmark for three different functionals. All calculations are performed at with the FHI-aims Tight basis. cFODFT results are shown in the rightmost panel for comparison. Figure reused with permission from Reference [1]. Copyright 2020 American Chemical Society.

more severe, diabats delocalize more, and this causes a systematic reduction in coupling strength.

Considering on the other hand the behavior of POD2L and POD2GS, both are much more stable over the different basis sets than POD and moreover virtually indistinguishable for this system. Also, in both cases the choice of functional now has more influence on H_{ad} than the basis set, with the PBE0 functional containing 25% exact exchange yielding slighly stronger couplings.

Figure 4.2 depicts the distance decay behavior of the couplings, as represented by the decay constant β. Physically, wavefunction couplings, like overlap, are expected to decay exponentially due to the exponential shape of their tails:

$$H_{ad} = H_{ad}^{0} e^{-\beta d/2} \tag{4.1}$$

where d is the fragment separation. This will in practice be determined by the basis functions used, the functional, and the employed flavor of the POD scheme. As seen in Figure 3.3, POD at small separations performs poorly for the more diffuse Dunning basis sets cc-pVQZ and cc-pV5Z. Mixing of the basis sets is severe, resulting in significant delocalization of the diabats, as shown in the SI Tables SII-SIV of Reference [1].

This results in large errors for β, as shown in Figure 4.2. The diffuse NAO basis sets severely underestimate β for POD. The delocalized wavefunction tails of the POD diabats results in a slower decay of coupling. The cc-pVDZ result of POD, in contrast, is good for both functionals PBE and PBE0 as it contains minimal mixing. POD2L and POD2GS likewise both capture proper exponential behavior. The functional appears to make no large difference in the decay exponent in Figure 4.2.

Hab11 test set

The analysis of the Benzene showcase reveals that POD works consistently well only with the most compact cc-pVDZ basis. The accuracy of POD2L and POD2GS is similar, but instead uniform over all the basis sets. We now proceed to assess, if this holds more

generally, and therefore analyze the performance of the POD flavors for the complete Hab11 test set of molecular dimers [74]. In this most accurate reference set, all H_{ad} values are calculated at the MRCI+Q level of theory by applying the energy splitting principle to the adiabatic dimer states [74].

Figure 4.3 summarizes the corresponding performance comparison, compiling the calculated H_{ad} couplings for POD and its various flavors, as well as also comparing to the cFODFT method. The POD2-based flavors POD2L and POD2GS clearly outperform the original POD method for all tested functionals and deliver an accuracy that is only slightly worse than the established cFODFT method for almost the entire benchmark set. The original POD clearly yields unphysical results for the employed extensive FHI-AIMS Tight basis set, reflecting the diabat mixing already discussed for the Benzene showcase. The few problematic outliers visible in the cFODFT results are from the acetylene dimer and are due to the symmetry of the molecule, which allows for arbitrary orientations of the fragment HOMOs around the molecular axis. The acetylene dimer is for this reason excluded from cFODFT error statistics below.

The similar performance of the POD2-derived flavors to the cFODFT method is generally expected as the POD2-based diabats should behave similarly to the basis of monomer fragments in cFODFT for the weakly-interacting systems in the Hab11 test set. We will show below that the overall slightly weaker couplings obtained for the POD2L and POD2GS flavors result from polarization effects present in the POD2 diabatic wavefunctions. Unfortunately, with the functionals tested, capturing this additional physics worsens the agreement with the Hab11 reference values. The slightly weaker couplings of POD2L compared to cFODFT are also shown in SI figure S3 of Reference [1] for the LC-ωPBE functional. Both cFODFT and the POD2-derived flavors yield stronger couplings at the hybrid PBE0 level with 25 % exact exchange than at the semi-local PBE level. This decreases the cFODFT MRSE from -25% (PBE) to -17% (PBE0), while both the POD2L and POD2GS MRSEs decrease from -26%(PBE) to -18%(PBE0), respectively. The range-corrected functional LC-ωPBE, which contains 100% exact exchange in the long-range limit, allows for even higher accuracy, with MRSE of -7% for cFODFT and -8% for both POD2L and POD2GS. Overall, the quantitative coupling values respond thus sensitively to the amount of exact exchange, and this interferes with the wavefunction polarization afforded in the POD2 flavors. In the following, we will analyze this interplay in more detail, but will first further confirm the proper basis set convergence achieved in the POD2 flavors for the entire Hab11 test set.

Basis set convergence

Regarding stability with respect to basis sets, POD is not alone in its vulnerability. Analogous to the problems of diabatization, molecular charge analysis or the theory of atoms in molecules also suffers from a nonunique definition of atomic charges. Mulliken and Löwdin charge analysis schemes exhibit similar instability with variations in the basis set, and recent improved schemes seek to remove these dependencies [124].

Figure 4.4 compiles the MRUE over all calculated couplings in the Hab11 test set for dif-

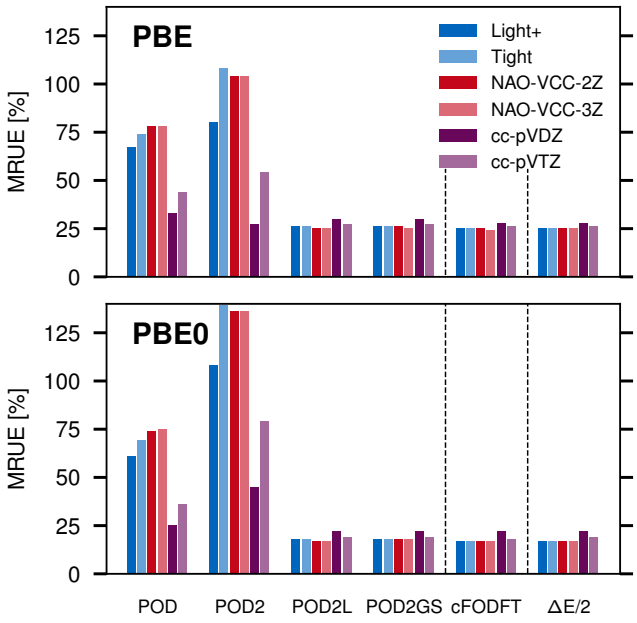

Figure 4.4: Mean relative unsigned error (MRUE) of H_{ad} couplings for the Hab11 test set calculated with the POD flavors and various basis sets (see text). Additionally shown are corresponding results for the cFODFT and the energy-splitting $\Delta E/2$ methods. Note the unsystematic behavior of POD and POD2, whereas all other approaches exhibit a proper basis set convergence. Figure reused with permission from Reference [1]. Copyright 2020 American Chemical Society.

ferent basis sets and the PBE and PBE0 functionals. For reference, corresponding results for the cFODFT and energy-splitting methods are also included. In full analogy to the behavior observed above for Benzene, there is a clearly improved basis-set stability in the case of POD2L and POD2GS. There is also a strikingly good agreement between these and the cFODFT and energy-splitting methods for both functionals. As discussed above, this is not unexpected for the symmetric, well-separated dimers contained in the Hab11 test set. The erratic behavior observed for POD and POD2 is again inconsistent with all other methods and precludes the use of these methods for production calculations. The analogue behavior obtained for both hybrid PBE0 and semi-local PBE, suggests these findings to be independent of the employed DFT functional.

Corresponding errors in the decay parameter β are compiled in Figure 4.5. POD with a cc-pVDZ basis set performs well, with a MRSE of 4% (PBE) and 5% (PBE0). However, this performance is lost for more extensive basis set, e.g. a severe underestimation of -47% (PBE) results for the comprehensive Tight basis set. The POD2-based methods are much improved and show less variation with respect to the basis set. POD2L has an MRSE in the range of -0.8 to 8% for PBE and 0.2 to 8.8% for PBE0. Overall, these errors are smaller than the MRSE obtained for the couplings, which are in the range of -30 to -25% for PBE and -22 to -17% for PBE0, shown in SI Figure S7 of Reference [1]. The cc-pVDZ β parameters are

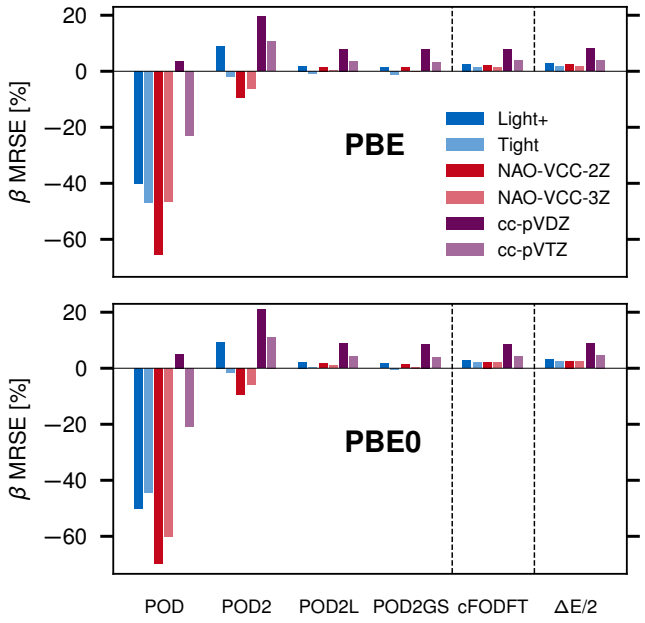

Figure 4.5: Mean relative signed error (MRSE) of the decay parameter β for the Hab11 test set calculated with POD and POD flavors and various basis sets (see text). Additionally shown are corresponding results for the cFODFT and the energy-splitting $\Delta E/2$ methods. Figure reused with permission from Reference [1]. Copyright 2020 American Chemical Society.

noticeably higher than those for the other basis sets in Figure 4.5 and there is generally a slightly higher MRSE for PBE0 compared to PBE. We can explain this in terms of wavefunction tails. The more diffuse NAO basis sets of FHI-aims (Light+, Tight, NAO-VCC-NZ) offer contributions supporting longer exponential tails. Thus, as with Benzene, decay parameters are lower for the NAO basis sets and higher for the more compact cc-pVDZ. The slightly larger decay parameters for PBE0 suggest likewise more compact diabatic wavefunctions with shorter exponential tails, which is consistent with the known properties [125, 126] of exact exchange. Including Hartree-Fock exchange partially corrects the self-repulsion error present in semi-local functionals. The diabats derived from adiabatic states in the POD and cFODFT methods are likewise expected to be more localized, with shorter tails. The specific influence of the functional on the couplings will be further discussed in detail in section 4.1.2 below.

Analysis of wavefunction isosurfaces (in Tables SII-SIV of Reference [1]) shows that in general the diabatic wavefunctions delocalize with more diffuse basis sets, resulting in higher overlap, stronger coupling and lower decay parameters for POD2-based methods. POD β values, in contrast, are severely underestimated due to the strong delocalization of the diabats.

Physically, one would expect a need for diffuse functions in the basis set to properly describe

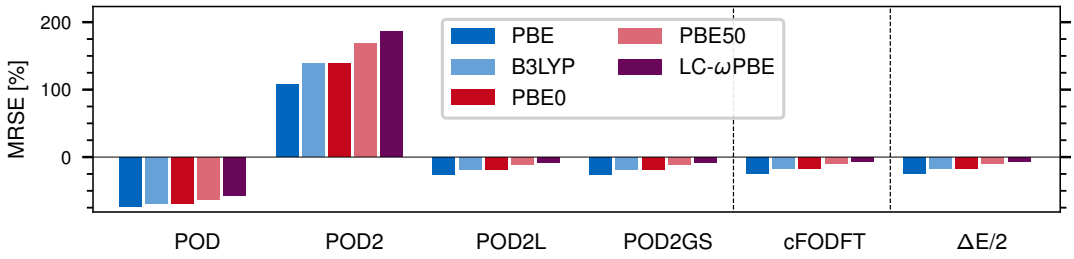

Figure 4.6: Mean relative signed error (MRSE) of H_{ad} couplings for the Hab11 test set calculated with POD, POD flavors, cFODFT and the energy-splitting method $\Delta E/2$ and various exchange-correlation functionals. The functionals are listed in order of increasing amounts of exact exchange. The Tight basis set is used throughout. Figure reused with permission from Reference [1]. Copyright 2020 American Chemical Society.

charge transfer systems, as these improve the description of the donor and acceptor frontier orbitals. Particularly for electron transfer—which would use an equivalent model based on diabatic LUMOs instead of HOMOs [75]—the importance of diffuse functions can not be underestimated. It is desirable, therefore, to have a method to calculate couplings which shows a more predictable behavior upon addition of diffuse functions to the basis. POD2L and POD2GS vastly improve over POD in this regard.

Exact Exchange

The improved basis-set stability of the POD2-based methods allows for a more precise understanding of the role of the exchange-correlation functional in determining electronic couplings. With a reasonably converged basis set, remaining errors in the calculated coupling values can be ascribed to the description of the electronic structure.

Figure 4.6 provides a comparison of the various diabatization methods with respect to different exchange-correlation functionals using the converged Tight basis set. The POD2L and POD2GS methods are again consistent with cFODFT and energy-splitting methods for all the functionals used. Importantly, errors decrease systematically with the increased fraction of exact exchange present in the functional. MRSEs for POD2L range from -26% for the semi-local PBE to -8% for the LC-ωPBE functional containing the highest amount of exact exchange. In contrast, the error of POD remains large and POD2 errors even increase as the functional tier is improved.

Figure 4.7 shows the same comparison for the decay parameters. Generally, we find small relative errors (MRSE in the range of -2 to +3%) and small unsigned errors (MRUE within the range of 2 to 4%) for the methods of interest (POD2L and to the right). There is a mix of under- and overestimation in MRSE, which, however may also include some error cancellation.

The addition of exact exchange has a less strong and less systematic effect on decay parameters in the POD2-based methods than it has for the coupling strengths. The cFODFT and energy-splitting method behave similar to each other, with MRSE of β increasing slightly

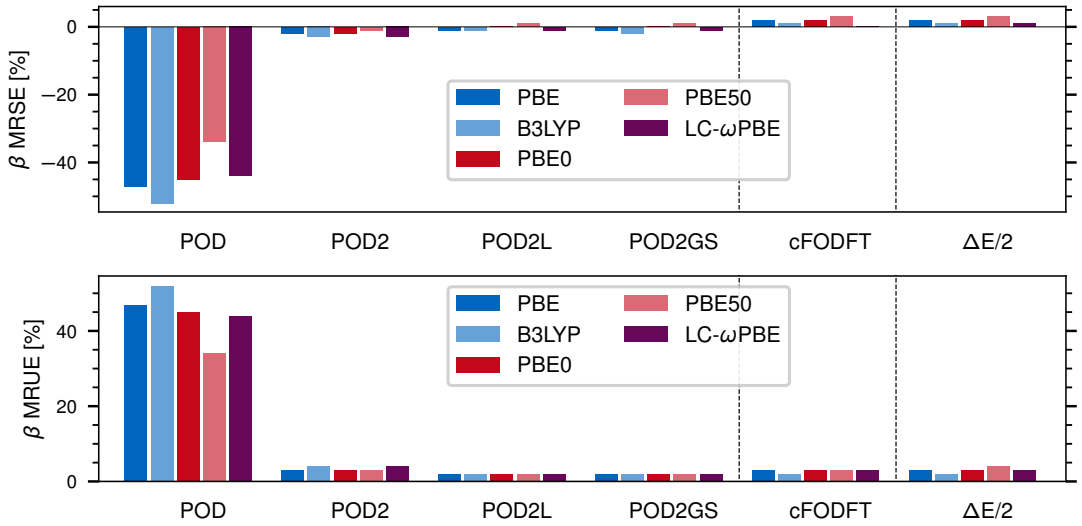

Figure 4.7: Mean relative signed error (MRSE) and mean relative unsigned error (MRUE) of the decay parameter β for the Hab11 test set calculated with POD, POD flavors, cFODFT and the energy-splitting method $\Delta E/2$ and various exchange-correlation functionals. The functionals are listed in order of increasing amounts of exact exchange. A Tight basis set is used throughout. Figure reused with permission from Reference [1]. Copyright 2020 American Chemical Society.

over B3LYP-PBE50, but lower again for LC-ωPBE. cFODFT and energy-splitting β MRUE are also slightly higher than that of POD2-methods for all functionals.

A different dependence of decay parameter β on exact exchange for various methods is anticipated due to their differing construction. As the energy-splitting method is not dependent on the diabatic wavefunctions but rather on adiabatic energy levels, it contains no sensitivity to wavefunction tails. The consistency of MRSE results between cFODFT and energy splitting would here thus suggest that exchange influences the decay parameter through other means than the fragment wavefunction tails. This is explored further below.

Overall, LC-ωPBE yields the most accurate coupling strengths and decay parameters with the POD2-based methods. In contrast, PBE, while underestimating coupling strengths, performs as well as LC-ωPBE for the decay constants. The variation of β MRSEs with basis sets (up to 9% overestimation with cc-pVDZ and PBE0) in Figure 4.5 is greater than with the various functionals (up to only +2% overestimation with Tight settings) in Figure 4.7. This would indicate that basis sets dominate over exact exchange in determining wavefunction tail character and hence β. This is confirmed in SI Tables SII-SIV of Reference [1], where indeed the basis sets make a more qualitative difference in determining the spatial character of diabats than the functionals. However, both functionals and basis sets contribute significantly to the coupling strengths.

The above results raise the question of how exact exchange influences the couplings, and whether this occurs through the (small) wavefunction tails or through the accuracy of the Hamiltonian itself ($H_{ad} = \langle\psi_a|\hat{H}|\psi_d\rangle$). Considering e.g. POD2L, we see from eq. (3.31) that

the effective couplings H_{ad}^{eff}—which we identify with the H_{ad} of other methods—depend on more than just the overlap of the POD2 diabats. The non-effective coupling H_{ad} as well as on-site energies $\epsilon_{\{a,d\}}$ originate from the POD2 block-diagonalized Hamiltonian, which is a representation of the adiabatic electronic Hamiltonian in the non-orthogonal POD2 quasi-diabatic basis. $\widetilde{\mathbf{H}}^{eff}$ of eq. (3.24) is the pair-wise representation of the adiabatic Hamiltonian in the orthogonalized diabatic basis of POD2L. Effective couplings H_{ad}^{eff} therefore arise from multiple basis transformations of the original Hamiltonian. It is the representation of this Hamiltonian – the interactions between states – in the POD2L diabatic basis which yields the accurate and well-behaved couplings H_{ad}^{eff}. The POD2L diabatic basis is of a higher quality for this transformation. The more compact orbital tails of the hybrid functionals may indeed be rather spectators when it comes to the magnitude of couplings, while taking a more important role in determining decay behavior.

This point can be tested. We demonstrate in Figure S1 that in cFODFT, the increase in coupling strengths with hybrid functionals is due not to wavefunction tails but to the operator. cFODFT couplings evaluated with a PBE0 dimer but using the PBE fragment orbitals show the same stronger couplings as with the PBE0 fragments. Similarly, cFODFT with a PBE dimer and PBE0 fragments has nearly the same weaker couplings as with the PBE fragments. This indicates a certain robustness of the electronic couplings against the choice of diabats. The more important factor is thus the choice of functional used to calculate the dimer Hamiltonian. This point has also been observed for FODFT [70]. As the cFODFT results are consistent with energy splitting and the POD2-based couplings, we conclude that the role of diabat tails is likewise minor in determining POD2-based coupling strengths and the operator dominates here as well.

Furthermore, throughout this work, we find similar coupling values achieved with POD2L and POD2GS, despite a difference in the character of the diabats for these two flavors (cf. Table 3.2). In POD2GS, the donor orbital character of POD2 is preserved and the acceptor distorted under the orthogonalization. In contrast, POD2L symmetrically distorts both acceptor and donor orbitals. The similarity of the two flavors with respect to the couplings thus demonstrates again the importance of the dimer Hamiltonian operator over diabatic wavefunction characters for the present systems.

We note here that our results are qualitatively in agreement with previous studies using POD. We summarize some recent results in the Table S1 of Reference [1] and discuss these findings there in detail.

A number of previous studies have also employed long-range corrected hybrid functionals such as LC-ωPBE [117, 118, 127–130] in the calculation of electronic couplings [101, 103] and likewise achieved higher accuracy over global hybrids. By incorporating 100% Hartree-Fock exact-exchange in the long-range component of the exchange functional, the correct asymptotic behavior of the non-local exchange potential can be restored, resulting in more accurate wavefunction and density tail regions. This correction to the electronic structure is advantageous for electronic couplings, as the dimers considered here are well-separated and the couplings depend considerably on the quality of the density and the Hamiltonian

operator as discussed above. Indeed, LC-ωPBE is found also in this work to outperform conventional hybrids PBE0 and B3LYP in electronic couplings based on the energy-splitting principle, as well as with the POD2-based flavors.

Polarization

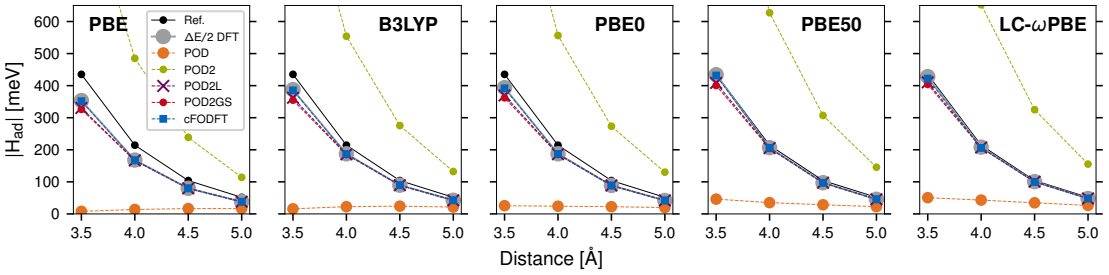

Figure 4.8: Comparison of Benzene dimer couplings for different functionals and methods. cFODFT, energy-splitting $\Delta E/2$ and POD2L results are nearly the same throughout. Improved accuracy for increasing fraction of exact exchange is observed, culminating with LC-ωPBE. Figure reused with permission from Reference [1]. Copyright 2020 American Chemical Society.

The explicit comparison to cFODFT and energy splitting results provides insight into the role of polarization within the dimer and how it affects the spatial character of the diabats. Since they are both based on the same dimer Hamiltonian, the only difference between cFODFT and the POD2-flavors is the construction of diabats: cFODFT uses the unpolarized fragments as diabats while the POD2-flavors construct diabats from the polarized dimer Hamiltonian. Figure 4.8 provides this comparison for the Benzene dimer and different functionals, illustrating for this showcase what has generally already been seen in the error analysis over the Hab11 test set. cFODFT and energy splitting couplings are highly similar throughout, while the POD2L and POD2GS couplings are slightly weaker. Polarization and fragment interaction thus reduces the coupling in the considered dimer systems. For the symmetric dispersion systems contained in Hab11 this impact is in fact quite small. This has also been asserted in an earlier Hab11 study with FODFT [70]. The diabatic states largely retain the character of isolated monomers, even upon relaxation of the dimer density as in the case of cFODFT and the POD2 flavors. The situation is expected to be different, however, for e.g. asymmetric or covalently bridged systems, which we will address in future work.

Derivative Couplings

The improved behavior of POD2-methods over POD can also be understood in terms of the formal requirements of a diabatic basis, which are more closely fulfilled by the POD2-derived flavors than by POD. As discussed in the literature, [32] these include the ability of diabats to maintain their character over changes in nuclear coordinates. Clearly, with decreasing separation of fragments, the POD diabats experience increased mixing and delocalization, resulting in underestimated couplings as demonstrated in Figure 3.3. In contrast, the POD2-based diabats better preserve their character. This requirement on a diabatic basis is stated

in terms of vanishing derivative couplings [32, 131]

$$\mathbf{d}_{ad}(\mathbf{R}) \equiv \left\langle \psi_a \middle| \frac{\partial}{\partial \mathbf{R}} \psi_d \right\rangle = 0 \ \ \forall \ \ \mathbf{R,a,d} \quad . \tag{4.2}$$

Such a condition is often only approximatively met by current diabatization methods [32]. We will not undertake a formal demonstration of the improved derivative coupling behavior of the POD2-based schemes. However, we note that the original block-diagonalization scheme, formulated in a configuration-interaction context, derives approximative diabatic states by partitioning the Hamiltonian [36, 132–135] with proper separation of fragment Hilbert spaces. This method was shown to provide optimized diabats with a minimized euclidean norm of the derivative couplings [131]. However, the Kondov POD implementation [24] makes some (unfortunately necessary) departures from this scheme. It adopts a single-particle approximation and partitions a mixed basis. The mixing in Kondov's method is not present in the original scheme and can be seen as contributing to the derivative couplings and resulting in less optimal behavior. We believe this to be yet another way to understand the improved behavior of POD2-based schemes. Clearly, with regards to fragment separation, the POD2 diabats are less susceptible to change than POD, though some mixing must emerge from the required biorthogonalization.

Summary

We offer reformulations of the DFT-based projection-operator diabatization (POD) method which demonstrate stable convergence with respect to basis set diffusivity. The new flavors use a localization-enforced POD variant (POD2) to parametrize a tight-binding model in the spirit of the fragment-orbital (FODFT) and dimer-projection (DIPRO) methods. This expands greatly the utility and reliability of the POD approach, which can now be used at arbitrary levels in the available basis set hierarchies, beyond the known limitations of the original method.

The fact that the new flavors POD2L and POD2GS converge properly with respect to the basis set allows for a systematic assessement of the role of the employed approximate DFT functional. To this end, we find an improved performance in terms of comparison to reference couplings for the Hab11 test set with an increasing ammount of exact exchange, obtaining most accurate couplings for the range-corrected LC-ωPBE functional.

This systematics provides a sound foundation for the application of the efficient POD-approach to other systems for which more accurate diabatic computational approaches are not tractable. This in particular, as in contrast to equally efficient cFODFT or energy splitting methods, the POD2L and POD2GS flavors allow to capture fragment-interaction and polarization. For the weakly coupled, dispersion-bound systems of the studied Hab11 test set, these interactions led only to small decreases of the calculated couplings. We expect them to play a larger role for asymmetric systems like rotated dimers or molecular adsorbates physisorbed on surfaces. The ability to use arbitrarily large basis sets will be of benefit there, as this allows for a more accurate description of properties such as the (variational) total

energy, geometry, density and frontier orbital character, simultaneous with a convergent behavior of the couplings. Additionally, the ability to preferentially preserve the character of a diabat through Gram-Schmidt orthogonalization in POD2GS offers the potential to study asymmetric systems where a symmetric distortion would result in relatively higher distortions of the smaller fragment. These properties are expected to be of particular advantage in adsorbate-surface systems and will be the topic of future work.

Another advantage of POD methods is the ability explore the influence of fragment interactions (e.g. polarization, hybridization) on electronic couplings. Though not strongly present in the Hab11 systems, these effects are relevant for covalently bound i.e. bridged systems where the partitioning into fragments becomes less obvious and less suitable for fragment-based approaches. As pointed out in the original work [24], such systems are particularly sensitive to mixing under the original POD method due to their strongly interacting nature. We believe this category of systems will therefore benefit significantly from the localization schemes proposed here. Additionally, the localization schemes are compatible with multi-state block-diagonalization approaches (donor-bridge-acceptor) which have been proposed by Wang *et al.* [103], but for which fewer high-accuracy benchmarks are available. Exploration of such systems is thus also relegated to future work.

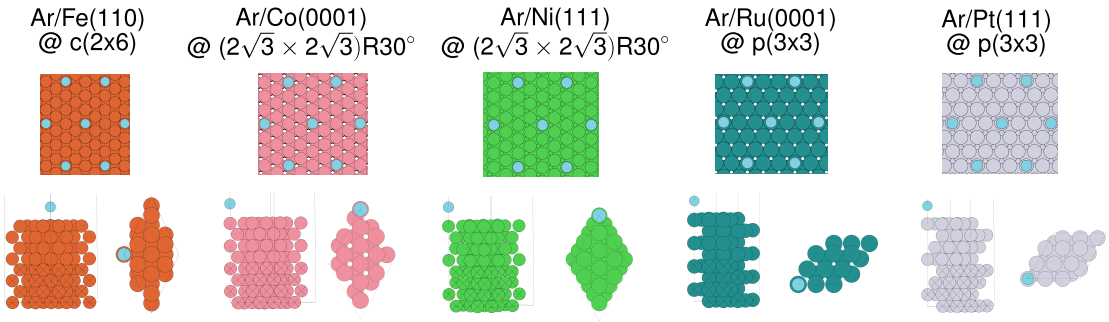

Figure 4.9: The low-coverage Argon/metal slab models used in this work, summarized in Table (4.1).

Table 4.1: Summary of overlayer models.

System	Overlayer	z_{eq}[Å]	Ar-Ar[Å]
Ar/Fe(110) [136]	c(2×6)	3.47	8.004
Ar/Co(0001) [136]	$(2\sqrt{3} \times 2\sqrt{3})$R30°	3.50	8.65
Ar/Ni(111) [136]	$(2\sqrt{3} \times 2\sqrt{3})$R30°	3.41	8.62
Ar/Ru(0001) [79]	p(3x3)	3.63	8.10
Ar/Pt(111) [137]	p(3x3)	3.67	8.32

4.2 Ultrafast Electron Transfer from Core-Excited Argon to Metals

Having demonstrated improved approaches for calculation of electronic coupling in molecular dimers, we next turn to the study of electronic coupling on surfaces. It is desirable to include periodic boundary conditions and consider the full Brillouin zone. The test system will be core-excited Argon on transition metals, shown in Figure 3.5 and 4.1. The photo-populated LUMO state transfers its electron into the surface with an ultrafast lifetime on the order of 3 femtoseconds, which we will seek to predict with the Newns-Anderson chemisorption function. Parts of the following section have been reused with permission from Reference [2] and have been submitted for publication. After they are published, they will be found at The Journal of Chemical Physics.

4.2.1 Computational Details

We apply our chemisorption-function based scheme to low-coverage models of Argon monolayers on five low-index transition metal surfaces. Namely, the magnetic Fe(110), Co(0001) and Ni(111), as well as the non-magnetic Ru(0001) and Pt(111) surfaces. The extended surfaces are described in periodic boundary supercell models, comprising slabs

consisting of eight layers and a vacuum region in excess of 40 Å. Ar is adsorbed at the metal surfaces' top position on one side of the slab such that there is one adsorbate per surface unit-cell. At the employed large surface unit-cells shown in Figure 4.9, this then describes a dilute overlayer with lateral Ar-Ar distances exceeding 8 Å.

The electronic structure of all systems is described at the DFT level, using the Perdew-Burke-Ernzerhof (PBE) functional [88] with Tkatchenko-Scheffler [138] dispersion correction. All calculations are performed with the all-electron DFT package FHI-aims [89, 90]. Tier 1 numeric atomic orbital basis sets are employed for all metals, a Pople 6-311+G** valence triple-ζ basis set from Basis Set Exchange [139] is used for Argon. Note that this split basis approach is necessary because while standard FHI-aims basis sets are able to very accurately represent the electronic structure of the metallic surfaces, they would yield erroneous unoccupied states of the Ar adsorbate. Especially, the crucial LUMO state would have shown a wrong level alignment and orbital geometry. The chosen triple-ζ Ar basis fully remedies this as depicted in Figure 4.10. Real-space quantities are represented on FHI-Aims' tight integration grids while BZ integration is performed on a $(4\times4\times1)$ regular **k**-point grid [91]. The Ar adatom and the topmost four metal layers are fully relaxed until residual forces fall below 5 meV/Å. A half core-hole is then included on Ar to simulate the effect of the core-excited state [15, 140].

For the calculation of the more delicate electronic couplings, a single-point calculation is finally performed. The basis set setting of the topmost metal layer is increased to tier 4. Note that all other metal layers are left at tier 1 and the less crucial integration grids were used at light settings for reasons of computational efficiency. The SCF-converged Hamiltonian and overlap matrices are printed at each point on a $(12 \times 12 \times 1)$ k-grid, and diabatization routines are performed in an external progam based on SciPy [123]. Consistent with the employed low-coverage model and the corresponding excitation of the quasi-isolated initial core electron to arbitrary momenta, the wavepacket of the excited Ar$4s4p_z$ state is assumed to be uniformly distributed in k-space. This approximation is further illustrated in Figure D1.

As demonstrated in Figures A2, A12 and A13 the resulting chemisorption function and the lifetimes derived from it are fully converged with respect to the employed finite k-grid, the Lorentzian smearing σ and the metal basis set. Unfortunately, convergence with respect to the Ar basis set is not that straightforward. Addition of further diffuse functions will increase the basis set superposition. Any such participation of Argon basis functions in describing the slab density will lead to the appearance of a ghost state upon partitioning and diagonalization of the Argon block in the POD2 scheme. This state at 1.6 eV below the Fermi level is already seen in the Γ-point in Figure (4.11c) at the triple-ζ basis set and fortifies for larger Ar basis sets. We find such larger basis sets to also decrease the $4s4p_z$ hybridization of the true donor state. To avoid these problems, we therefore stick to the triple-ζ Ar basis set, which yields a comparable hybridization for the Ar@Fe(110) system as found in earlier work [27, 28, 82, 83]. We discuss the influence of the Argon basis in depth in Appendix A.3. Importantly, while basis set superposition effects are unavoidable in such schemes, the diabatization is found to behave in a stable and continuous manner over the basis sets explored.

We also note that, in direct opposition to earlier results [28], the k-grid integrated chemisorption function converges well with slab depth. As depicted in Figures A6 and A5, already 4 layers of metal atoms show a mostly converged WDOS with no noticeable improvement beyond 8 layers.

Finally, we also examined the convergence of the WDOS with donor coverage. As mentioned above, we target a dilute limit in our work, while in the experiment Ar actually forms a dense monolayer. Yet, at the small fluences of incidence photons only a small fraction of Ar atoms will be excited at any one time. Thus, the excited donor states will essentially be localized and dilute in real space, rather than forming an excited band in the Ar overlayer. As depicted in Figure A9, we find a small variation of computed lifetimes going from the c(2x6) coverage used here to the dilute p(5x5) overlayer, similar to earlier studies [28], which however does not significantly influence resulting trends.

4.2.2 Results and Discussion

Γ-point results

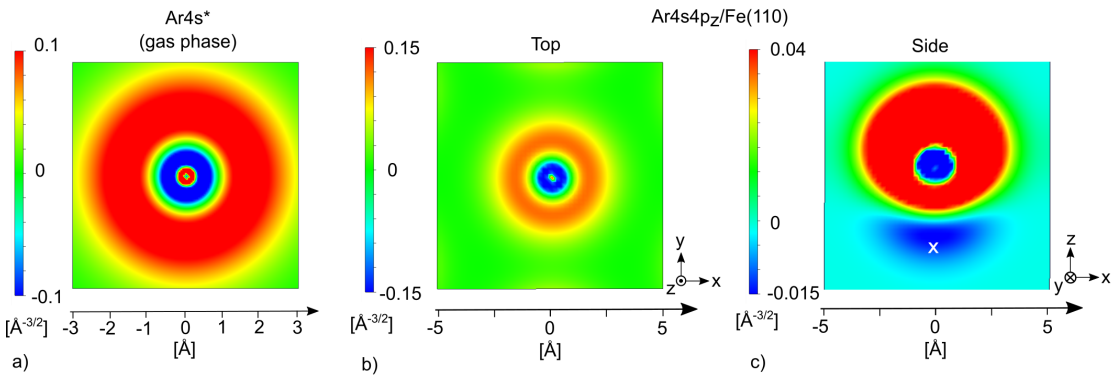

Figure 4.10: a) The Argon 4s* wavefunction in gas phase, with nodal structure resolved. A full core hole is present on the $2p_{3/2}$ level and the promoted electron occupies the 4s. b) Top and c) side views of the Ar$4s4p_z$ $POD2_d$ diabat on the Fe(110) c(2x6) slab with 8 layers, where the Argon contains a half core hole. The position of the Fe surface atom 3.47 Å directly below is marked with a cross. Color scales adjusted for illustration. The 6-311+G** basis set is used.

To illustrate our approach, we first examine the properties of the chemisorption function at the Γ-point, $\Delta_{\mathbf{k}=\Gamma}(\epsilon)$, for the low-coverage $c(2 \times 6)$ Ar/Fe(110) system. These results are summarized in Figures 4.11 and 4.12. Upon projection onto the ($POD2_d$,$frag_a$)GS diabatic basis, the Kohn-Sham Hamiltonian nearly block-diagonalizes, with the acceptor block only approximately diagonal as a result of the GS orthogonalization procedure. The projection yields diabatic energy levels, which are comparable to the levels of the original adiabatic Kohn-Sham spectrum as shown in Figure 4.11c. Most important for the ensuing discussion of adsorbate to surface ET, a donor state appears in the diabatic Argon spectrum at ϵ_d = 3.13 eV above the Fermi level. This is close to the experimental value of 2.97 eV [136] and we note that the half core-hole constraint is crucial to achieve this good alignment. As

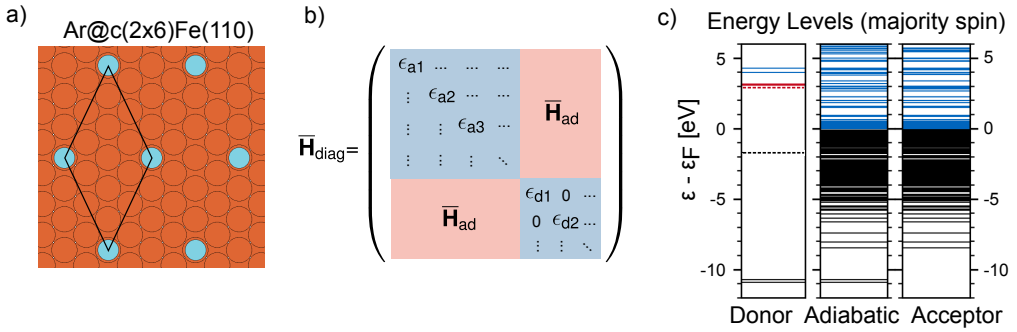

Figure 4.11: Illustration of the diabatization procedure (POD2$_d$,frag$_a$)GS, for the case of the low-coverage Argon model on ferromagnetic Fe(110) shown in a). b) Schematic of the quasi block-diagonal representation of the Kohn-Sham Hamiltonian achieved upon projection onto the (POD2$_d$,frag$_a$)GS diabatic basis. c) Energy spectra of the majority-spin donor and acceptor diabatic blocks compared to the original adiabatic Kohn-Sham spectrum (occupied states in black, unoccupied states in blue). An Ar4*s*-like state (red solid line) emerges close to the experimental resonance (red dashed line) in the diabatic donor spectrum. Additionally, a ghost state resulting from basis set superposition appears at 1.6 eV below the Fermi level (black dashed line). This figure has been reused with permission from Reference [2] and has been submitted for publication. After it is published, it will be found at The Journal of Chemical Physics.

apparent from the real-space visualization in Figure 4.12a this Ar donor state has a hybridized 4*s*4p_z character and thus contains a nodal plane parallel to the surface, consistent with earlier theoretical [82] and experimental [141] work.

Figure 4.12b shows the computed electronic couplings $H_{ad,\mathbf{k}=\Gamma}$ to all acceptor states in the diabatic basis (for comparison, the couplings at $\mathbf{k} = \overline{S}$ are shown in Figure B4). These couplings span a rather large range of strengths within each angular momentum channel. Most *d*-states show rather small couplings, seemingly supporting the prevalent *sp*-band model of ET [27, 28]. Yet, they are not zero, and in fact do show similar strengths as *s*- and *p*-like states in the energy region close to the donor level. In fact, the high symmetry of the Ar4*s*4p_z donor state, as well as its position on the on-top site, allow to nicely understand these varying couplings in terms of textbook rules of orbital phase cancelation. Figure 4.12a illustrates this for four select acceptor states. Acceptor state i) is a bulk *d*-state with hardly any presence in the surface layer and a correspondingly vanishing coupling. State ii) is a *p*-like state which is in-phase with the donor orbital in the $\mathbf{k}_{||}$ direction, resulting in strong overlap and coupling. State iii) is the same state but out-of phase (antibonding) in the $\mathbf{k}_{||}$ direction, resulting in a cancellation of phase and a corresponding zero coupling. Finally, state iv) is an intermediate case with a corresponding intermediate coupling.

In contrast to a mere (angular momentum projected) DOS the computed chemisorption function $\Delta_{\mathbf{k}=\Gamma}(\epsilon)$ shown in Figure 4.12b appropriately accounts for these varying couplings, with its value $\Delta_{\mathbf{k}=\Gamma}(\epsilon_d)$ at the donor level energy then yielding the broadening for the Ar adsorbate and the concomitant ET lifetime. Coincidentally, the Γ-only WDOS displayed Figure 4.12b already seems to provide, when evaluated at the donor resonance energy, lifetimes directly comparable to experimental results [79, 136, 137]. Notwithstanding, we

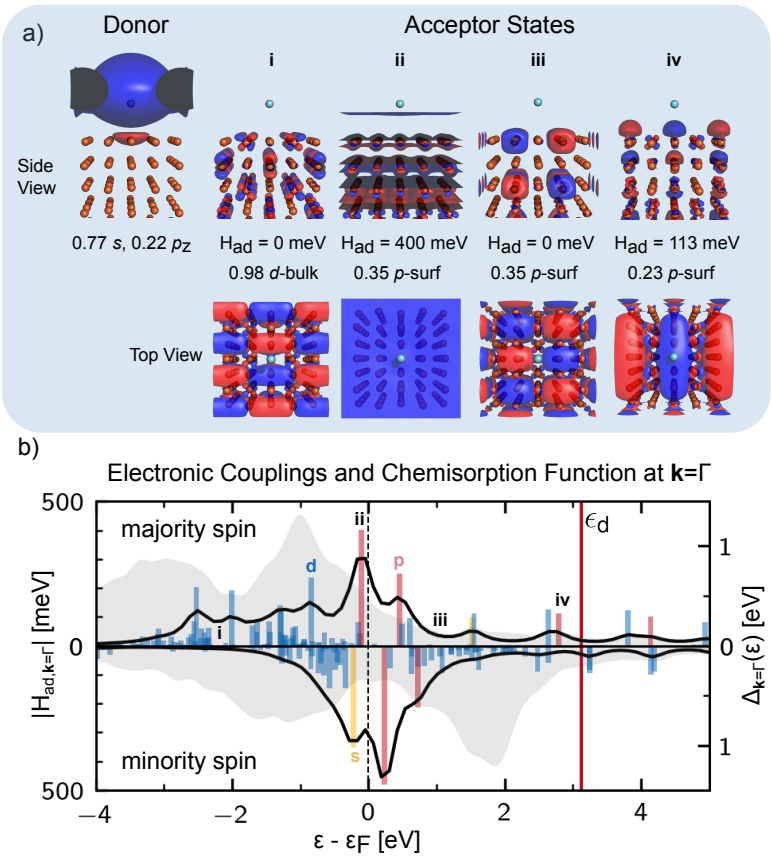

Figure 4.12: Diabatic states and couplings for the Ar/Fe(110) system of Figure 4.11. a) Real-space representation of the POD2D Argon donor state, revealing its $4s4p_z$-type hybridization (isovalue 0.01 $e^{1/2}Å^{-3/2}$), as well as of four select acceptor states indicated in panel b) (isovalues 0.05 (side views) and 0.02 (top view) $e^{1/2}Å^{-3/2}$). In each case, the electronic coupling H_{ad} to the donor and the (Mulliken) character are indicated. b) Electronic couplings H_{ad} between the donor and all acceptor states are shown on the energy axis, colored according to the dominant character of the acceptor state in the metal slab (s = yellow, p = red, d = blue). The resulting chemisorption function $\Delta_{\mathbf{k}=\Gamma}(\epsilon)$ (Equation3.39) is shown as a black line. The predicted Ar donor state energy ϵ_d is marked with a red vertical line. For comparison, the $\mathbf{k}$ = Γ DOS of the slab is shown light grey. This figure has been reused with permission from Reference [2] and has been submitted for publication. After it is published, it will be found at The Journal of Chemical Physics.

stress that the actual agreement here is in fact largely fortuituous. Primarily due to band folding, the WDOS merely evaluated in the Γ-point approximation is highly sensitive to the employed size of the periodic supercell. We illustrate this in Figure A3 for a range of cell sizes. It is found that the chemisorption function within a Γ-point approximation only slowly converges with cell size, making it insufficient for the prediction of lifetimes at reasonable slab sizes. To really achieve a quantitatively converged chemisorption function, a proper integration over the BZ is indispensable.

Brillouin-zone integrated results

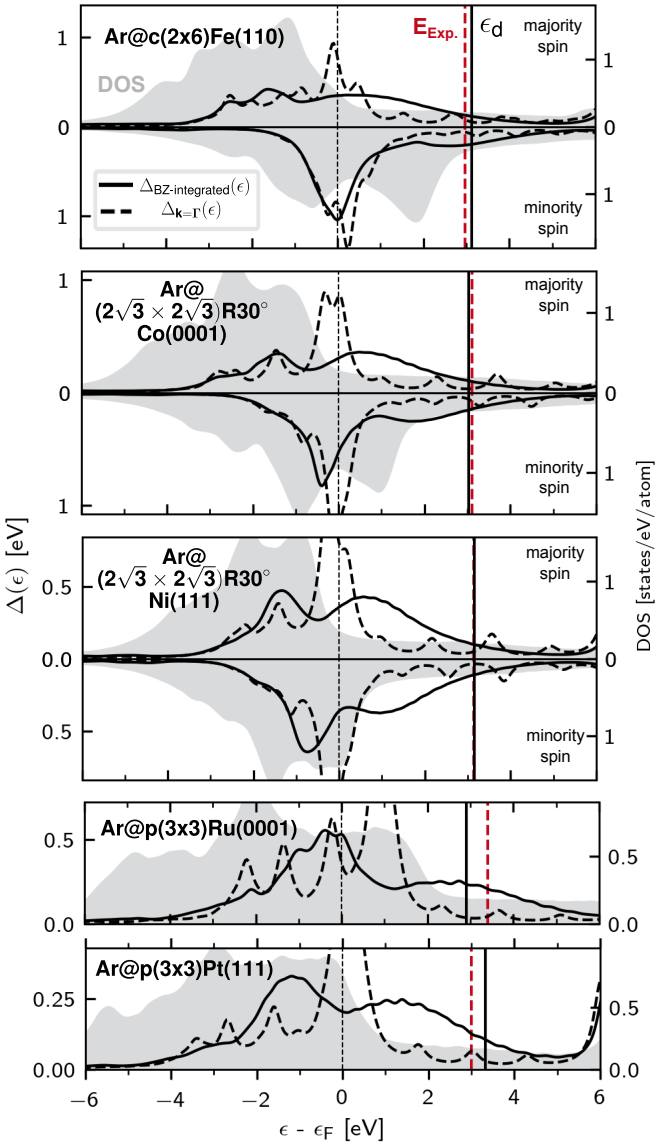

Figure 4.13: Brillouin-zone integrated chemisorption function (solid line) for the Ar4s4p_z compared to the chemisorption function obtained at Γ-point (dashed line). The (POD2$_d$,frag$_a$)GS method is used. The BZ-integration is performed on a (12×12×1) k-grid. Both functions contain a Lorentzian broadening of 0.2eV. The experimental and calculated resonance energies are shown with vertical red and black lines, respectively. The DOS of the metal surface layer is shown for comparison. This figure has been reused with permission from Reference [2] and has been submitted for publication. After it is published, it will be found at The Journal of Chemical Physics.

We show in Figure 4.13 now the (POD2$_d$,frag$_a$)GS chemisorption function for the Ar4s4p_z donor on five transition metal surfaces after appropriate integration over the full Brillouin

zone (full lines) using Equation (3.40). To highlight the influence of BZ integration we depict the respective Γ-point results (dashed lines) alongside the **k**-converged chemisorption functions. Next to the noticeable differences between the two functions, we note that the BZ-integrated chemisorption function is actually largely independent of the slab size, unlike the Γ-point result. As depicted in Figure A6, we find the BZ-integrated WDOS to converge very well with slab depth, showing very little to no change beyond 4 layers. In contrast, the chemisorption function at k=Γ is highly sensitive to slab size. We also find significant differences between the integrated and Γ-only WDOS' especially at the Argon donor energies. These, in turn, lead to noticeably different predictions for the lifetimes (Equation 3.38) of the core-excited Ar state, listed in Table A5. The importance of BZ-sampling is thus clear to achieve a converged and interpretable ET rate.

Table 4.2: Summary of ET systems studied in this work with the ($POD2_d$,$frag_a$)GS diabatization method. The resonance energy prediction (averaged over the Brillouin zone) is given in eV from Fermi level. Lifetimes are in fs, contain a Lorentzian broadening of 0.2eV and are averaged over a 12x12x1 Monkhorst-Pack k-grid. Relative signed errors (RSE) with respect to experimental lifetimes are shown. Mean relative signed error (MRSE) of the calculated Argon lifetimes compared to all experimental values is -6%. (MRSE For spin majority -0.3% and minority -12%). This table has been reused with permission from Reference [2] and has been submitted for publication. After it is published, it will be found at The Journal of Chemical Physics.

	Experiment			Diabatic method				
System	E_{res}	$\tau_{maj.}$	$\tau_{min.}$	E_{res}	$\tau_{maj.}$	$\tau_{min.}$	RSE_{maj}[%]	RSE_{min}[%]
Ar/Fe(110) [136]	2.97	2.67	2.08	3.125[1]	2.88	1.66	+8	-20
Ar/Co(0001) [136]	3.11	3.24	2.63	3.038[2]	3.15	2.14	-2	-19
Ar/Ni(111) [136]	3.14	3.12	3.12	3.15	3.43	2.93	+10	-6
Ar/Ru(0001) [79]	3.4	1.5	-	2.91	1.41	1.41	-6	-6
Ar/Pt(111) [137]	3.0	3.51[3]	-	3.325	3.14	3.13	-11	-11

The k-point integrated and converged chemisorption function now allows us to compute ET lifetimes (Equation 3.38) comparable to experiment as illustrated in Figure 4.14a for the transfer from $Ar^*(2p_{3/2}^{-1}4s)$ to the five metal surfaces. Additionally, the results are summarized in Table 4.2. Experimental lifetimes, lifetime errors (when reported), and resonance energies for ferromagnetic systems Fe(110), Co(0001) and Ni(111) were taken from the same publication [136], while those of Ru(0001) [79] and Pt(111) [137] are from separate, older works. For the core-hole measurement on Ar/Pt(111) [137], no lifetime was reported. It can, however, be estimated with the same method as used in Reference [79]. The calculated lifetimes have an overall mean relative signed error of -6% and mean signed error of -0.14fs compared to the experimental values. The qualitative and quantitative differences in lifetimes over the surfaces, and, for ferromagnetic systems, between spin channels, are captured excellently.

It is appropriate here to consider the influence of the diabatization scheme upon the lifetime predictions. The convergence properties with respect to Brillouin-zone sampling, basis sets, and finite slab size were established above. The diabatic representation of systems is in general non-unique, and will affect the prediction of lifetimes. In Appendix A.4, we compare lifetimes predicted with ($POD2_d$,$frag_a$)GS and ($frag_d$,$frag_a$)GS schemes, as well as their non-orthogonalized counterparts. It is found in Table A5 and Figures A15,A16 that the ($POD2_d$,$frag_a$)GS representation yields the most accurate resonance energy predictions as well as electron transfer lifetimes for the 5 surfaces considered. The ($frag_d$) donor state (shown in Figure A14) couples too strongly with the surface, leading to underestimated lifetimes. Orthogonalization is found to reduce couplings slightly, improving overall accuracy (Figure B3). Finally, with the exception of the artifact state, the diabatic PDOS of the ($POD2_d$,$frag_a$)GS scheme, shown in Figure C8 is found to be consistent with the adiabatic

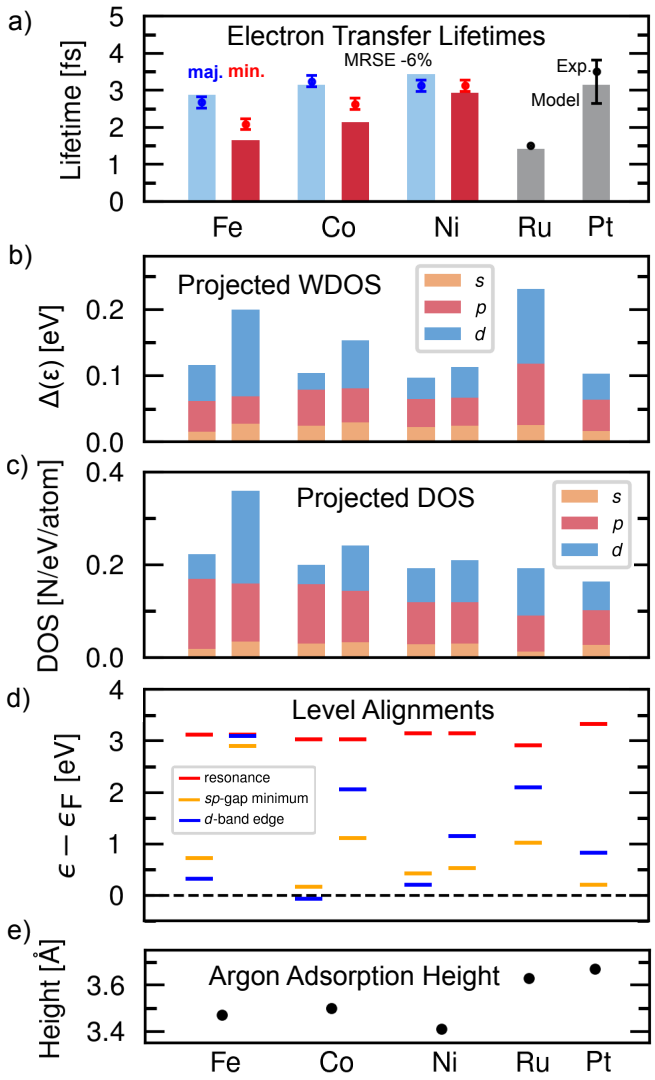

Figure 4.14: a) Calculated electron transfer lifetimes (vertical bars) compared to experimental values (dots, errorbars shown when reported). The lifetimes may be understood in terms of parameters describing the systems: b) the value of the chemisorption function (WDOS) and c) the DOS of the surface layer at the resonance energy, as well as their angular momentum decompositions, d) the alignment of the surface bands relative to the resonance, and e) the adsorption height of the Argon above the on-top site on each surface. Correlations are analyzed in Figures 4.15, C1 and C2. This figure has been reused with permission from Reference [2] and has been submitted for publication. After it is published, it will be found at The Journal of Chemical Physics.

PDOS of Figure E1. In contrast, the (frag_d,frag_a)GS underestimates the donor energy (Figure C5). The consistency of the PDOS between diabatic and adiabatic representations is an important way to measure the suitability of representations in the absence of experimental data. Due to superior performance in these aspects, the (POD2_d,frag_a)GS scheme is chosen as the most suitable and used throughout this work.

Having established the suitability of our approach, and its agreement with experiment, we now examine the contributions of different acceptor states, specifically focusing on the angular momenta. For comparison, Figures 4.14b and c, respectively depict the WDOS and surface-DOS evaluated at the resonance energies and both resolved by angular momentum contributions. To this end, we employ a Mulliken analysis of both the DOS and WDOS, shown in Figure C4.

The angular-momentum components of the WDOS (which we shall call the projected-WDOS or pWDOS) thus contain the weights of each state *by character*. The pWDOS can thus be seen as a projected DOS weighted by couplings, and thus shows the dominant character of the states which participate in the overall lifetime broadening. It does not necessarily show the character which is associated with strong coupling (indeed, coupling and character are nontrivially related, as was seen in Figure 4.12).

Figure 4.14b shows that states which participate in the overall lifetime broadening have, on average, significant *d* as well as *sp*-character. This is of course consistent with the hybridized nature of states at the resonance energy. However, we see upon closer examination that it is the changing *d*-character of the states which is found to decisively determine the differences in lifetimes over the surfaces and spin channels, while the *sp*-character is relatively unchanged.

Considering other popular modes of interpreting ET lifetimes, the DOS depicted in Figure 4.14c indeed bears some qualitative resemblances to the WDOS. Importantly, the WDOS, due to its inclusion of phase effects, captures more closely the variations among the surfaces, in closer agreement with the experimental lifetimes than the DOS. In particular, the DOS fails to capture the difference between the shortest (Ru) and longest (Pt) lifetimes. The WDOS, on the other hand, shows a much higher value on Ru than Pt, despite similar DOS values on the surfaces. As Argon adsorbs approximately at the same height on these two systems—cf. Figure 4.14e, the large difference in lifetimes on Ru and Pt is strongly related to different electronic couplings, determined both by the spatial extent of the surface wavefunctions and specific phase effects.

Finally, in Figure 4.14d we depict the onsets of the *sp*-gap and the *d*-band together with the resonance energy. The *sp*-gap onset is thereby evaluated from the primitive band structures of all five surfaces (Figure E3), while the *d*-band edge is extracted from the materials' surface DOS at a cutoff of 0.2 [states/eV/atom]. Both, the proximity of the resonance to the *sp*-band gap onset and to the *d*-band appear to correlate well with the lifetimes. Yet, we note for example that for Fe, very different *sp*-bandgap onsets appear in the majority and minority spin channels, while the *sp*-DOS and *sp*-WDOS are nearly identical in both spin channels, indicating little influence of band gap alignment on the couplings or DOS of the *sp*-channel (indeed, the parabolic gap should have a nearly constant DOS similar to the 2D free electron gas). In contrast, the difference of the *d*-band edge between the spin channels corresponds to a large difference in both the *d*-band DOS and WDOS.

For a clearer analysis of such relationships, we correlate the ET lifetimes against features of the electronic structure in Figures 4.15. We find that the calculated lifetimes correlate

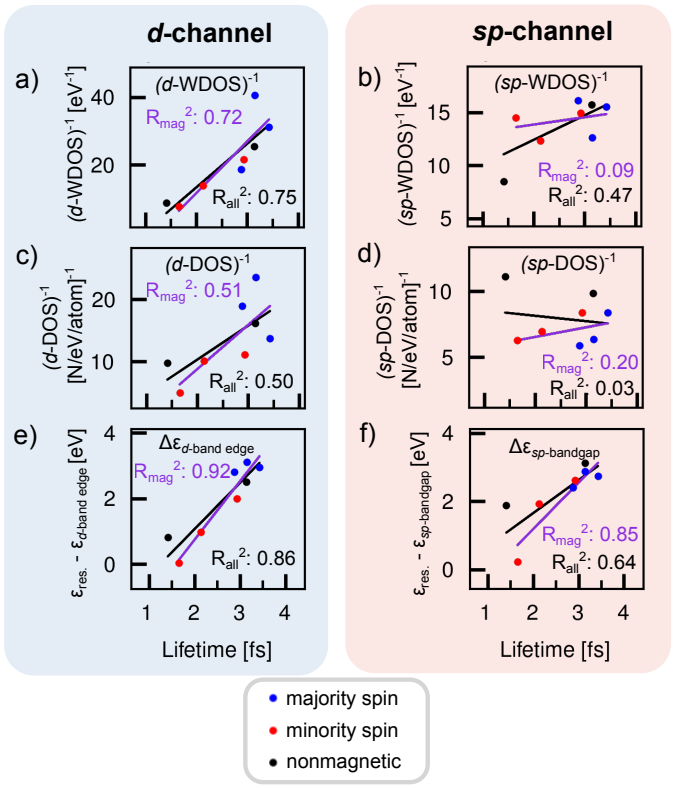

Figure 4.15: The predicted electron transfer lifetimes from Figure 4.14 are tested for correlation with electronic structure properties of the surfaces. A linear regression is shown for all datapoints (black line) and seperately for magnetic systems (violet line). The angular-momentum components of the WDOS are depicted: a) contains the WDOS weighted by the *d*-character of states and b) the WDOS weighted by the *sp*-character of states. The projected DOS of the surface is shown: c) contains the DOS weighted by the *d*-character and d) the DOS weighted by the *sp*-character of states in the surface layer. Finally, the proximity of the resonance energy to the edge of the *d*-band is depicted in e), with the onset energy of the *sp*-band gap depicted in d). This figure has been reused with permission from Reference [2] and has been submitted for publication. After it is published, it will be found at The Journal of Chemical Physics.

strongly with (coupling-weighted) *d*-character of the acceptor states, and weakly with their *sp*-character. In Figures 4.15a,b, the (inverse) WDOS *d*-channel is seen to correlate strongly with the lifetimes, while the *sp*-channel of the WDOS correlates poorly. This correlation is even worse for the investigated magnetic systems. Furthermore, coming back to the simple Tersoff-Hamann picture, the ET rate should be proportional to the local DOS at the probe coordinate (approximated here as the DOS of the surface layer). In Figures 4.15c,d, we correlate the lifetimes against the inverted *d* and *sp* components of the DOS, respectively. Thereby, we observe a very slight correlation between the lifetimes and inverse DOS of the *d*-channel, but none at all for the *sp*-DOS, consistent with the lack of phase information in this simple picture. Additionally, while our predicted lifetimes correlate strongly with the proximity of the resonance to the *sp*-band gap onset as depicted in Figure 4.15f, we find them to correlate poorly with the *sp*-component of the DOS (Figure 4.15d and the *sp*-WDOS

(Figure 4.15b). Instead, there is a strong correlation of the lifetimes with the *d*-band edge, which may be explained by an increasing diffusivity of states with energy [28], or simply by the increase in the *d*-band DOS magnitude at the *d*-band edge. The energy of the *d*-states is captured in the *d*-band edge descriptor, and indeed strongly correlates with the *d*-band WDOS, as seen in Figure C2c.

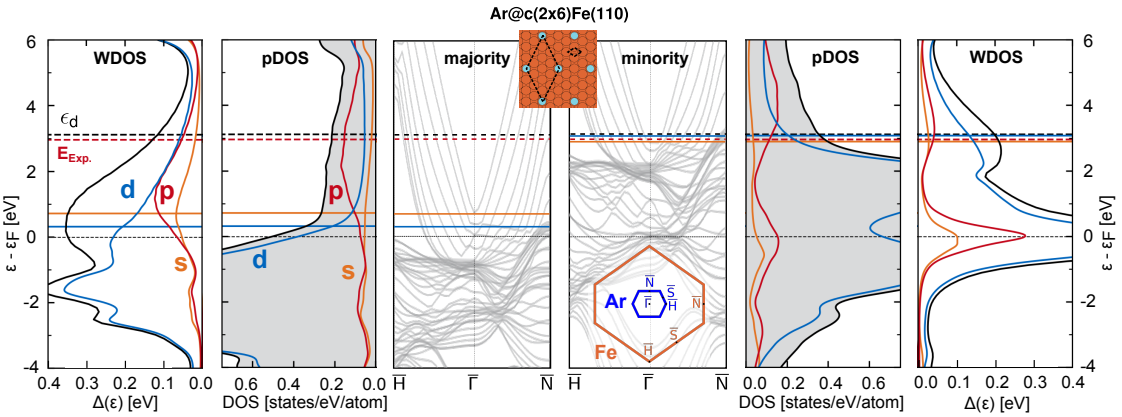

Figure 4.16: The chemisorption function of the Ar/Fe(110) c(2x6) system is compared to the surface-projected DOS, and to the band structure of the surface primitive cell. The nontrivial relationship between the DOS and the WDOS arises due to the electronic couplings, which contain e.g. phase cancellation effects. The *sp*-band gap onset, marked with an orange horizontal line, is associated with a local maximum in the chemisorption function followed by a monotonic decay, consistent with the role of the band gap identified in earlier work, and with the experimentally-measured energy dependence of the ET process. The *d*-band edge is marked with a blue line, and the experimental and predicted Ar4*s* resonances are indicated. Other systems are shown in Figures C4 and E3. This figure has been reused with permission from Reference [2] and has been submitted for publication. After it is published, it will be found at The Journal of Chemical Physics.

We find that similar observations can be made when interpreting the energy dependence of the predicted electron transfer lifetimes. While the connection between the WDOS and excited-state lifetimes only strictly holds at the resonance energy cf. Figure 3.38, assuming an unaffected nature of the donor state, one could use it to interpret experimental findings for other incidence energies. They show growing lifetimes for larger incidence energies beyond the resonance [52, 79, 142]. Furthermore, local maxima in the ET rates below the resonance have been observed experimentally [137] on Ar/Pt(111) and in accurate Green's Function-based simulations [28] of Ar/Ru(0001). Both of these trends are reproduced in the WDOS as depicted in Figure 4.13. Theoretically, the energy dependence of lifetimes has alternatively been attributed to the declining DOS of the *d*-states (already in 1998 by Menzel and co-workers [142, 143]), or to the effect of the band gap in the *sp*-states originally proposed by Gauyacq and Borisov [28, 82, 83]. Upon examination of the WDOS components over the energy scale, as shown in Figure 4.16 for Ar/Fe, we find that the energy dependence at resonance arises from significant contributions from both *d*- and *sp* components, combining the two explanations proposed earlier. The onset of the *sp*-band gap, which is marked with an orange line in Figure 4.16, is associated with a local maximum in the WDOS, followed by a sharp monotonic decay which differs from the oscillatory behavior observed at lower

energies. The decay behavior is consistent with the decay of couplings to *sp*-type states with $\mathbf{k}_{||}$ in the gap region proposed earlier [28]. While we relegate a more detailed study of such dependencies to future work (the present model is based on the folded band structure, (Figure E2), we do observe this suppression of the *p*-channel WDOS in the band gap region of all systems (Figure C4) —against quite different behavior in the PDOS—indicating a systematic relationship between the WDOS and the band structure.

Finally, observing the nontrivial relationship of the DOS and WDOS over the energy scale, we can furthermore better understand the (lack of) correlation of the ET lifetimes with the *d*- and *sp*-channels established above. For this, we may consider the nature of the couplings themselves. States with strong *sp* character, which have large spatial extent and presence on the surface, may nevertheless have vanishing couplings due to phase cancellation (cf. Figure 4.12). Their presence in the pWDOS, compared to the PDOS, is thus suppressed near the resonance in Figure 4.16. The more localized *d*-bands, on the other hand, couple via their exponential tails and are thus less effected by phase cancellation. Chen related [49–51, 144] the coupling matrix elements to the gradients, rather than the squared-modulus (density), of participating states. As such, we may anticipate qualitatively different coupling behaviors from the localized (high-gradient) *d*-band states compared the more diffuse (and uniform) free-electron-like *sp*-bands above the Fermi level.

These effects are meaningfully elucidated by constraining the donor to have purely 4s character, within the (frag_d,frag_a)GS method. Upon removal of the $4p_z$ hybridization, depicted in Figures C4 and C5 we recover a much stronger relationship between the *d*-WDOS and *d*-DOS over the full energy scale. Nonlinearity between the *sp*-DOS and *sp*-WDOS is meanwhile enhanced, confirming the increased vulnerability of these acceptor states to strong phase effects.

5 Conclusions

This dissertation has explored the development of quantitative schemes for the calculation of the electronic coupling parameter H_{ad} from first-principles Density Functional Theory (DFT). The Projection-Operator Diabatization (POD) method [24, 71] was modified to yield improved basis set stability and accuracy in the methods POD2L and POD2GS, as demonstrated in the Hab11 [74] benchmark of molecular dimers. The improved numerical stability allows for use of the schemes at arbitrary levels in the atomic basis set hierarchy, increasing the utility of the diabatization methods, and allows for the exploration of physical effects such as polarization and exact exchange and their role in the electronic coupling [1].

We extended these approaches to the study of adsorbed surface systems, using core-excited Argon on transition metals as an example. Here, diabatization schemes were proposed in addition to a strategy for their use with the quasi-continuum of the (metal) surface, as well as the consideration of periodic boundary conditions. Following the model of Newns [53], we use the Bloch states of the isolated surface ($frag_a$) as diabats for the acceptor system (a) and use as donor diabats (d) either the Bloch states of the isolated adsorbate monolayer ($frag_d$) or those of the adsorbate block in the Kohn-Sham Hamiltonian of the combined system ($POD2_d$). The states are Gram-Schmidt (GS) orthogonalized, and the resulting diabatic bases are termed ($frag_d$,$frag_a$)GS and ($POD2_d$,$frag_a$)GS. Projection upon the ($POD2_d$,$frag_a$)GS is found to yield a diabatic representation of the electronic structure from which accurate ET lifetimes can be extracted for core-excited Argon on five transition metal substrates. For this, the electronic couplings are used to construct a first-principles Newns-Anderson chemisorption function which gives the line broadening of the initially populated Argon LUMO state on the surface.

The consideration of convergence aspects and the validation of couplings against quantitative reference data is emphasized throughout the work, as the electronic couplings (and diabatization schemes in general) are non-unique. While the ($POD2_d$,$frag_a$)GS scheme is the most accurate, it is found that the electron transfer lifetimes offered by different diabatization schemes may also agree reasonably with experiment despite offering different qualitative behaviors. For example, a fortituous agreement of lifetimes calculated in the Γ-point approximation with experiment is observed, despite the sensitivity of this chemisorption function to finite size effects. Also, the ($frag_d$,$frag_a$)GS is found to yield lifetimes similar to ($POD2_d$,$frag_a$)GS at the resonance energy of the ET process, despite having a funda-

mentally different chemisorption function at other energies and lacking the understood hybridization of the donor state [28]. For the validation of the chemisorption function across the energy scale, we assessed it against the energy dependence of the electron transfer measurements, as well as against phase-cancellation behaviors, such as Chen's Derivative Rules [49] anticipated from the theory of Scanning Tunneling Microscopy [47, 50, 51].

Having gained confidence in the validity of the couplings over the energy scale, we interpret the chemisorption function and query it to elucidate the ultrafast electron transfer process. A key insight is the finding of a significant role for the transition metal *d*-type character, which is found to correlate with the variation in lifetimes over spin channels and surfaces, in contrast to the previous understanding of the process based on models of the *sp*-type band structure.

The chemisorption function thus proves advantageous for the understanding of the resonant electron transfer process, which occurs some 3eV above the Fermi level. However, the chemisorption function is also used elsewhere in the literature, such as in descriptions of bonding on surfaces with the Newns-Anderson model [39, 63], or – also called a *hybridization function* – in the description of highly correlated many-body physics such as the Kondo Effect [18, 30] in e.g. single-spin adsorbates. In such applications, the behavior of the chemisorption function over the full energy range may be considered. It is hoped that this work lays the foundation for a quantitative, first-principles exploration of such phenomena with the chemisorption function. Judging from this work and other local representations of the electronic structure, it is clear that the diabatic representation of strongly-interacting (e.g. covalently bound) systems will face challenges, such as more severe basis set superposition effects. However, the present methods may serve as a starting point for the development of representations for such systems which are nevertheless meaningful and similarly advantageous. This will be the topic of future work.

Appendices

A Convergence Properties of the Chemisorption Function

Sensitivity of the chemisorption function to various aspects is here analyzed. Parts of the following sections have been reused with permission from Reference [2] and have been submitted for publication. After they are published, they will be found at The Journal of Chemical Physics.

A.1 Sampling the Brillouin Zone

In Figures A1-A4, sampling the Brillouin zone is found necessary in order to acquire a chemisorption function which is robust against finite size effects. The Lorentzian broadening of 0.2eV, used throughout this work, is also motivated in Figure A2.

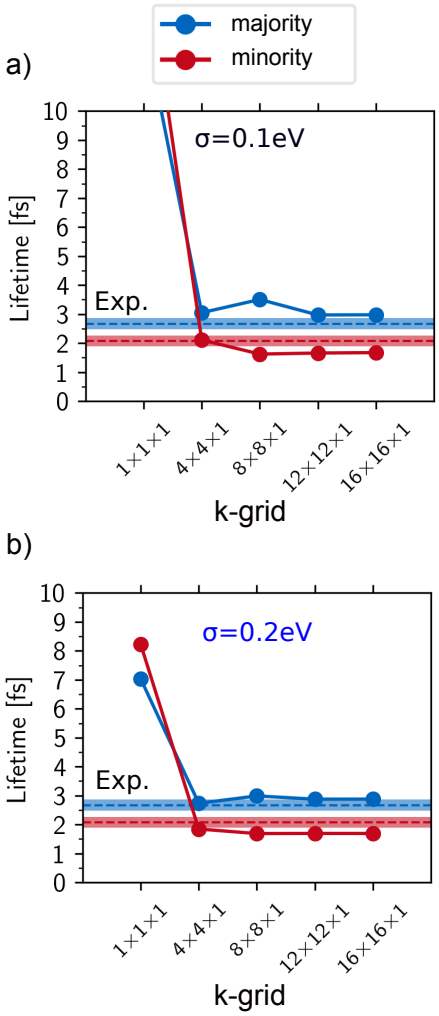

Figure A1: **Sampling the Brillouin zone: k-grid convergence and Lorentzian broadening.** The convergence of lifetimes at the predicted resonance energy ϵ_d =3.125 eV is shown with respect to k-grids, for two fixed values of the Lorentzian broadening. With a larger k-grid, a smaller value of the Lorentzian broadening is necessary for a smoothe chemisorption function. As a production setting, the Lorentzian broadening of σ=0.2eV is chosen in combination with the 12x12x1 k-grid. The demonstration has 4 metal layers with basis set Light Tier4 in the top layer and Light Tier 1 in all lower layers. This figure has been reused with permission from Reference [2] and has been submitted for publication. After it is published, it will be found at The Journal of Chemical Physics.

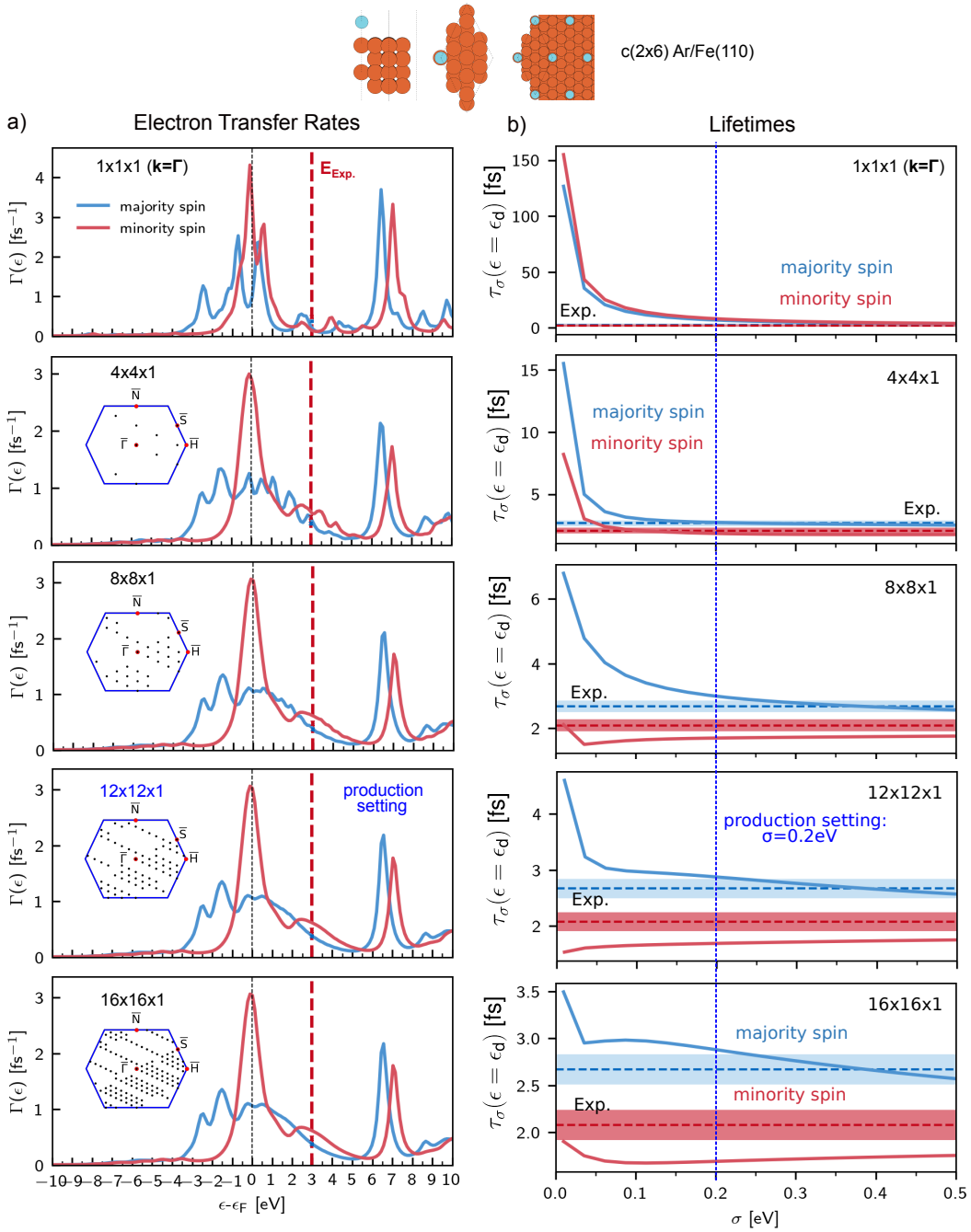

Figure A2: **Sampling the Brillouin zone: k-grid convergence and Lorentzian broadening.** a) The (POD2$_d$,frag$_a$)GS chemisorption function is shown as a spin-dependent ET rate for the Ar/Fe(110) c(2x6) overlayer model at k=Γ point and for different Monkhorst-Pack k-grids. The Lorentzian broadening is fixed to σ =0.2eV. The experimental resonance energy is a vertical red line. b) The ET rate at the predicted resonance energy ϵ_d =3.125 eV is converted to a lifetime and shown for different values of the Lorentzian broadening. With a larger k-grid, a smaller value of the Lorentzian broadening is necessary for a smoothe chemisorption function. As a production setting, the Lorentzian broadening of σ=0.2eV is chosen in combination with the 12x12x1 k-grid. The demonstration has 4 metal layers with basis set Light Tier4 in the top layer and Light Tier 1 in all lower layers. This figure has been reused with permission from Reference [2] and has been submitted for publication. After it is published, it will be found at The Journal of Chemical Physics.

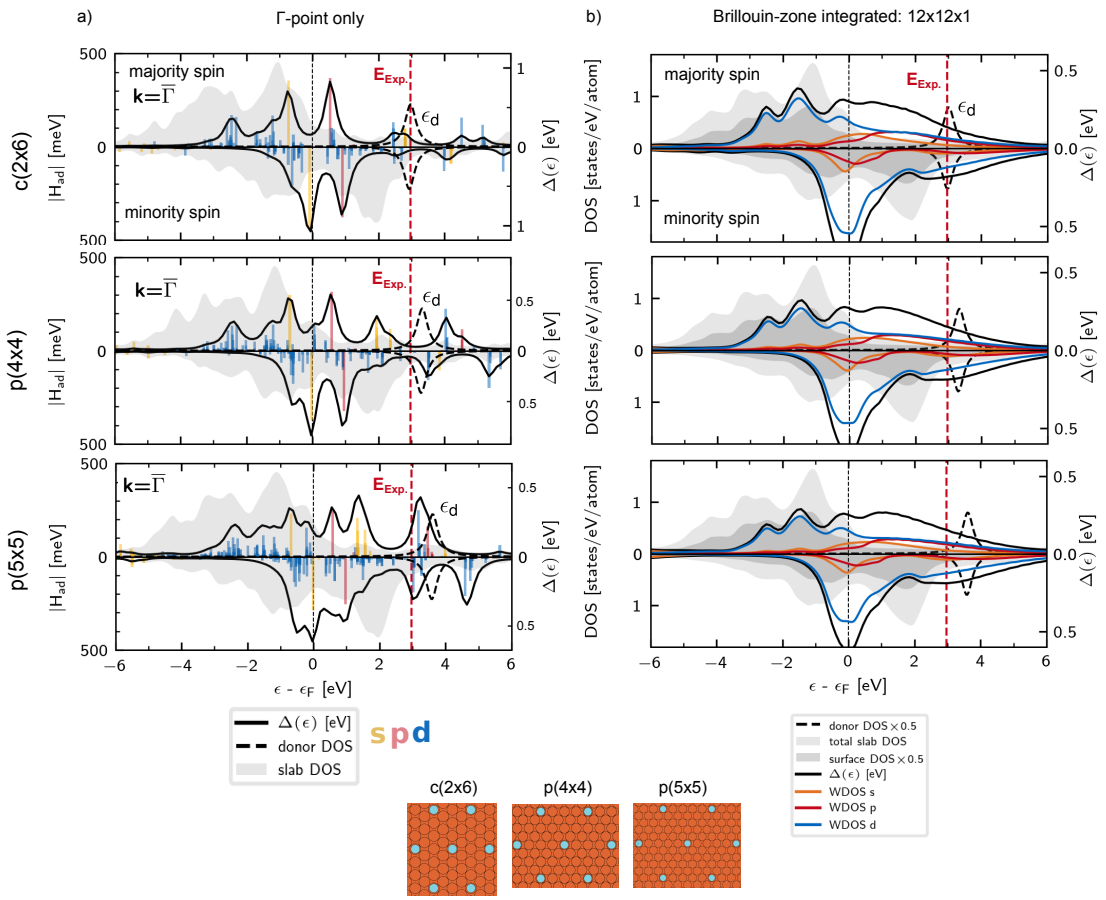

Figure A3: **The insufficiency of the Γ-point approximation.** a) The electronic couplings and chemisorption function at $\mathbf{k}_{||} = \Gamma$ are seen to vary strongly with slab size due to band folding. b) A proper Brillouin zone integration results in a chemisorption function which displays proper size- consistent behavior and is robust against finite size effects. In the limit of (intractably) large slab size, the chemisorption function at $\mathbf{k}_{||} = \Gamma$ is expected to converge to that averaged over the Brillouin zone. The systems shown are the same as Figure A8, with 4 layers of metal and using the Light Tier 1 in all metal layers. Argon elevation is fixed to 3.5 Å and the Argon basis set is 6-311+G**. This figure has been reused with permission from Reference [2] and has been submitted for publication. After it is published, it will be found at The Journal of Chemical Physics.

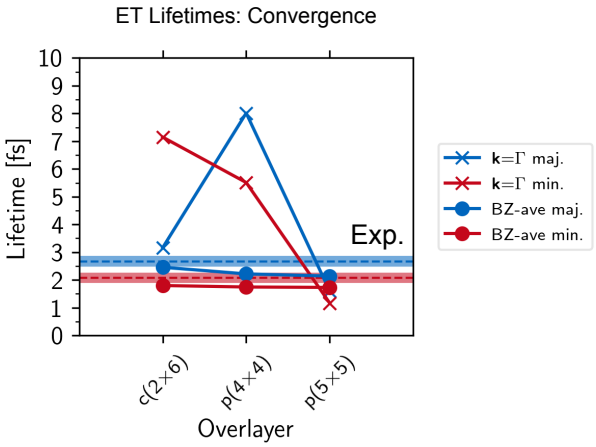

Figure A4: **The insufficiency of the Γ-point approximation.** ET lifetimes evaluated at the experimental resonance energy (red dashed line) for all three coverages, comparing results at $\mathbf{k}_{||} = \Gamma$ and using the 12x12x1 BZ-integration. This confirms the strong dependence of the $\mathbf{k}_{||} = \Gamma$ lifetimes on the slab size and the stability of the BZ-averaged chemisorption function against slab size effects. The c(2x6) overlayer is also seen to be a reasonable approximation of the low-coverage limit. Lorentzian broadening is σ=0.2eV and BZ-averaging is performed on the 12x12x1 k-grid. The systems shown are the same as Figure A8, with 4 layers of metal and using the Light Tier 1 in all metal layers. Argon elevation is fixed to 3.5 Å and the Argon basis set is 6-311+G**. This figure has been reused with permission from Reference [2] and has been submitted for publication. After it is published, it will be found at The Journal of Chemical Physics.

A.2 Cell Depth

In Figures A5 and A6, it is found that the (BZ-averaged) chemisorption function of the c(2x6) Ar/Fe(110) overlayer converges well at a depth of 4 layers. 8 layers are used as a production setting for calculating ET lifetimes.

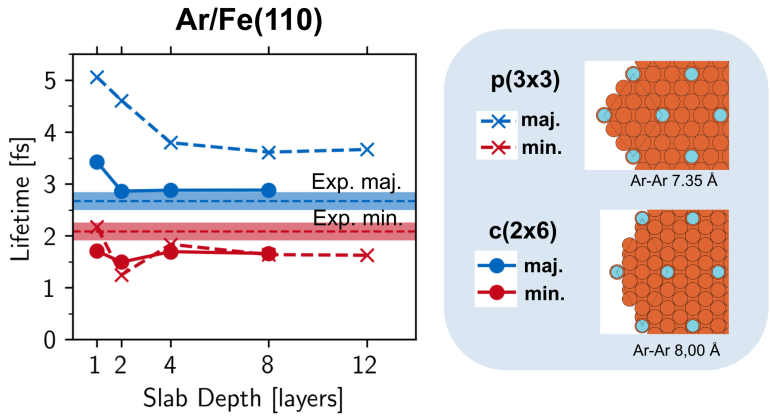

Figure A5: Convergence of electron transfer lifetimes with slab depth for two overlayer models of Ar/Fe(110) shown in Figure A6, compared to experimental [136] values (dashed horizontal lines) and errorbars (shaded regions). The ($POD2_d$,$frag_a$)GS method is used, and lifetimes are evaluated at a resonance energy of 3.125eV, which is the resonance energy of the c(2x6), 8-layer slab. A reasonable convergence in spin-dependent lifetimes is attained at 4 layers of depth. Lifetimes reported in the production calculations, Table 4.2, use 8 layers. The overlayer models yield different lifetime predictions, as the higher-coverage p(3x3) structure contains Argon-Argon nearest-neighbor interactions which modify the donor wavepacket. Nearest-neighbor Ar-Ar distance is 7.35 Å. The k-grid is 12x12x1 for both coverages. This figure has been reused with permission from Reference [2] and has been submitted for publication. After it is published, it will be found at The Journal of Chemical Physics.

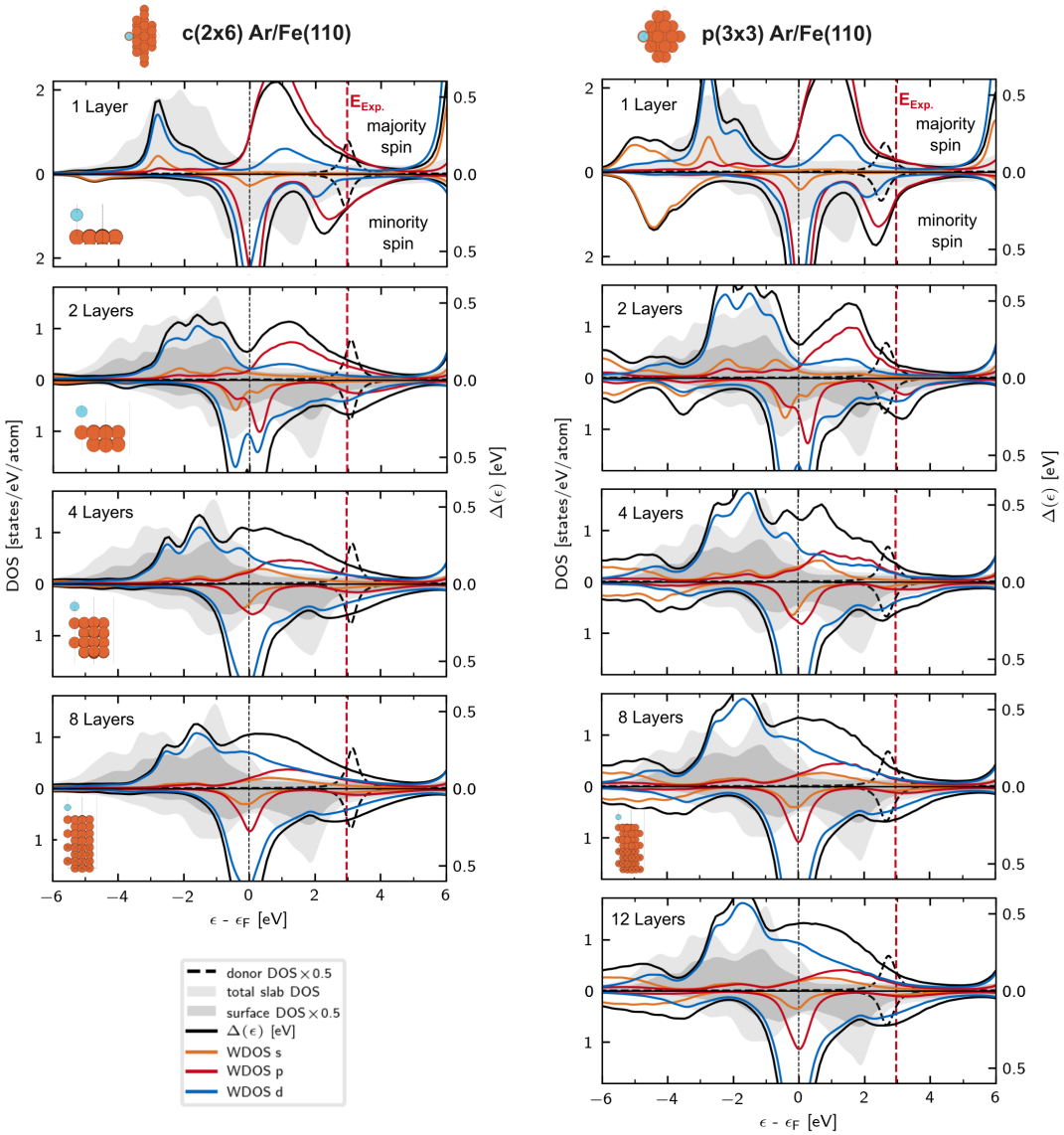

Figure A6: Convergence of the chemisorption function (WDOS) with slab depth is shown for two overlayer models of Ar/Fe(110). The (POD2$_d$,frag$_a$)GS method is used and the k-grid is fixed to 12x12x1. While 1 and 2-layer slabs are clearly not converged, 4 layers offers a reasonably converged and interpretable chemisorption function for the c(2x6) overlayer (left). We use 8 layers in our production results to calculate ET lifetimes, which differs only slightly from 4 layers in the angular momentum decomposition (colored). The higher-coverage p(3x3) chemisorption function (right) differs from c(2x6) due to the onset of undesired Argon-Argon nearest-neighbor interactions, resulting in slight dispersion in the donor band. The smaller cell nevertheless allows more layers of depth to be explored. The experimental resonance is shown as a red vertical line, and agrees well with the projected DOS of the donor state (black dashed line). All curves contain a Lorentzian broadening of 0.2eV. The demonstration has Light Tier4 basis in the top metal layer and Light Tier 1 in all lower layers. This figure has been reused with permission from Reference [2] and has been submitted for publication. After it is published, it will be found at The Journal of Chemical Physics.

A.3 Basis Sets and Monolayer Coverage

To assess the dependence of our ET lifetime predictions on the monolayer coverage and the Argon basis set, we study here the Ar/Fe(110) system at different coverages described in Table A1 and shown in Figure A8. The Light Tier 1 basis has been used on all metal layers, 4 layers of metal are used and Argon has been fixed to 3.5 Å above the surface (the settings differ slightly from our production settings in Table 4.1, which uses 8 layer slabs, a relaxed Argon geometry and Light Tier 4 in the surface layer). The p(5x5) overlayer is considered a dilute limit, as the distance between Argons exceeds twice the cutoff radius of the Argon basis functions, preventing possible overlap or dispersion.

Convergence with Dilute Limit

We first investigate whether our production model c(2x6), using the 6-311+G** Pople basis set for Argon, is well converged with the dilute limit of an isolated adsorbate. In Table A2, we find that using 6-311+G** basis, the POD2 donor state has a consistent hybridized character over the three coverages, and varies little between the c(2x6) and dilute p(5x5) structures. As a result, the chemisorption function shown in Figure A8 (top row) also varies little over these coverages. A more significant change is found in the site energy of the resonance, which is shown as a PDOS peak in Figures A8 and A10 and summarized in Table A4. The change in the resonance energy is also observed in the adiabatic PDOS, however, (Figure A10) and hence should not be attributed to the diabatization scheme. The chemisorption function, interpreted as an energy-dependent lifetime, is shown in Figure A9 and changes modestly with coverage. In Table A3, we see that upon reduction of coverage from c(2x6) to the dilute p(5x5) overlayer, lifetimes are found to increase as much as 0.5fs or 21% from their c(2x6) values, using the 6-311+G** basis. The resonance energy, Table A4 varies from 3.00 eV at c(2x6) to 3.60eV at p(5x5) (and similarly in the adiabatic PDOS), while the chemisorption function (the couplings) appears itself more stable. The primary cause of differences in the predicted lifetimes with coverage is hence the changes in the resonance energy and not the couplings. This effect is already present in the adiabatic electronic structure. We note that the core-excited Argon atom has a charge of +0.43e, due to the promoted half-electron being delocalized into the surface. The slight variation in (both adiabatic and diabatic) level alignments with slab size may be attributable to weak electrostatic interaction of Argon with its own image.

Importantly, the qualitative traits of the chemisorption function, such as the spin selectivity, and angular momentum decomposition, are stable over these coverages, and we thus consider the model at c(2x6) to be reasonably representative of the dilute limit, yielding lifetimes which are a lower bound and converged within 0.5 fs of their value at dilute coverage.

The effect of coverage on the ET lifetimes is anticipated to be approximately same regardless of the substrate species, and hence we anticipate the model to carry equivalent accuracy over our production monolayers in Figure 4.1, which have similar coverages with nearest-neighbor distances in the range of [8.00, 8.65]Å.

We additionally illustrate the size-consistent property of the chemisorption function by using

the example of He2*s*/Ru(0001) in Figure A7. It is here shown more clearly how the **k**=Γ result begins to resemble the BZ-averaged chemisorption function for very large slabs. At low coverages, the BZ-averaged chemisorption function is converged and independent of coverage (size-consistent). For this purpose, the demonstration uses only 2 layers of metal atoms.

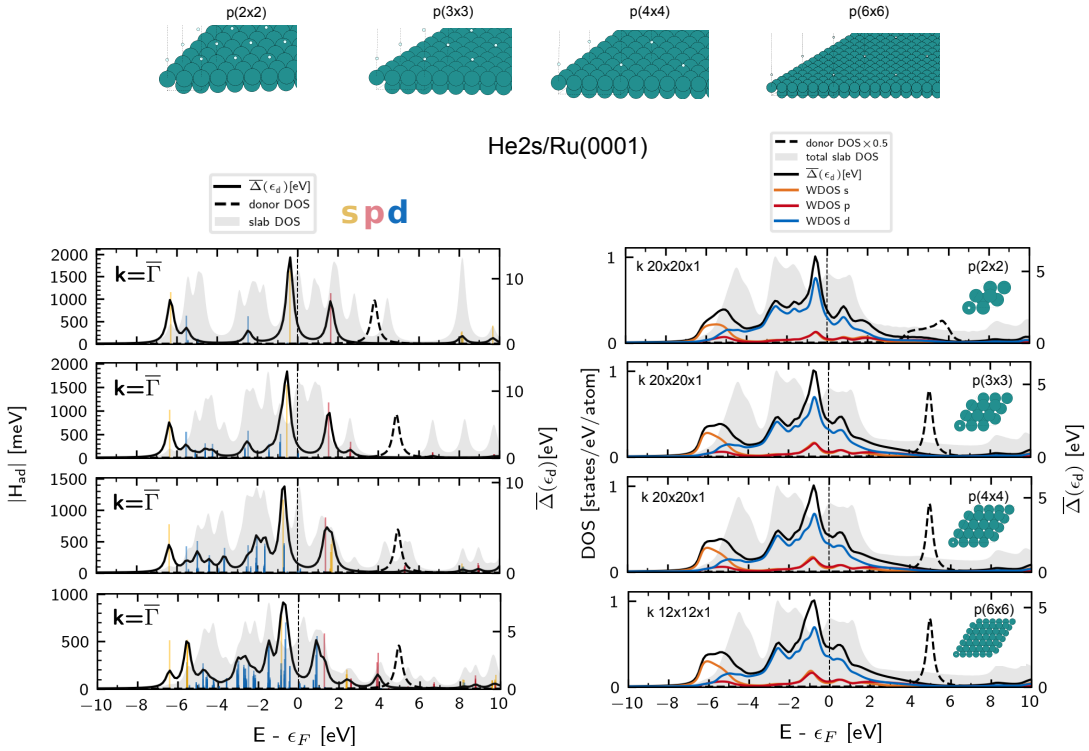

Figure A7: Right: the size-consistency of the chemisorption function is shown for a model system of He2s on 2 layers of Ru(0001). At the p(2x2) overlayer, the nearest-neighbor distance of 5.4Å is small enough to result in dispersion in the 2s band. At more dilute coverages, the chemisorption function converges to a steady value. Left: the chemisorption function at **k** = Γ converges towards the BZ-averaged chemisorption function (right) in the limit of a large slab, but varies significantly over smaller (and computationally tractable) slab sizes. The Helium atom has been placed 3.5Å on top of Ru (Argon, in comparison, adsorbs 3.63Å above Ru in Figure 4.9. Light Tier1 basis set was used for Ru slab and default Tight Tier 2 for Helium. Here, He is neutral and the (fragS,POD2D)GS method yields a 2s LUMO state which is not hybridized. The chemisorption function of He2s is qualitatively similar to that of constrained Ar4s shown in e.g. Figure C5b.

Argon Basis Set

We turn to the sensitivity of the electron transfer lifetimes to the basis set of Argon. In Figure A8, we do observe significant differences among the chemisorption functions for different basis sets and coverages. At higher coverages, significant dispersion is present in the POD2 donor state using aug-cc-pVXZ, and its character varies over the Brillouin zone. At the dilute limit, however, this has stabilized and we observe that the aug-cc-pVXZ basis sets yield a

POD2 donor wavepacket with significantly weaker $4s4p_z$ hybridization than 6-311+G** (Table A2). As a result of the stronger 4s character, the aug-cc-pVXZ basis sets show overall stronger couplings with the surface. The energy-dependent lifetimes near the resonance energy, however, vary comparatively little with the degree of wavepacket hybridization (Figure A9), consistent with previous work[27]. In the dilute case, p(5x5), lifetimes are found to decrease by as much as -1 fs or 33% from 6-311+G** values upon use of aug-cc-pV5Z. Within the aug-cc-pVXZ basis hierarchy, lifetimes change less but still -0.25fs or -12% upon changing from aug-cc-pVDZ to aug-cc-pV5Z. Lifetime predictions for different coverages and basis sets are given in Table A3.

For reasons of basis set superposition effects, no fully quantitative convergence in the ET lifetimes with basis set can be anticipated. The superposition effects may be understood by comparing the diabatic projected-DOS of Figure A10 with the conventional adiabatic PDOS of Figure A11. The consistency of the two representations will vary with basis set (and e.g. with the strength of the interaction, determined by the separation of the two systems). An increasingly large basis set on Argon will participate in the density of the surface in the combined system. Upon performing the POD2 partitioning and diagonalization of the donor block, the spectrum of the diabatic Argon subsystem, shown in Figure A10, will thus differ from the projected-DOS of the Argon within the adiabatic description (Figure A11). The most noticable difference is the artifact state below the Fermi level, which is a $4p_z$ state which has experienced a significant reduction in site energy in the diabatic system. The severity of this distortion increases from the aug-cc-pVDZ to the aug-cc-pV5Z basis sets.

The Gram-Schmidt orthogonalization scheme, which uses the overlap matrix in e.g. Equation (3.36), is also influenced by the choice of basis set. Orthogonalization reduces the magnitude of couplings, improving agreement with experiment, but also results in a more sensitive dependence of the couplings on the basis set.

We note that the adiabatic PDOS, Figure A11, itself is not anticipated to converge with basis, as this is already based on a projection of density onto localized basis functions. We justify our selection of the 6-311+G** basis set for Argon by the good agreement between the resonance energy of the POD2 donor state and that of the experiment (Table A4), and furthermore in the hybridization. The hybridization of the POD2 donor in 6-311+G** (approximately (0.75,0.25) (s,p) Mulliken character in Table A2) is more consistent with the significant degree of hybridization present in previous work [27, 28, 82, 83] (e.g. a tuned wavepacket with minimum of 30% p-type character[27]). A careful consideration of multiple basis sets should be undertaken in future applications to electron transfer lifetimes, to establish the degree of variation present in the model.

In summary, keeping to the 6-311+G** basis, we thus estimate that our model provides a lower bound for ET lifetimes which is converged with 0.5fs of the lifetime at the dilute limit. The accuracy of the model should thus be high enough therefore to meaningfully resolve differences in ET lifetimes over different substrates. The experimental lifetimes vary by over 2fs (1.5fs on Ar/Ru(0001 and 3.51fs on Ar/Pt(111)), and the difference in the spin-dependent lifetimes is 0.59fs on Ar/Fe(110) and 0.61fs on Ar/Co(0001). We note again the

approximative nature of our model, which neglects the true monolayer structure, and hence does not fully reproduce the experimental system.

Table A1: Argon-Argon nearest-neighbor distances in three overlayer models for Ar/Fe(110). The cutoff radius of the Argon basis functions is 6 Å, meaning there is zero overlap between Argons for nearest-neighbor seperations greater than 12Å. This table has been reused with permission from Reference [2] and has been submitted for publication. After it is published, it will be found at The Journal of Chemical Physics.

	c(2x6)	**p(4x4)**	**p(5x5)**
Argon-Argon distance [Å]	8.00	9.80	12.25

Table A2: The variation in Mulliken character of the POD2 donor wavepacket, for different coverages of Ar/Fe(110) and Argon basis sets. The Mulliken character has been averaged over the Brillouin zone. A weaker 4s4p$_z$ hybridization is yielded by the aug-cc-pVXZ basis sets than the 6-311+G**. The energy of the resonance also varies: Table A4. The donor wavepacket energy and character does not vary significantly with spin. This table has been reused with permission from Reference [2] and has been submitted for publication. After it is published, it will be found at The Journal of Chemical Physics.

	c(2x6)	**p(4x4)**	**p(5x5)**
Basis Set	(s, p)	(s,p)	(s,p)
6-311+G**	(0.7627, 0.2373)	(0.7622, 0.2378)	(0.7527, 0.2472)
aug-cc-pVDZ	(0.7769, 0.2228)	(0.8619, 0.1379)	(0.8513, 0.1485)
aug-cc-pV5Z	(0.7514, 0.2386)	(0.8477, 0.1452)	(0.8506, 0.1432)

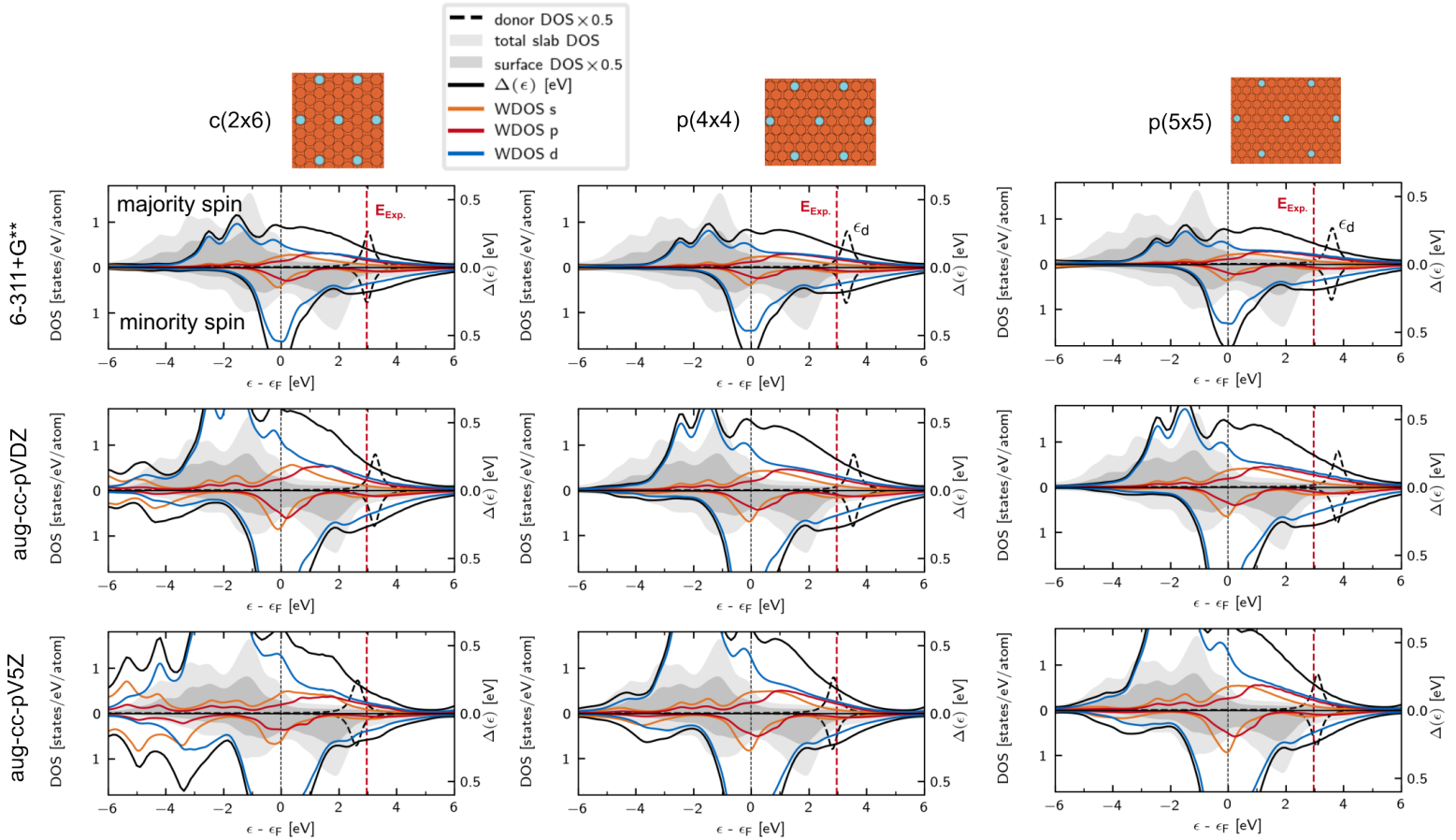

Figure A8: **Role of coverage and Argon basis set.** We show the chemisorption function of Ar/Fe(110) at different coverages and Argon basis sets. Also the projected DOS of the donor state is shown (dashed black line). The corresponding energy-dependent ET lifetimes are shown in Figure A9. This Figure has been reused with permission from Reference [2] and has been submitted for publication. After it is published, it will be found at The Journal of Chemical Physics.

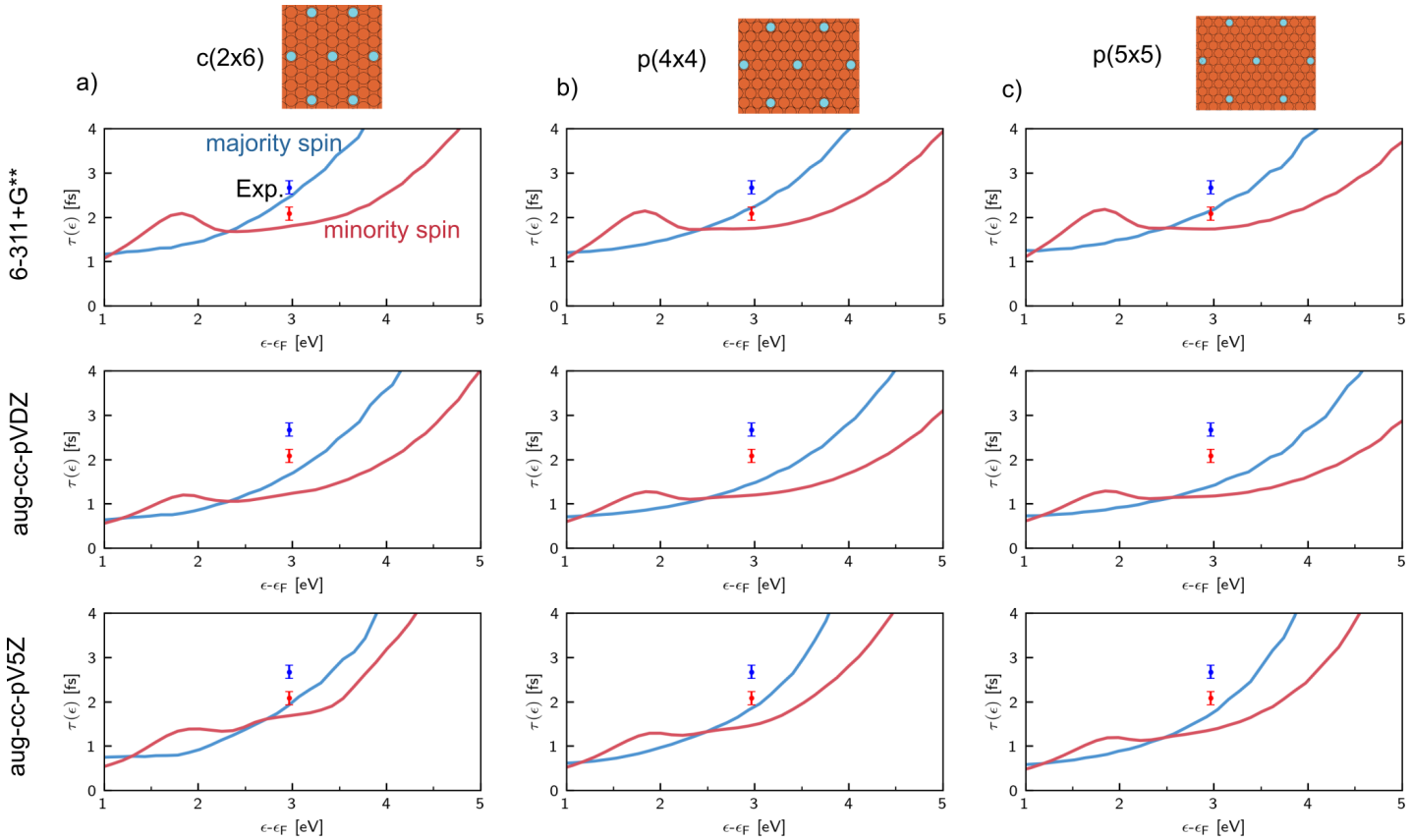

Figure A9: **Role of coverage and Argon basis set.** We show the energy-dependent ET lifetimes for Ar/Fe(110) at different coverages and Argon basis sets. The aug-cc-pV5Z basis set, due to a greater spatial extent, converges with the dilute limit only at low coverages. The resonance energy also varies over these two settings, as seen in Figure A8 which determines the final lifetime prediction given in Table A3. This Figure has been reused with permission from Reference [2] and has been submitted for publication. After it is published, it will be found at The Journal of Chemical Physics.

Table A3: Electron transfer lifetimes (in femtoseconds) calculated for different coverage of Ar/Fe(110) and Argon basis sets. The experimental values are (2.67, 2.08) fs for (majority, minority) spin channels[136]. The lifetimes are evaluated at the predicted diabatic resonance energies shown in Table A4 and Figure A8. This table has been reused with permission from Reference [2] and has been submitted for publication. After it is published, it will be found at The Journal of Chemical Physics.

	c(2x6)		**p(4x4)**		**p(5x5)**	
	majority	**minority**	**majority**	**minority**	**majority**	**minority**
6-311+G**	2.50	1.81	2.58	1.81	3.03	1.93
Aug-cc-pVDZ	2.04	1.31	2.14	1.40	2.25	1.48
Aug-cc-pV5Z	1.48	1.53	1.76	1.44	1.99	1.45

Table A4: The variation of the POD2 resonance energy, in eV, with the coverage of Ar/Fe(110) and the basis set of Argon. The diabatic resonances are visible as peaks in Figures A8 and A10. The experimental resonance lies 2.97eV above Fermi energy[136]. The changes in the peak locations are roughly consistent with those observed in the adiabatic PDOS, Figure A11. This table has been reused with permission from Reference [2] and has been submitted for publication. After it is published, it will be found at The Journal of Chemical Physics.

	c(2x6)	**p(4x4)**	**p(5x5)**
6-311+G**	3.00	3.25	3.60
Aug-cc-pVDZ	3.25	3.60	3.80
Aug-cc-pV5Z	2.60	2.90	3.13

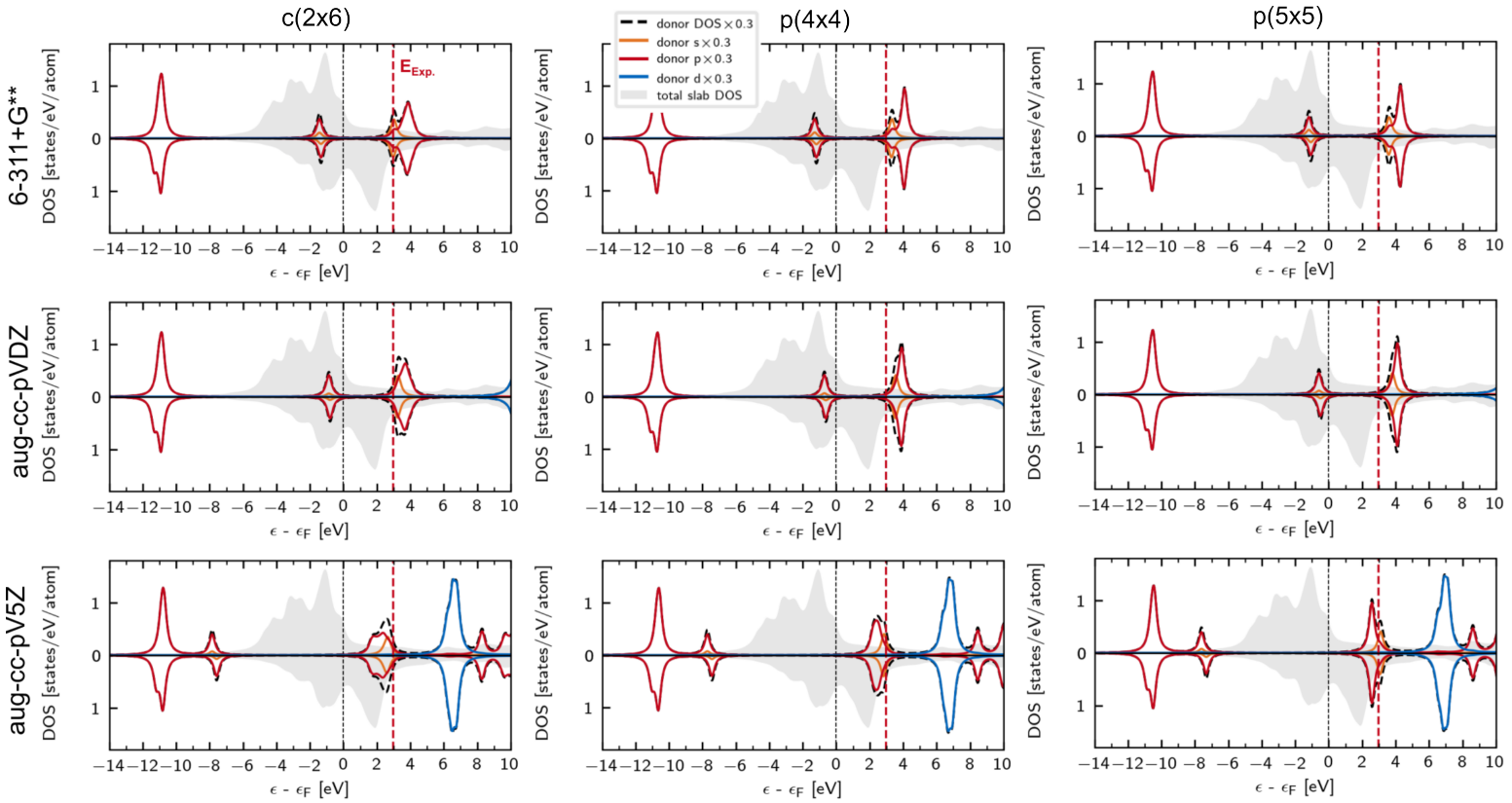

Figure A10: **Role of coverage and Argon basis.** Diabatic projected DOS for the ($POD2_d$,$frag_a$)GS scheme, Ar/Fe(110), for different coverages and Argon basis sets. The consistency of the diabatic properties with the adiabatic properties (e.g. Figure A11) varies with basis set and coverage. This Figure has been reused with permission from Reference [2] and has been submitted for publication. After it is published, it will be found at The Journal of Chemical Physics.

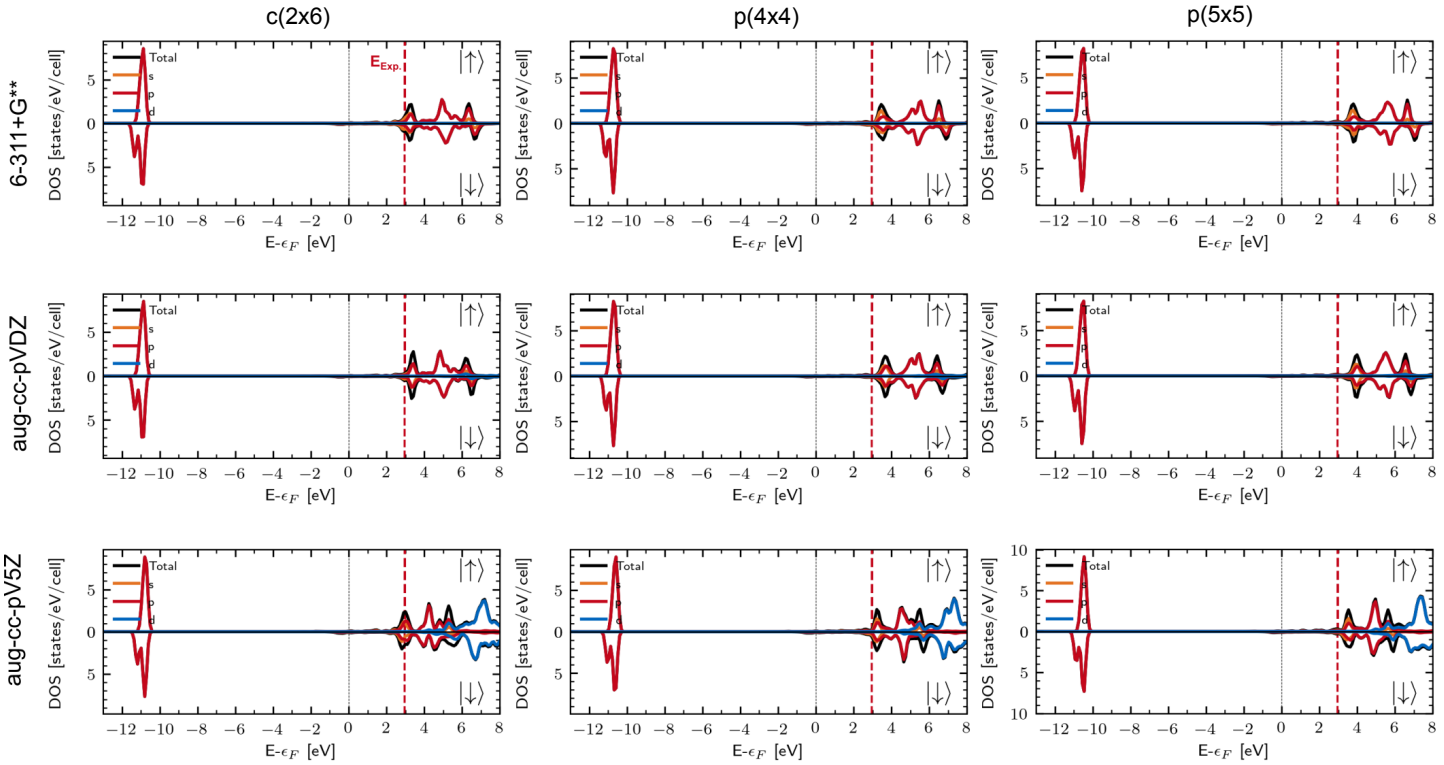

Figure A11: **Role of coverage and Argon basis.** Adiabatic (conventional) projected DOS of the Ar/Fe(110) system for different coverages and Argon basis sets, showing majority (spin up) and minority (spin down) channels. Compare to Figure A10. The energy of the 4s LUMO resonance, as well as the HOMO 3p states, is seen to increase upon reduction of coverage. This Figure has been reused with permission from Reference [2] and has been submitted for publication. After it is published, it will be found at The Journal of Chemical Physics.

Substrate Basis Set

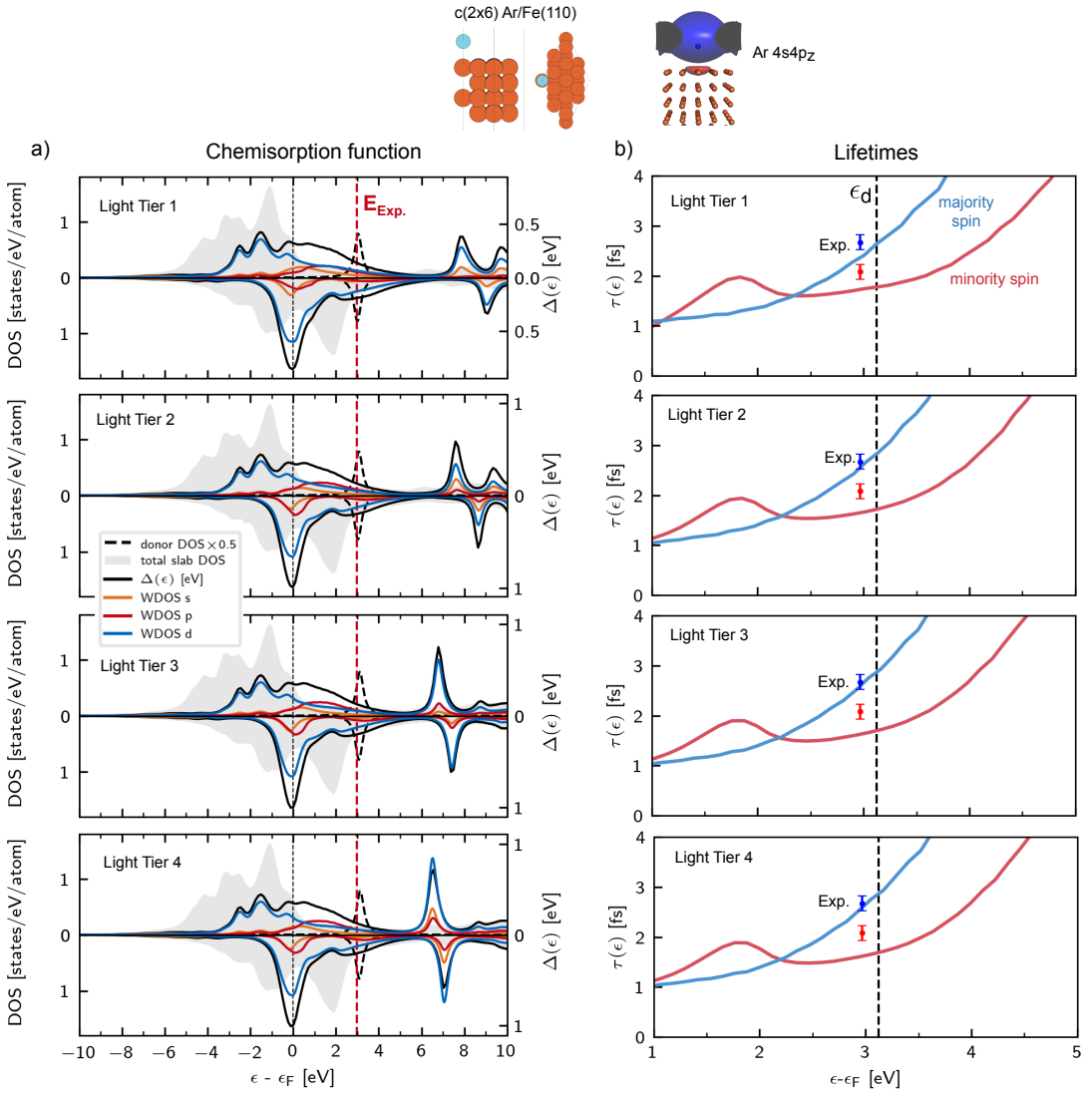

Figure A12: a) The influence of the substrate basis set on the chemisorption function of Ar/Fe(110) c(2x6) , using the ($POD2_d$,$frag_a$)GS method. Within the FHI-aims basis tier hierarchy, the basis set of the top metal layer is varied, while all deeper layers have default Light Tier 1. Upon the addition of tiers with increasingly diffuse basis functions, changes in the chemisorption function are only observed in the diffuse, high energy virtual states beyond the vacuum level (which is approx. 4.6 eV in the ground state). Coupling to states below the vacuum level are steady. b) The chemisorption function has been converted to an energy-dependent electron transfer lifetime, and compared to experimental lifetimes at the experimental resonance energy (shown with errorbars) [136]. The influence of the slab basis set is minimal. We choose Light Tier 4 as the production basis set for the uppermost metal layer. The k-grid is $12\times12\times1$ Monkhorst-Pack and the Argon basis set is 6-311+G**. This Figure has been reused with permission from Reference [2] and has been submitted for publication. After it is published, it will be found at The Journal of Chemical Physics.

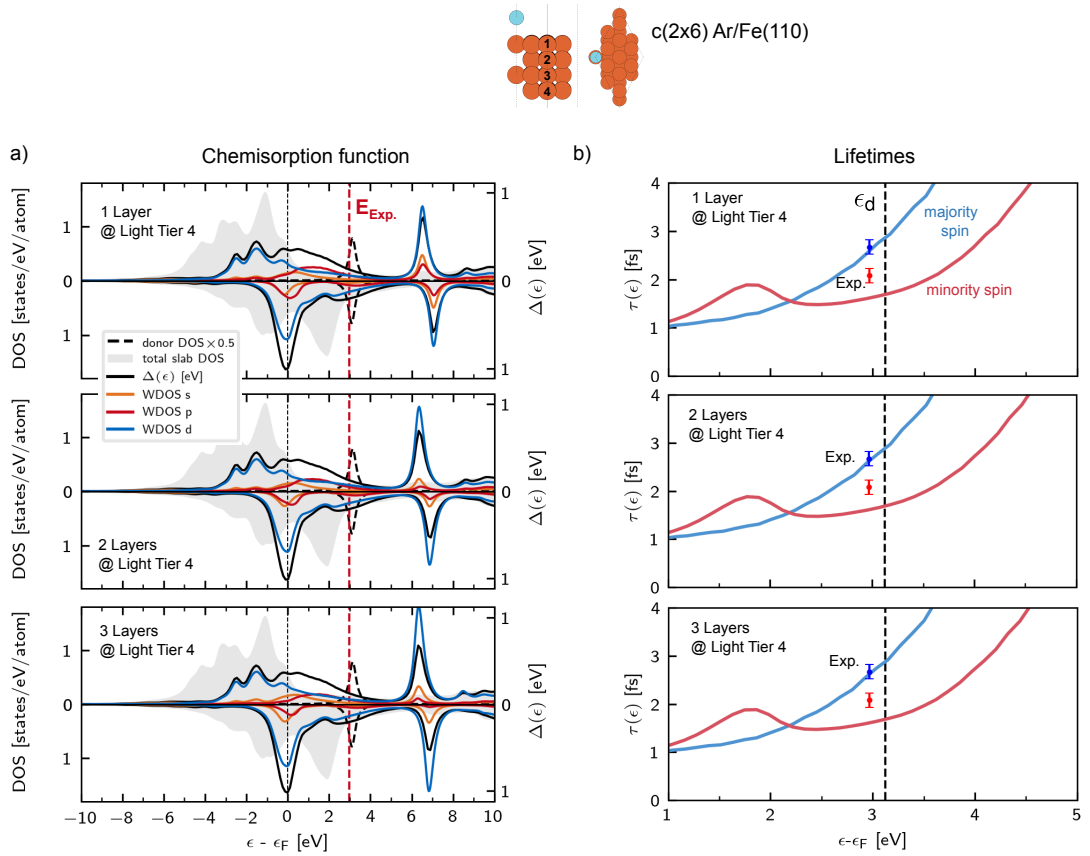

Figure A13: In a continuation of Figure A12, we demonstrate that it is sufficient to use the diffuse Light Tier 4 basis set in the uppermost metal layer and Light Tier 1 in all lower layers (top row). a) Changes in the chemisorption function are only observed at high energies. b) The influence on lifetimes at resonance is minimal, consistent with the basis functions of the bulk layers not significantly participating in the relevant wavefunction tails above the surface. This Figure has been reused with permission from Reference [2] and has been submitted for publication. After it is published, it will be found at The Journal of Chemical Physics.

A.4 Influence of Diabatization Scheme

It is appropriate to consider the non-uniqueness of the diabatic representation. Multiple suitable definitions of the diabatic states may exist. In the present context of charge transfer in Ar/metal systems, we may assess the suitability of a representation by considering the accuracy of the diabatic donor site energy, as well as the accuracy of the ET lifetimes compared to experiment. To assess the variation of results with the diabatization scheme employed, we compare the (frag_d,frag_a)GS and (POD2_d,frag_a)GS diabatization methods, as well as their counterparts without orthogonalization. The donor states of the two schemes are shown in Figure A14. We show in Figure A15 the BZ-averaged chemisorption function for the four different diabatization schemes for the Ar/Fe(110) system. The $\mathbf{k}$=Γ chemisorption functions are also shown for comparison. The resonance energy in the (frag_d,frag_a)GS scheme is underestimated, while that of (POD2_d,frag_a)GS agrees well with experiment. Orthogonal-

ization is seen to reduce the magnitude of couplings and the chemisorption functions. The ($frag_d$) is found to couple more strongly with the surface than the ($POD2_d$) donor, which has a p_z nodal structure. The hybridized nodal structure of POD2 donor is furthermore consistent with earlier works [27, 28]. The end result is that the $POD2_d$,$frag_a$)GS gives overall the most accurate donor site energies and ET lifetimes (Figure A16) when compared to the other methods. A summary of this analysis is provided in Table A5 for other slab systems. We thus identify the ($POD2_d$,$frag_a$)GS method in Figure A16 as the most suitable diabatization scheme for these systems.

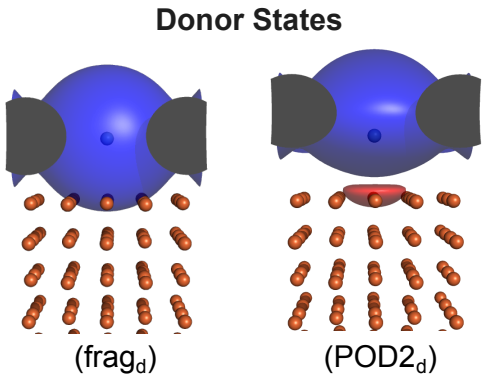

Figure A14: A comparison of Argon LUMO donor state models. In the fragment method, the donor is taken from an isolated monolayer and contains no interactions with the surface. Wavefunctions shown at isovalue 0.01 $e^{1/2}Å^{-3/2}$.

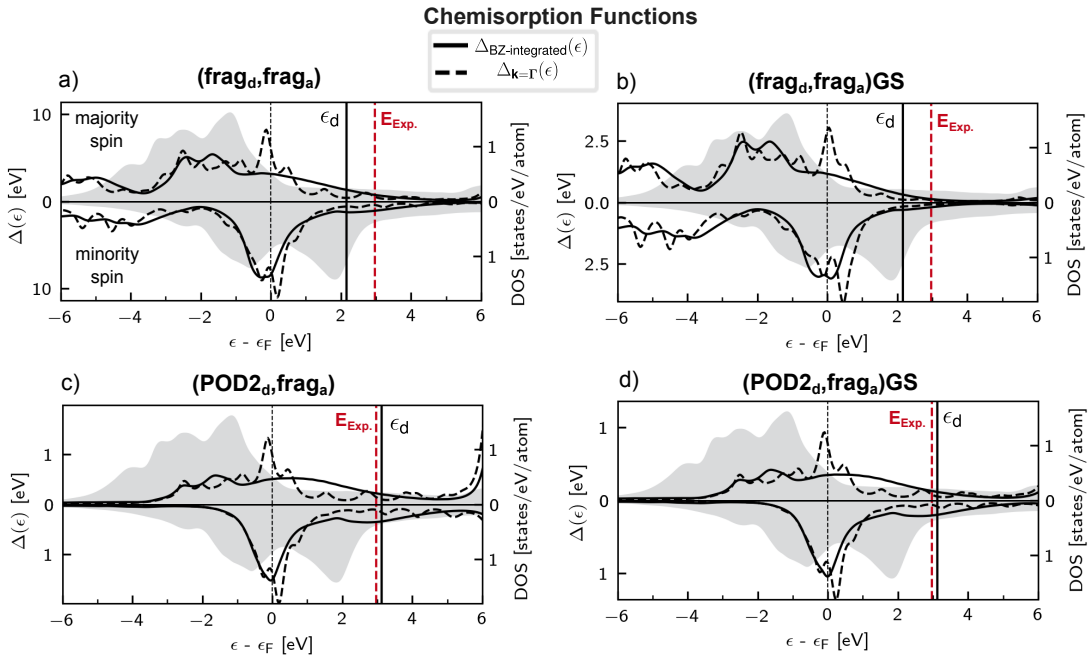

Figure A15: We show the chemisorption function from different diabatization schemes, at **k**=Γ (dashed black line) and BZ-integrated (solid black line). Two donor wavepackets are considered (shown in Figure A14 for **k**=Γ), and the acceptor states are used both with and without Gram-Schmidt orthogonalization. The system is the production Ar/Fe(110) slab with 8 layers. Different diabatization schemes yield significantly different chemisorption functions (see scale). The two donor wavepackets additionally have different site energies ϵ_d, while the acceptor DOS (grey) is practically unchanged. Orthogonalization of the diabats is seen to reduce the magnitude of the chemisorption function, while the donor wavepacket hybridization tunes both the magnitude and contour of the chemisorption function. This Figure has been reused with permission from Reference [2] and has been submitted for publication. After it is published, it will be found at The Journal of Chemical Physics.

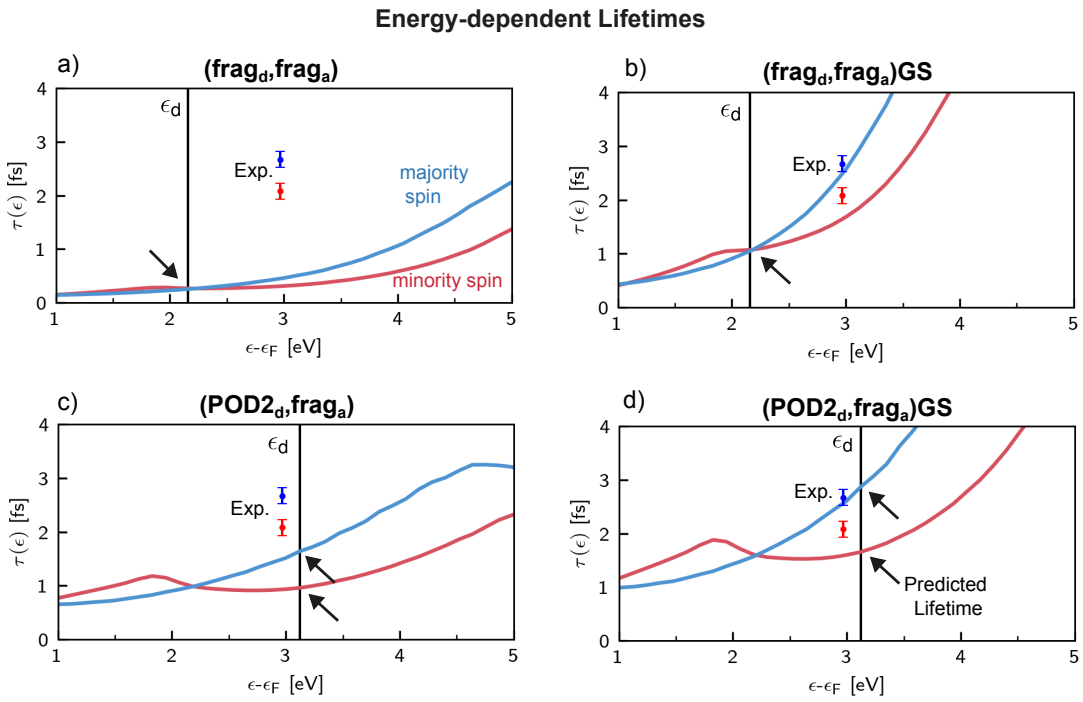

Figure A16: The energy-dependent lifetimes (BZ-integrated) are compared for the different diabatization schemes, for the c(2×6) Ar/Fe(110) production system. Experimental lifetimes, with errobars, are shown at the experimental resonance energy. Predicted lifetimes at the predicted resonance energy ϵ_d are indicated with arrows. The (POD2$_d$,frag$_a$)GS method is identified as the most suitable diabatization method and used throughout this work. Extracted lifetimes are listed in Table A5. This Figure has been reused with permission from Reference [2] and has been submitted for publication. After it is published, it will be found at The Journal of Chemical Physics.

Table A5: Lifetimes (in femtoseconds) from different diabatization schemes, for the production systems of Table 4.2. For comparison purposes, all lifetimes have been evaluated at the resonance energy of the ($POD2_d$) donor state (shown also in Table 4.2). Occasionally (e.g. on Fe), lifetimes evaluated at **k=**Γ agree well with experiment. This is fortituous, as these are vulnerable to finite size effects and thus not suitable for interpretation (see Figure A3). This table has been reused with permission from Reference [2] and has been submitted for publication. After it is published, it will be found at The Journal of Chemical Physics.

	k=Γ		**BZ-averaged**	
	$\tau_{\mathbf{maj.}}$	$\tau_{\mathbf{min.}}$	$\tau_{\mathbf{maj.}}$	$\tau_{\mathbf{min.}}$
Ar/Fe(110)				
($frag_d$,$frag_a$)	0.97	0.57	0.51	0.32
($frag_d$,$frag_a$)GS	4.81	3.66	2.97	1.86
($POD2_d$,$frag_a$)	3.34	2.02	1.64	0.96
($POD2_d$,$frag_a$)GS	6.3	3.8	2.88	1.66
Experiment. [136]			2.67	2.08
Ar/Co(0001)				
($frag_d$,$frag_a$)	1.44	0.82	0.53	0.39
($frag_d$,$frag_a$)GS	5.41	4.19	2.43	1.78
($POD2_d$,$frag_a$)	5.39	3.01	1.97	1.35
($POD2_d$,$frag_a$)GS	9.62	5.42	3.15	2.14
Experiment. [136]			3.24	2.63
Ar/Ni(111)				
($frag_d$,$frag_a$)	1.1	1.4	0.59	0.52
($frag_d$,$frag_a$)GS	5.38	5.05	2.77	2.46
($POD2_d$,$frag_a$)	3.52	5.09	2.12	1.82
($POD2_d$,$frag_a$)GS	6.67	9.01	3.43	2.93
Experiment. [136]			3.12	3.12
Ar/Ru(0001)				
($frag_d$,$frag_a$)	1.43	1.44	0.33	0.33
($frag_d$,$frag_a$)GS	4.02	4.04	1.36	1.37
($POD2_d$,$frag_a$)	5.81	5.8	0.87	0.87
($POD2_d$,$frag_a$)GS	9.41	9.4	1.41	1.41
Experiment. [79]			1.5	1.5
Ar/Pt(111)				
($frag_d$,$frag_a$)	1.91	1.92	0.71	0.71
($frag_d$,$frag_a$)GS	4.86	4.89	2.05	2.06
($POD2_d$,$frag_a$)	7.45	7.43	2.22	2.22
($POD2_d$,$frag_a$)GS	11.29	11.26	3.14	3.13
Experiment. [137]			3.51	3.51

B Analysis of Electronic Couplings in Ar/Fe(110)

We discuss in more detail the electronic couplings in the Ar/Fe(110) system shown in Figure 4.12.

Mulliken Character versus H_{ad}

The angular momentum decomposition of the chemisorption function (the pWDOS) reveals the average character of states participating in the WDOS. It does not, however, reveal which character is associated with a strong *coupling*. For a more thorough analysis of this, in Figures B1-B2 we show correlation plots of the $H_{ad,\mathbf{k}}$ against the Mulliken character of the acceptor states, for the Ar4s4p$_z$/Fe(110) production system.

As was already clear from Figure 4.12, the relationship between the character of acceptor states and their coupling to the adsorbate is nontrivial due to the complex and local nature of the phase effects.

It would be desirable to formally decompose the couplings into contributions from different basis functions of the surface. However, while the Mulliken character is only moderately ambiguous (due to basis function overlaps), the electronic coupling is much less suitable for decomposition. The electronic coupling is a pairwise interaction, consisting of off-diagonal terms while the Mulliken character is dominated by local on-site terms which are easier to seperate.

It is nevertheless reasonable to ask which character of a state is responsible for the strength of its coupling. An otherwise forbidden transition may suddenly become allowed upon e.g. slight hybridization of the final state's character. In this way, it is possible that the coupling strength may be dominated by even the weakest components of a state's overall Mulliken character. We relegate this inquiry to future work.

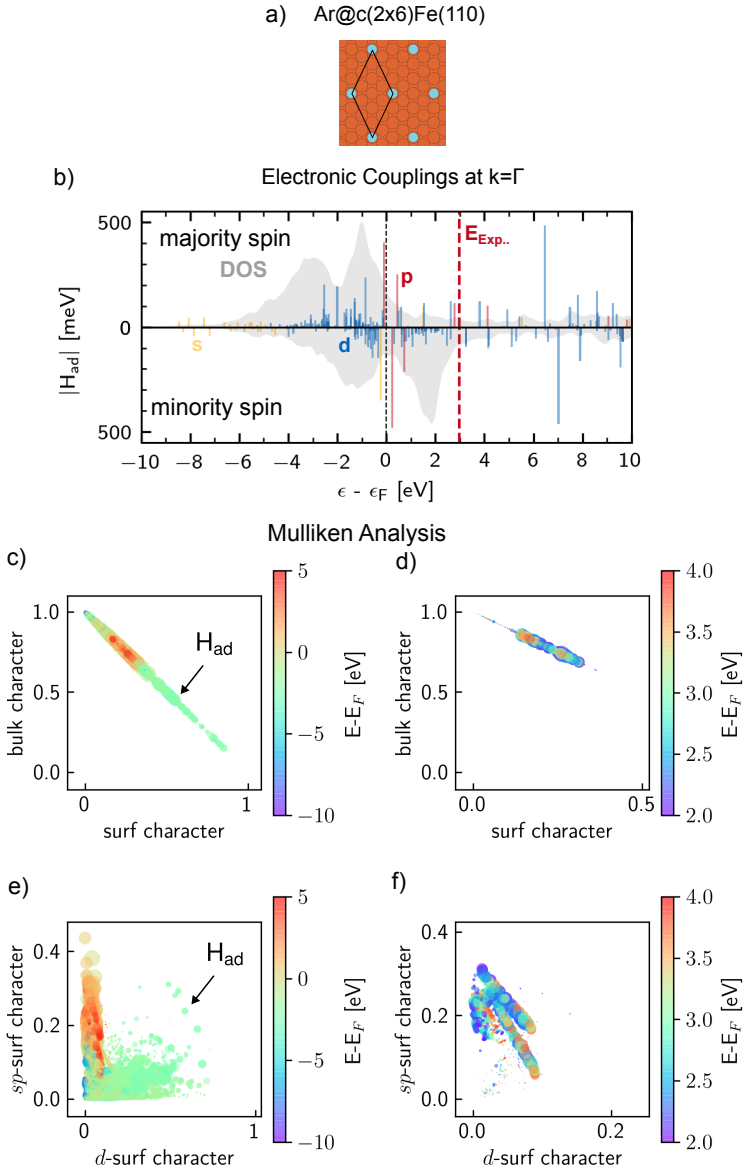

Figure B1: The electronic couplings for the Ar/Fe(110) system are analyzed in terms of the Mulliken character of the associated acceptor state. a) The overlayer model (See also Figure 4.11) b) The couplings at **k** = Γ, color-coded according to the dominant Mulliken character of the state. The Mulliken character M_μ of a state is defined in Equation (3.43). c)-d) The couplings are plotted in terms of the character of the acceptor state on the surface layer versus in the bulk, c) for all states and d) those near the resonance. Marker size corresponds to coupling strength. e)-f) The couplings are shown in terms of the *sp* versus *d*-character of the acceptor states in the surface layer. The higher energy states are seen to have more *sp*-character as anticipated. Strong couplings (large dots) are observed over a range of characters. The system is the production slab of c(2x6)Ar/Fe(110). c)-f) show couplings for all of the acceptor states of the majority spin channel which lie in the energy window indicated, and include couplings from the full Brillouin zone (12x12x1 k-grid).

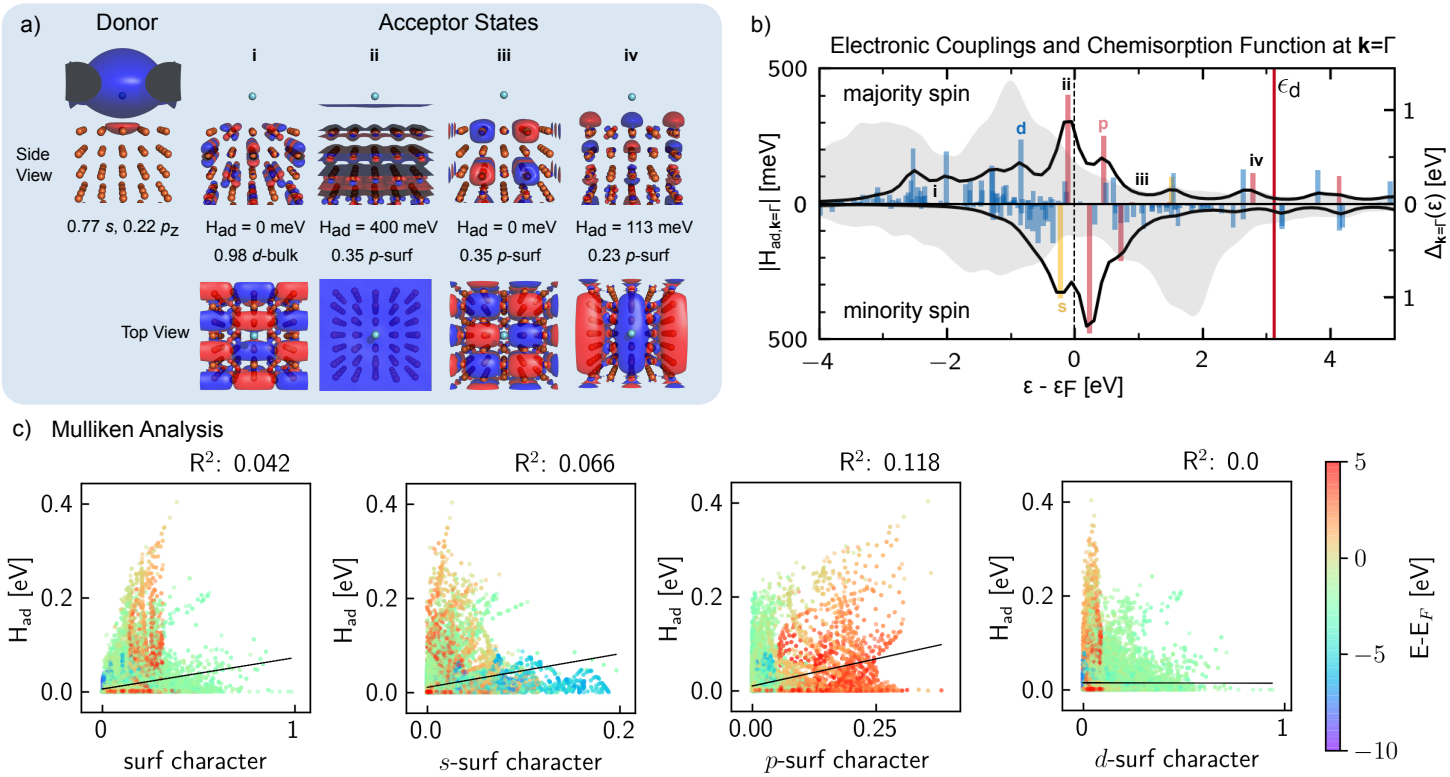

Figure B2: We analyze in more detail Figure 4.12. a) and b) show the electronic couplings for Ar/Fe(110) at k=Γ. c) The electronic couplings of the system are analyzed in terms of the Mulliken character of the associated acceptor state. Due to symmetry and phase effects, couplings are not trivially correlated with the Mulliken character of participating states, or even with the presence of states on the surface versus bulk layers. The Mulliken character is defined in Equation (3.43). Linear regression shown for illustration only. Couplings in c) are shown for the majority-spin channel and are taken from the full Brillouin zone (12x12x1 k-grid).

Role of Orthogonalization

As shown in Figure B3, the electronic couplings under the ($frag_a$,$POD2_d$)GS scheme are slightly reduced in magnitude from those of the ($frag_a$,$POD2_d$) scheme. The effective (orthogonalized) couplings of ($frag_a$,$POD2_d$)GS show a linear relationship to the overlap of the pre-effective ($frag_a$,$POD2_d$) couplings. This relationship has been recognized for molecular systems and exploited in the efficient Analytic Overlap Method [145] to estimate couplings.

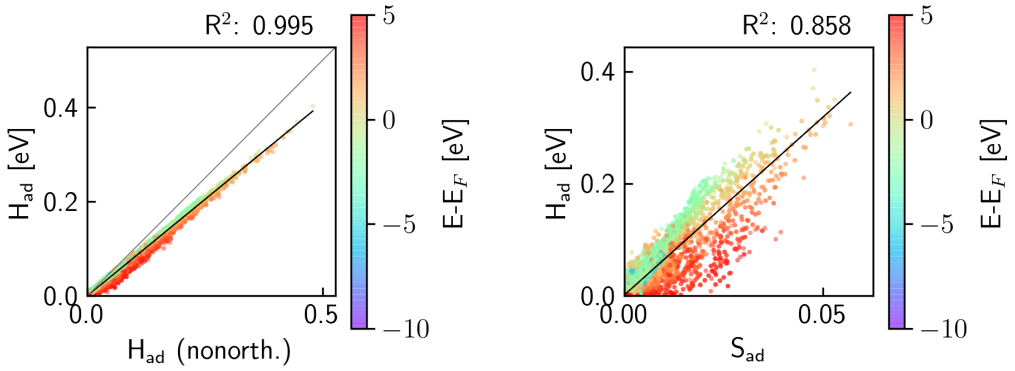

(a) (b)

Figure B3: The effective couplings are compared to the pre-effective couplings and to the overlap. a) Orthogonalization is seen to slightly reduce the magnitude of the couplings. b) The effective electronic couplings H_{ad} (after orthogonalization) are compared to the overlap S_{ad} of the donor-acceptor pairs prior to the orthogonalization. Data are shown for all electronic couplings in the energy range indicated, throughout the 74 points of the 12x12x1 Monkhorst-Pack k-grid in the Brillouin zone, for majority spin direction of the Ar/Fe(110) production system of Figure 4.12. The ($frag_a$,$POD2_d$)GS method is used. Linear regression is shown for illustration.

Couplings in k-space

The variation of the acceptor state nodal structure throughout the Brillouin zone is significant, resulting in anisotropy of the electronic couplings. This explains the need to properly sample the Brillouin zone to achieve an accurate and converged estimate of adsorbate broadening with the chemisorption function. Figure B4 shows for example the large differences in the chemisorption function at two k-points. Using a logarithmic scale, it is more clearly seen how most states have vanishing couplings, leaving the WDOS to be determined by a handful of dominant states at each **k**-point.

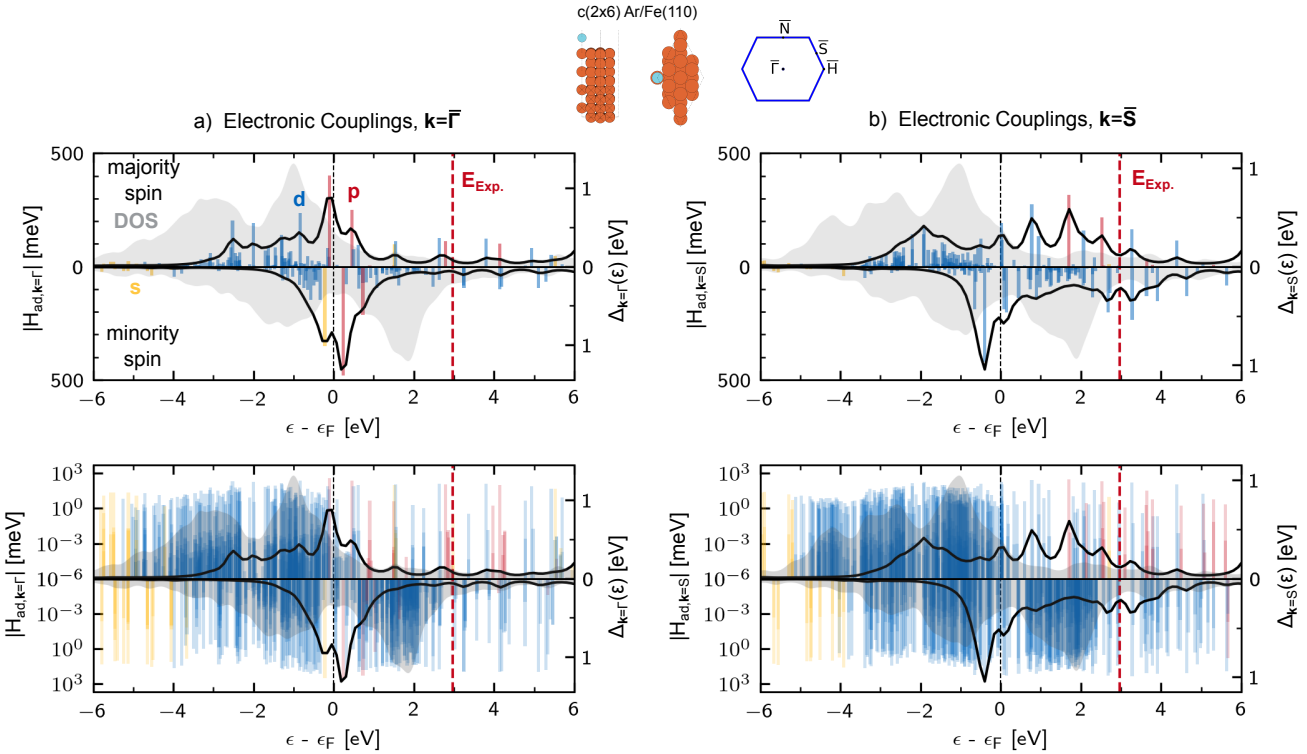

Figure B4: The electronic couplings and chemisorption functions shown at two different **k**-points for the 8-layer, c(2x6) Ar/Fe(110) system of Figure 4.12. Couplings are shown on an absolute scale (upper) and logarithmic scale (lower), and are colored according to the dominant Mulliken character of the acceptor states. Near the resonance, significant couplings are found for both *p* and *d*-like acceptor states. In contrast, the PDOS is dominated by the *p*-channel (e.g. Figure C4) at resonance. These **k**-resolved chemisorption functions are included in the BZ-averaged chemisorption function shown Figure 4.13. The variation in the chemisorption function over the BZ is shown also in Figure C10, demonstrating the need for Brillouin zone integration. The ($POD2_d$,$frag_a$)GS method is used. This Figure has been reused with permission from Reference [2] and has been submitted for publication. After it is published, it will be found at The Journal of Chemical Physics.

C Extended Results: Argon on Transition Metals

Parts of the following section have been reused with permission from Reference [2] and have been submitted for publication. After they are published, they will be found at The Journal of Chemical Physics.

We provide in Figures C1 and C2 further correlation of lifetimes with properties of the surfaces, e.g. those in Table C1. Figures C3- C11 show the diabatic description of Ar on all surface systems studied. In addition, we compare the chemisorption functions of the ($POD2_d$,$frag_a$)GS and ($frag_d$,$frag_a$)GS schemes, which have different donor states. While the schemes offer similar lifetimes near the experimental resonance (Figure C7), the use of a ($frag_d$) donor leads to underestimation of the resonance energy ϵ_d (Figure C5).

Table C1: Parameters describing the electronic structure of the substrates. The *sp*-bandgap onset is determined from the adiabatic bandstructures of the primitive surface cells in Figure E3. The *d*-band center of mass is determined by analyzing the DOS of the surface layer, shown in e.g. Figure C5. A cutoff of 0.2 [states/eV/atom] was used to define the edges of the *d*-band. This also defines the upper edge listed in the table. Values are in eV with respect to Fermi energy. Values are shown in Figure C4. This table has been reused with permission from Reference [2] and has been submitted for publication. After it is published, it will be found at The Journal of Chemical Physics.

	***d*-band center**		***d*-band edge**		***sp*-bandgap onset**	
	majority	minority	majority	minority	majority	minority
Fe(110) BCC	-2.03	0.46	0.32	3.09	0.73	2.9
Co(0001) HCP	-2.32	-0.64	-0.07	2.06	0.17	1.11
Ni(111) FCC	-1.87	-1.2	0.2	1.15	0.42	0.53
Ru(0001) HCP	-1.65		2.1		1.025	
Pt(111) FCC	-2.25		0.83		0.21	

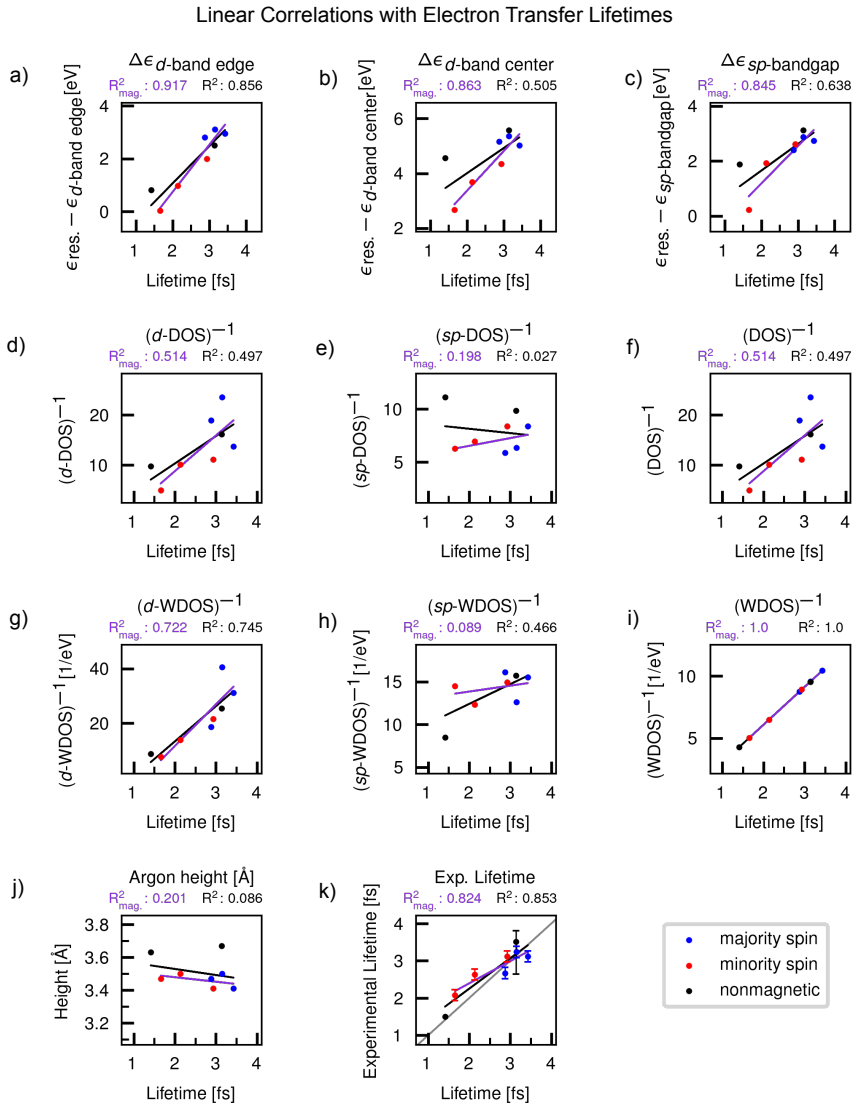

Figure C1: We explore the relationship of the predicted electron transfer lifetimes to the properties of the systems, extending Figure 4.15. Linear regressions are performed for illustration of trends, for all datapoints (black) and for the magnetic systems only (violet). R^2 values are indicated to show the strength of linear correlations. A linear correlation cannot in all cases be expected, as we compare different substrates, but is shown for illustration purposes. a)-c) Scaling of the lifetimes with the level alignments of the surface bands. The d-band edge and center of mass are defined with a cutoff of 0.2 [N/eV/atom] observing the projected d-channel of the surface DOS in Figure C4. d)-f) Scaling of the lifetimes with the inverse of the DOS. g)-i) Scaling of lifetimes with the inverse of the chemisorption function (WDOS). j) Scaling of lifetimes with Argon adsorption height. k) Scaling of (predicted) lifetimes with the experimental values, shown with errorbars when reported. Mean relative signed error is -6%. Electronic structures are shown in Figures C3 and C4. This Figure has been reused with permission from Reference [2] and has been submitted for publication. After it is published, it will be found at The Journal of Chemical Physics.

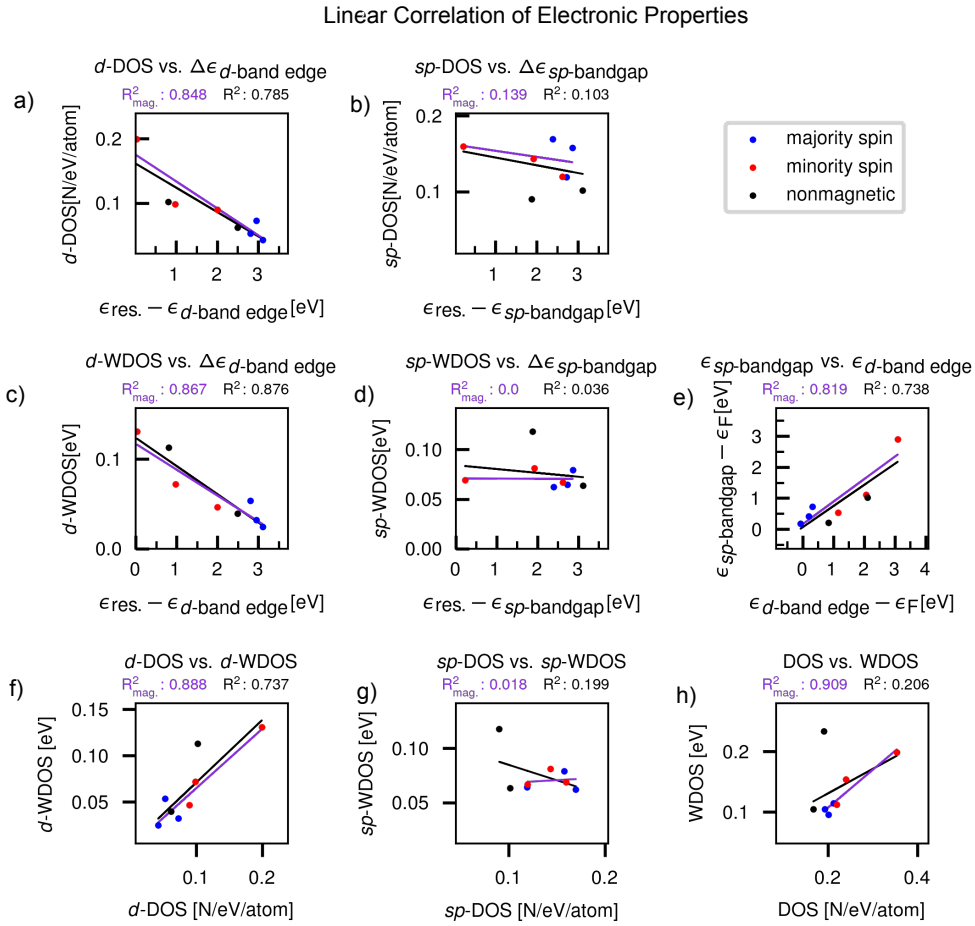

Figure C2: Predicted electron transfer lifetimes are tested for correlations, extending Figure 4.15. A linear correlation cannot in all cases be expected, as we compare different substrates, but is shown for illustration purposes. a) The proximity of the d-band edge to the resonance is associated with increased d-band DOS at resonance. b) The proximity of the sp-band gap onset to the resonance is not associated with any change in the sp-band DOS at resonance (consistent with constant DOS for 2D parabolic bands). c) The proximity of the d-band edge to the resonance is associated with increased WDOS *d*-channel. d) The proximity of the *sp*-band gap onset to the resonance is not associated with change in the WDOS *sp*-channel. e) The *sp*-band gap onset energy and the *d*-band edge are shown to be closely related. f) The *d*-channel of the DOS and WDOS show a strong linear scaling (stronger for magnets), indicating a trivial phase relationship. g) The *sp*-channel of the DOS and WDOS show no scaling, indicating a nontrivial phase effect. h) The DOS and WDOS show a strong linear scaling for magnetic systems (which have similar atomic number) indicating an overall trivial phase effect, and poor linear scaling upon consideration of all systems. This is consistent with spin-selectivity being determined simply by the DOS - specifically by the *d*-band component. Electronic structures are shown in Figures C3 and C4. This Figure has been reused with permission from Reference [2] and has been submitted for publication. After it is published, it will be found at The Journal of Chemical Physics.

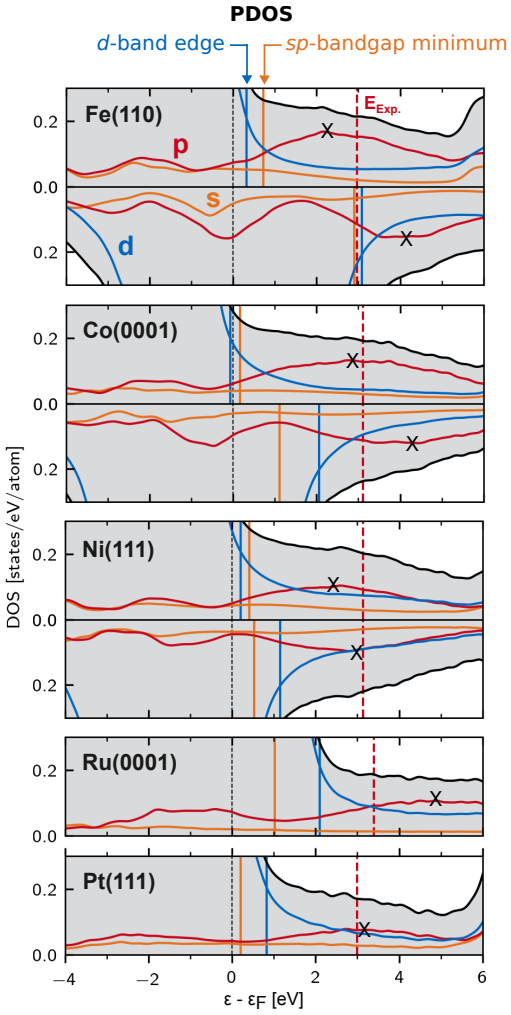

Figure C3: The diabatic projected density of states (PDOS) of the slabs, under the ($POD2_d$,$frag_a$)GS method. Compare to Figure C4. This Figure has been reused with permission from Reference [2] and has been submitted for publication. After it is published, it will be found at The Journal of Chemical Physics.

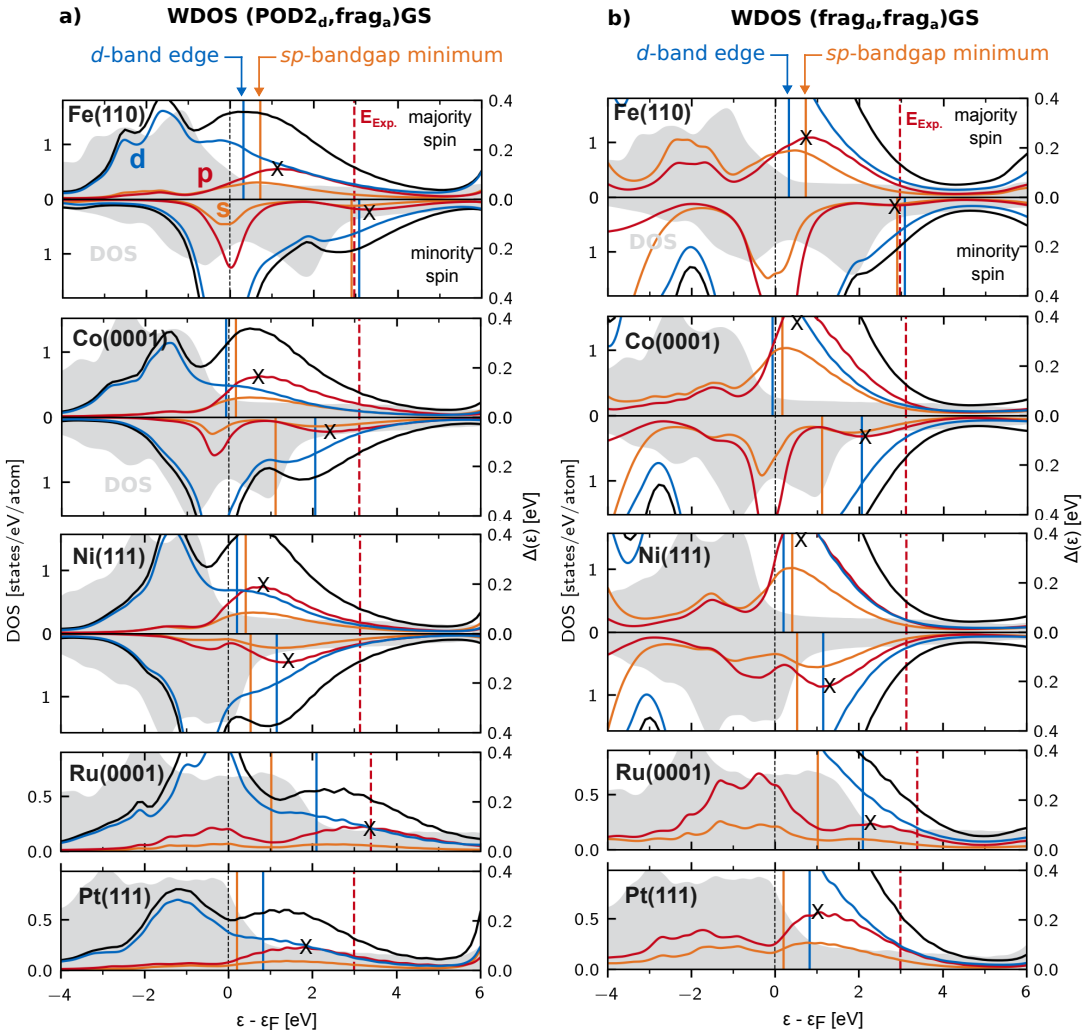

Figure C4: The WDOS is shown for two diabatic models: a) (POD2$_d$,frag$_a$)GS with a hybridized 4s4p_z donor and b) (frag$_d$,frag$_a$)GS with a constrained 4s donor. The methods are also compared in Figure C5, and the decompositions are defined in Equations (3.47) and (3.50). The complex relationship between the DOS (Figure C3) and WDOS can be understood in terms of the nature of the electronic couplings. In both of the donor models, the d-channel shows generally a more linear relationship between the DOS and WDOS above the Fermi level, while this relationship is nontrivial in the sp-channel. The behavior is consistent with more severe phase effects in coupling to the spatially more extensive sp-like states compared to the more compact d-like states, a behavior which in turn is understood from e.g. Chen's rules in STM [50]. Previous work has described the decay of electronic couplings with $\mathbf{k}_{||}$ in the sp-band gap region. The sp-bandgap onset (taken from primitive band structures, Figure E3 is shown as a vertical orange line. This is found to be associated with a local maximum (marked with an X) and subsequent downturn in the s and p-channels of the chemisorption functions. The behavior is consistent with the proposed effect of the band gap, although a rigorous analysis of the $\mathbf{k}$-dependence of couplings will be saved for future work. Both d and p components are found to contribute significantly to the downward slope of the chemisorption function at resonance and hence to the energy-dependence of ET lifetimes. This Figure has been reused with permission from Reference [2] and has been submitted for publication. After it is published, it will be found at The Journal of Chemical Physics.

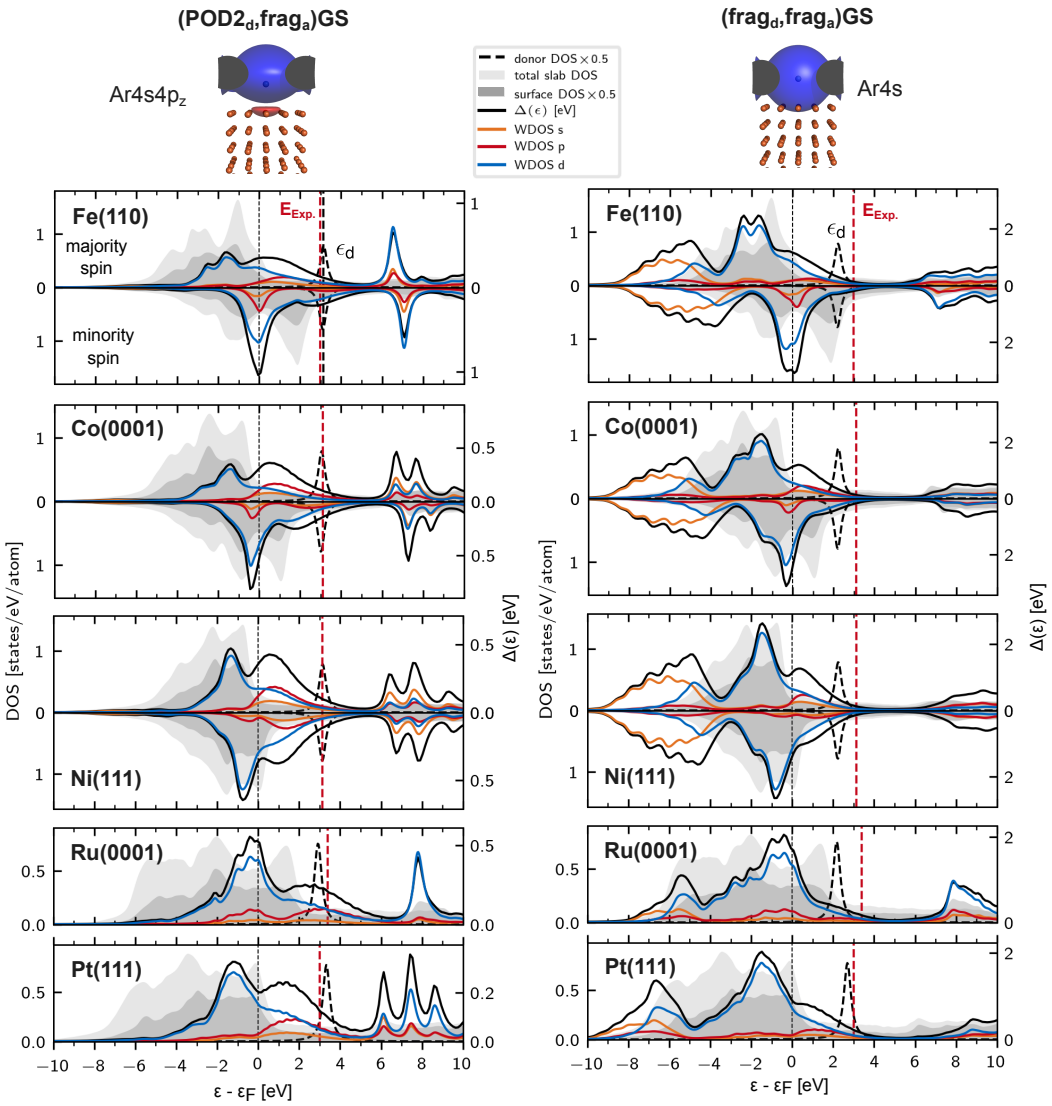

Figure C5: a) The chemisorption function of the (POD2$_d$,frag$_a$)GS method is compared to that of the constrained 4s (frag$_d$,frag$_a$)GS method in b). The WDOS of the constrained 4s-donor state shows a closer tracking of the d-band DOS, which is anticipated in e.g. Tersoff-Hamann [47] and Chen's [50] STM theory for the coupling of *s*-like versus *p*-like probe states on surfaces. The difference between the DOS and WDOS remains significant and nontrivial, however, in both methods. A significant difference is also seen in the energy of the donor state (shown as a PDOS peak), which is underestimated in the (frag$_d$) approach. The angular momentum decomposition of the WDOS is shown, and reveals that the donor wavepacket hybridization primarily affects couplings to the *d*-type states of the surface, while couplings near the resonance are relatively unchanged. The hybridized and constrained donor wavepackets from the Ar/Fe(110) system are shown on top. See also Figure C4. This Figure has been reused with permission from Reference [2] and has been submitted for publication. After it is published, it will be found at The Journal of Chemical Physics.

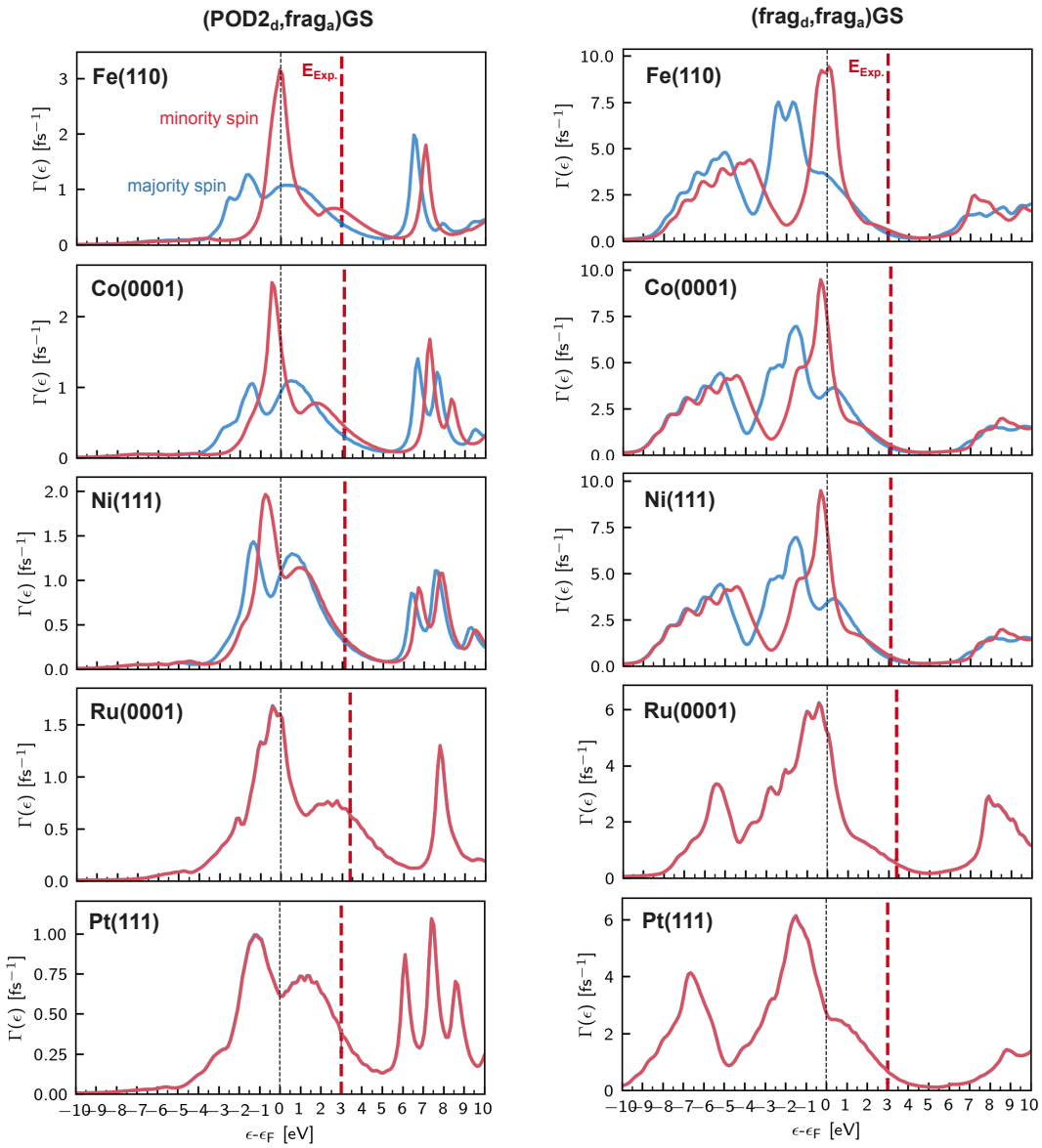

Figure C6: The chemisorption function of Figure C5 is shown as a spin-dependent electron transfer rate for the 5 surfaces, comparing the ($POD2_d$,$frag_a$)GS (left) and the ($frag_d$,$frag_a$)GS (right) approaches. The experimental resonance energy is shown as a vertical red line. While constraining the donor wavepacket to the 4s state of the isolated monolayer (right) does change the chemisorption function significantly overall, the ET rates near the resonance are only modestly affected. The robustness of the ET rates with respect to the wavepacket hybridization was also observed previously [27]. In Figure C5, we see that the wavepacket hybridization changes primarily couplings to the d-band, with a smaller effect on couplings near resonance. A more significant difference is observed in the site energy of the donor state. This Figure has been reused with permission from Reference [2] and has been submitted for publication. After it is published, it will be found at The Journal of Chemical Physics.

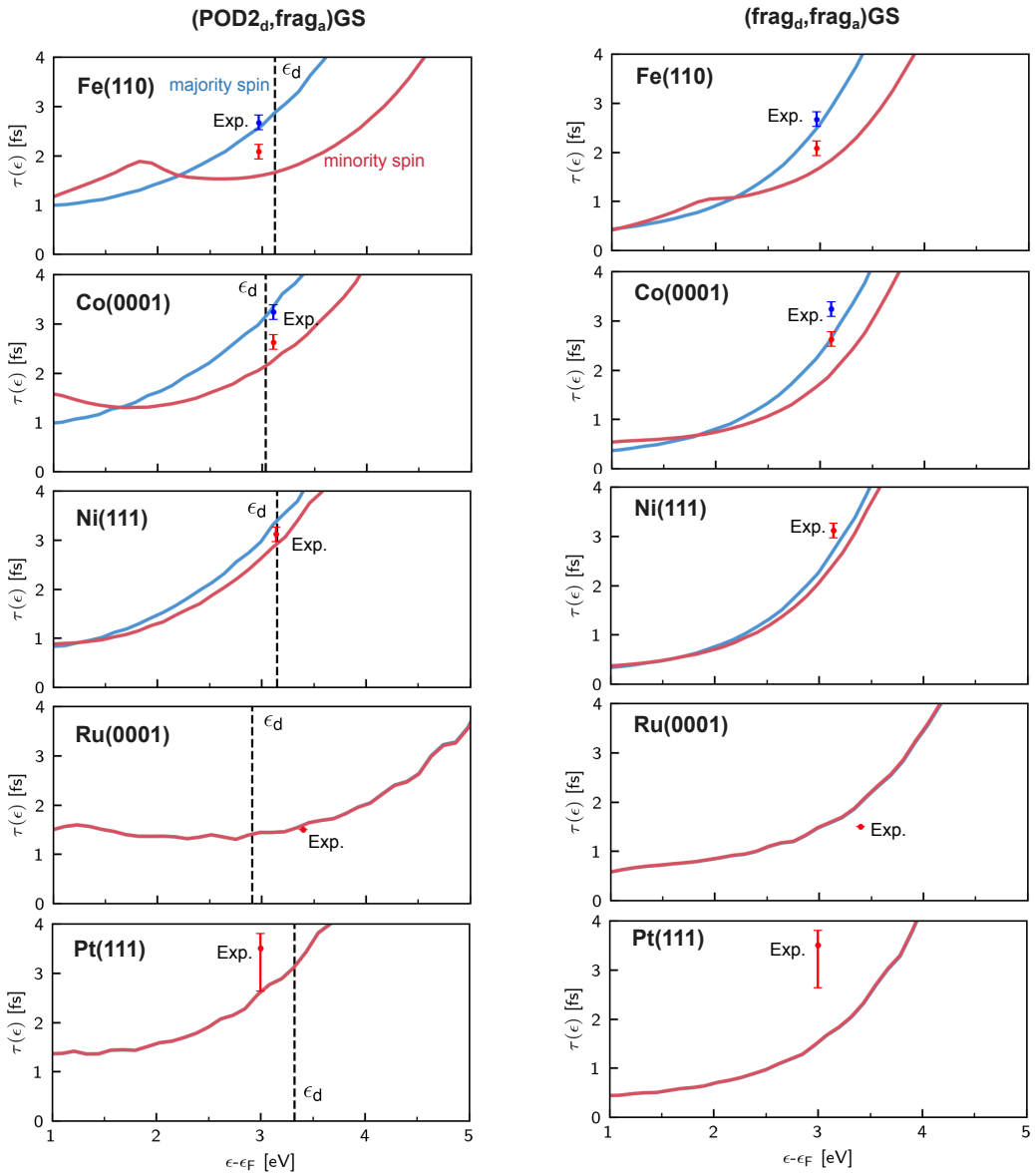

Figure C7: The chemisorption function of Figure C5 is shown as an energy-dependent electron transfer lifetime for the 5 surfaces, comparing the (POD2$_d$,frag$_a$)GS (left) and the (frag$_d$,frag$_a$)GS (right) approaches. The lifetimes reported in this work are the values at the predicted resonance energy: $\tau = \tau(\epsilon_d)$. The experimental lifetimes are shown at the experimental resonance energy (with errorbars when reported). While constraining the donor wavepacket to the 4s state of the isolated monolayer does change the chemisorption function significantly overall, predicted ET lifetimes near the resonance are less affected. The independence of lifetimes to the wavepacket hybridization was also found in an earlier work [27]. A more significant difference is observed in the predicted site energy of the donor state ϵ_d, which is underestimated in the (frag$_d$,frag$_a$)GS method (shown in Figure C5). This Figure has been reused with permission from Reference [2] and has been submitted for publication. After it is published, it will be found at The Journal of Chemical Physics.

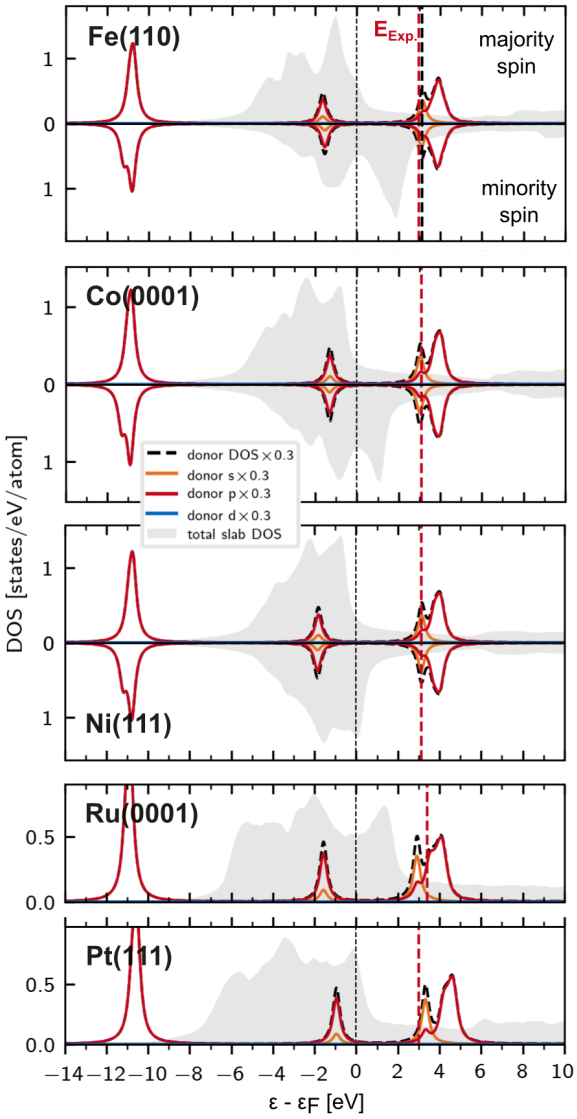

Figure C8: The (POD2$_d$,frag$_a$)GS diabatic DOS of the slab (grey), and the diabatic DOS of the Argon adsorbate. The angular-momentum components of the Argon DOS are shown in colors. A hybridized $4s4p_z$ resonance state (see yellow *s*-channel) is found in good agreement with the experimental resonance energy on all slabs (red dashed line). The donor state is distinguished from nearby $4p$ states through a Mulliken analysis at each **k**-point. A ghost artifact $4p_z$ state is visible below the Fermi level (described in text), and the $3p$ HOMO peaks are visible as anticipated near -13eV. The spectra here are comparable to the adiabatic PDOS in Figure E1, with the exception of the artifact state. This Figure has been reused with permission from Reference [2] and has been submitted for publication. After it is published, it will be found at The Journal of Chemical Physics.

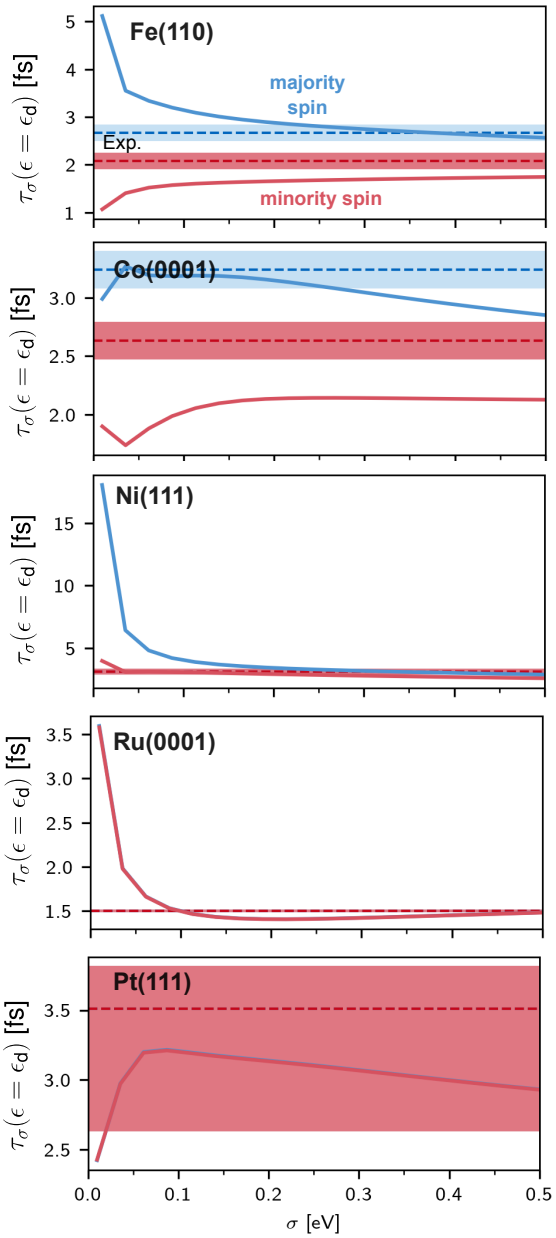

Figure C9: The stability of electron transfer lifetimes with respect to the Lorentzian broadening parameter σ of the chemisorption function. The lifetimes are taken from the value of the chemisorption functions of Figure C6a at the predicted resonance energies of Table 4.2. Experimental ET lifetimes are shown as horizontal dashed lines, with shaded regions indicating experimental errorbars (when reported). We report ET lifetimes at the broadening value of σ=0.2eV. The chemisorption function (WDOS), like the DOS, requires a finite broadening for smoothe behavior, the value of which is also related to the density of the k-grid used (here, 12x12x1 for all slabs). This Figure has been reused with permission from Reference [2] and has been submitted for publication. After it is published, it will be found at The Journal of Chemical Physics.

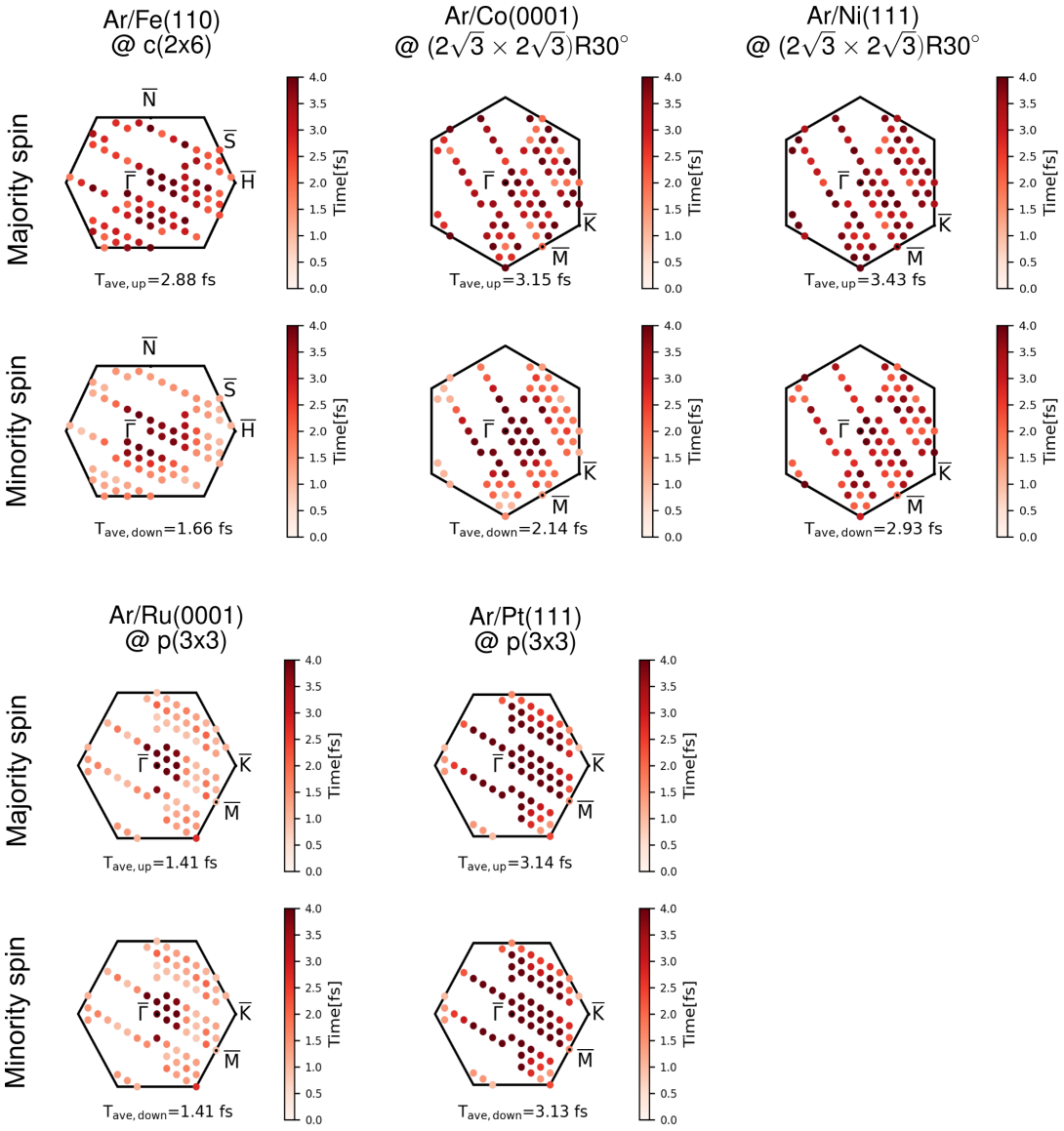

Figure C10: The ET lifetimes at resonance, $\tau(\epsilon = \epsilon_d)$, as they are calculated throughout the irreducible surface Brillouin zones of the overlayers on the 12×12×1 Monkhorst-Pack grid. The BZ-averaged lifetimes, given in Table 4.2, are thus averaged over these points. The onset of the parabolic surface-projected band gap is visible for Ru and Pt, despite the presence of folded bands. The (POD2$_d$,frag$_a$)GS method is used. The significant variation of couplings over the BZ is shown also in Figure B4. This Figure has been reused with permission from Reference [2] and has been submitted for publication. After it is published, it will be found at The Journal of Chemical Physics.

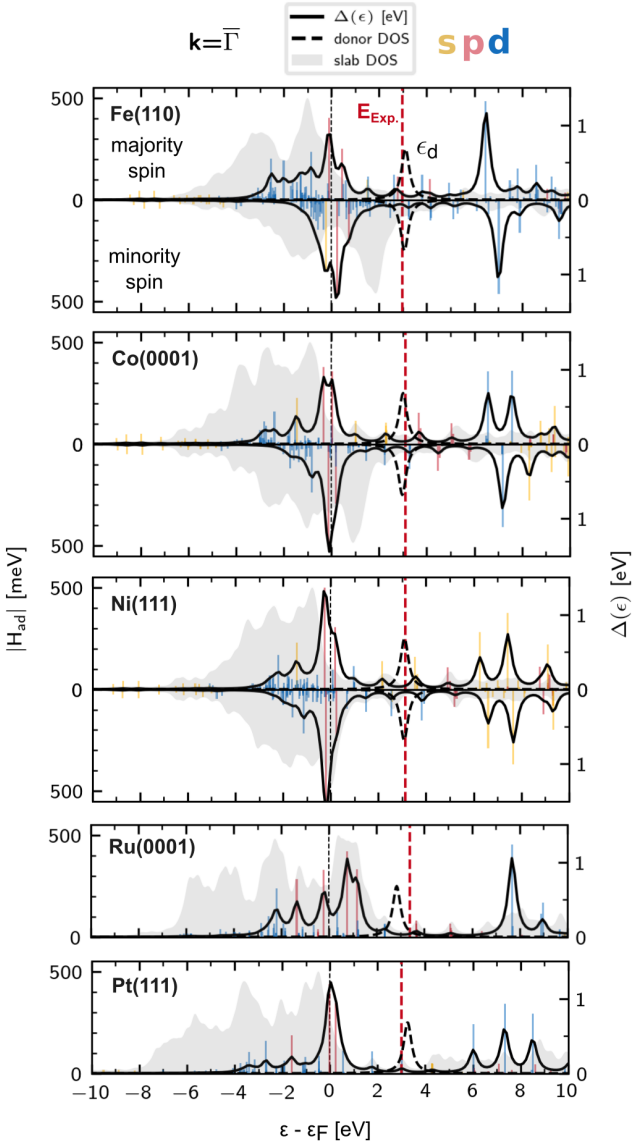

Figure C11: Electronic couplings and chemisorption function at $\mathbf{k}_{||} = \Gamma$ for all systems, using the (POD2$_d$,frag$_a$)GS method. The dominating angular momentum character of the surface states is indicated in color. The projected diabatic DOS of the donor resonance state is shown as a black dashed line, in good agreement with the experimental resonance energy (red vertical line). The diabatic DOS of the slab, at $\mathbf{k}_{||} = \Gamma$, is shown in grey. This Figure has been reused with permission from Reference [2] and has been submitted for publication. After it is published, it will be found at The Journal of Chemical Physics.

D Wavepacket Models in k-space and Real-space

In Figure D1, we show the effect of different Gaussian wavepacket models on ET lifetimes. The system is our production slab c(2x6) Ar/Fe(110) with 8 layers of depth. The cells of the overlayer and primitive lattice are shown in real-space, and the nested Brillouin zones of Argon and Fe are shown in reciprocal space. On the left is shown a broad 2D Gaussian in real-space. This has a standard deviation of σ_r=5Å, shown as a dashed line, resulting in a narrow wavepacket in k-space (The Fourier transform of the Gaussian is another Gaussian with standard deviation $\sigma_k \sigma_x \geq \frac{1}{2}$). The preferential weighting of the **k**=Γ region increases the ET lifetimes. On the right: a wavepacket which is localized in real space and delocalized (uniform) in k-space. Our production results (Figure C7) use a uniform sampling of the Brillouin zone. While weighting the **k**=Γ region is well motivated by wavepacket arguments (and the Fourier transform of the Argon 4s in real space), and could be used to improve agreement with experiment, the physical justification is here false. Our WDOS calculation scheme is based on the folded band structure and therefore the **k**=Γ region contains folded bands (Figure E2). A weighting of the wavepacket to favor the **k**=Γ region thus is corrupted by the band folding. A proper consideration of wavepacket structure in k-space, and its effect on ET lifetimes, should be performed in the unfolded band structure, which we save for future work. The uniform wavepacket approximation is furthermore valid in the limit of low coverage, where the BZ is small and the wavepacket itself is folded and its structure therefore obscured.

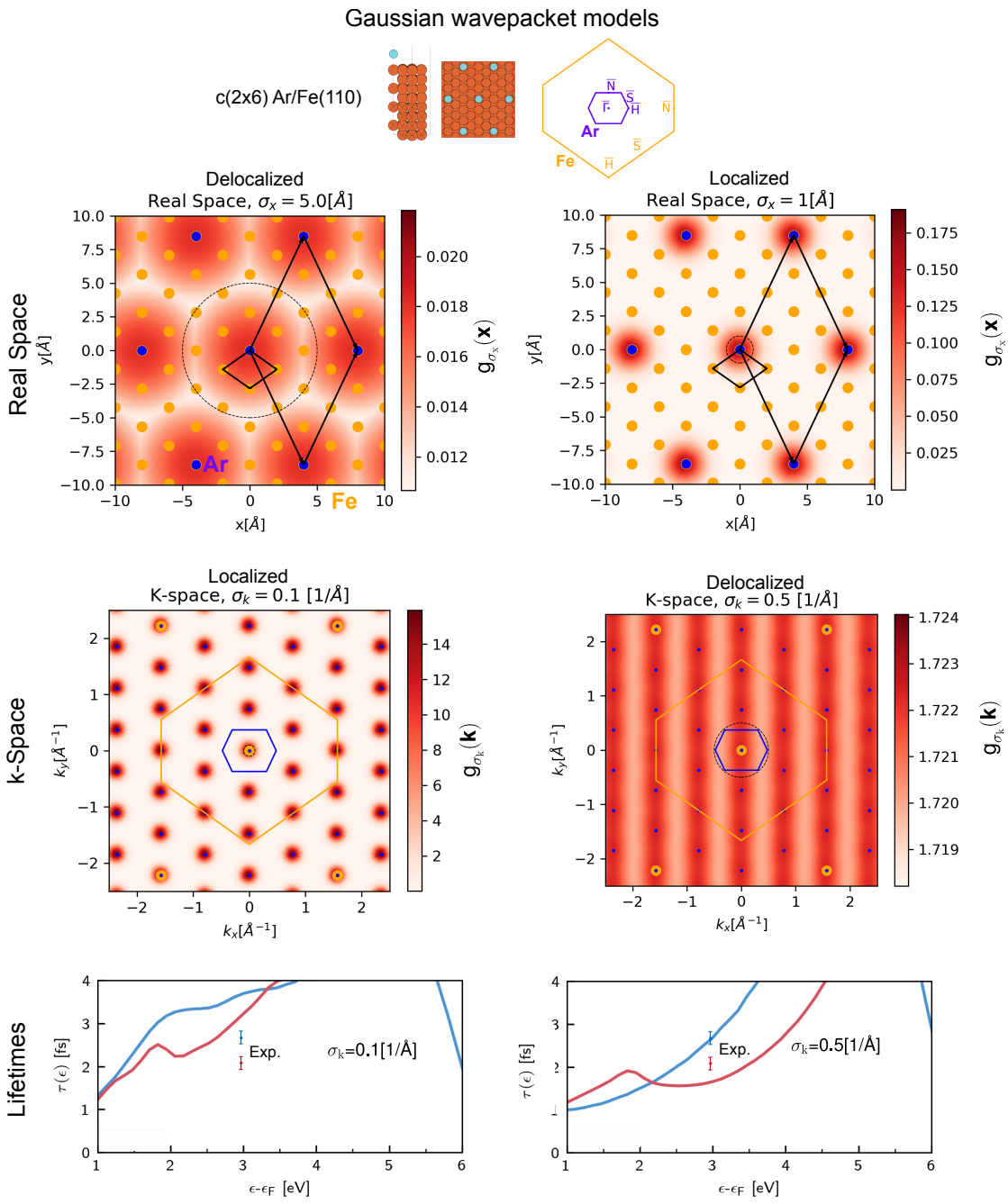

Figure D1: BZ-averaged electron transfer lifetimes are shown under two different Gaussian wavepacket models of the Argon donor state. On the left, a delocalized Gaussian in real-space (localized in k-space). On the right, a localized Gaussian in real-space (uniform in k-space). Further description in text.

E Select Adiabatic Properties

Parts of the following section have been reused with permission from Reference [2] and have been submitted for publication. After they are published, they will be found at The Journal of Chemical Physics.

The suitability of a diabatic representation can be assessed by comparison of its properties, such as the diabatic DOS, to the original adiabatic DOS. For this reason we provide the original adiabatic PDOS of the Ar/Fe(110) system in Figure E1. Adiabatic band structures are also provided, demonstrating band folding and the projected band gap.

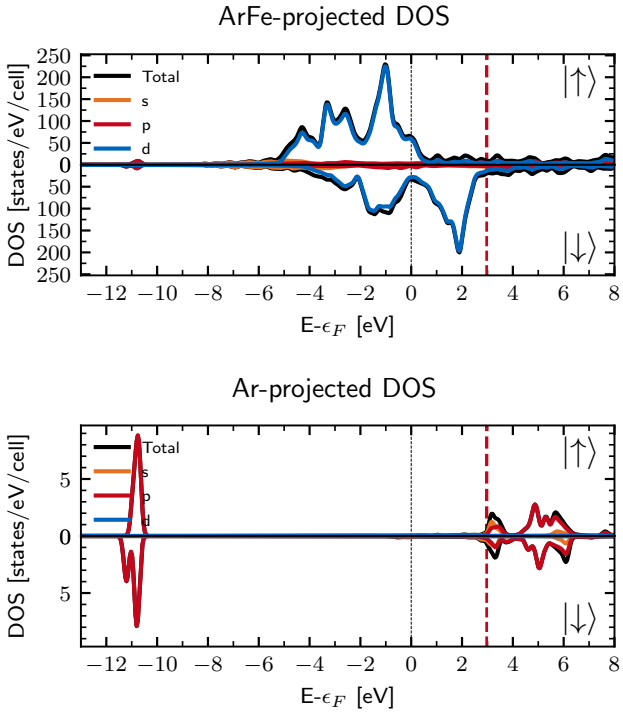

Figure E1: The (conventional) adiabatic projected DOS is shown for the c(2x6) Ar/Fe(110) system with 8 metal layers, containing a Gaussian broadening of 0.1eV, and evaluated on a 3x3x1 k-grid. Upper: projection upon the full system. Lower: the adiabatic PDOS of the Argon atom. The experimental resonance is shown with a red dashed line, corresponding to a 4s-like peak in the Ar-projected DOS (the atom contains a half core-hole). The diabatic DOS, shown in Figure C8, is consistent with this adiabatic PDOS, with the exception of a rogue state beneath the Fermi level. This Figure has been reused with permission from Reference [2] and has been submitted for publication. After it is published, it will be found at The Journal of Chemical Physics.

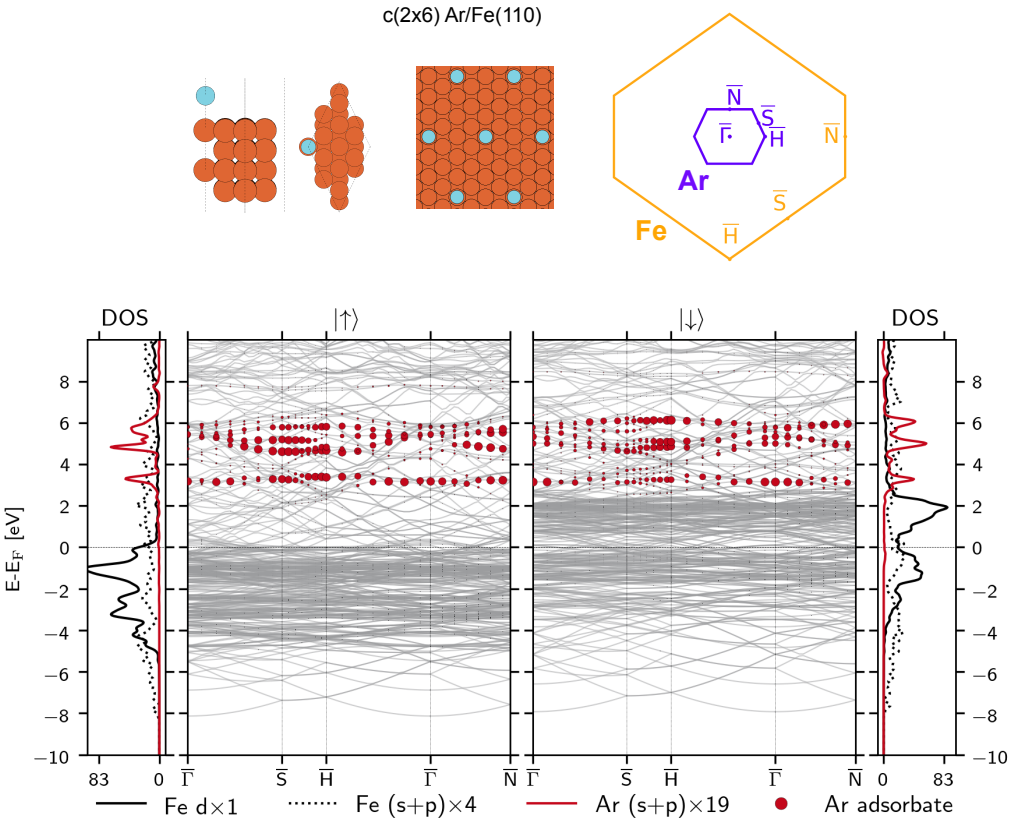

Figure E2: Conventional adiabatic $\mathbf{k}_{||}$ band structure of the c(2x6) Ar/Fe(110) system with 4 metal layers. The band structure is shown for the Argon Brillouin zone, which contains the folded bands of the surface, as well as the adiabatic projected Density of States of the system (with a 0.1eV Gaussian broadening, evaluated on a 3x3x1 k-grid). The Mulliken character of bands associated with the Argon atom is highlighted with red markers, revealing a LUMO resonance band approximately 3 eV above the Fermi level, and minimal dispersion. This corresponds to a peak in the Argon projected-DOS. A half-core hole is present on the Argon. The nested Brillouin zones of the Argon overlayer (blue), which fits inside that of the primitive Fe(110) BCC surface (yellow), is shown at top. The band structure of the primitive surface cells are given in Figure E3. DOS shown in units of [states/eV/cell]. This Figure has been reused with permission from Reference [2] and has been submitted for publication. After it is published, it will be found at The Journal of Chemical Physics.

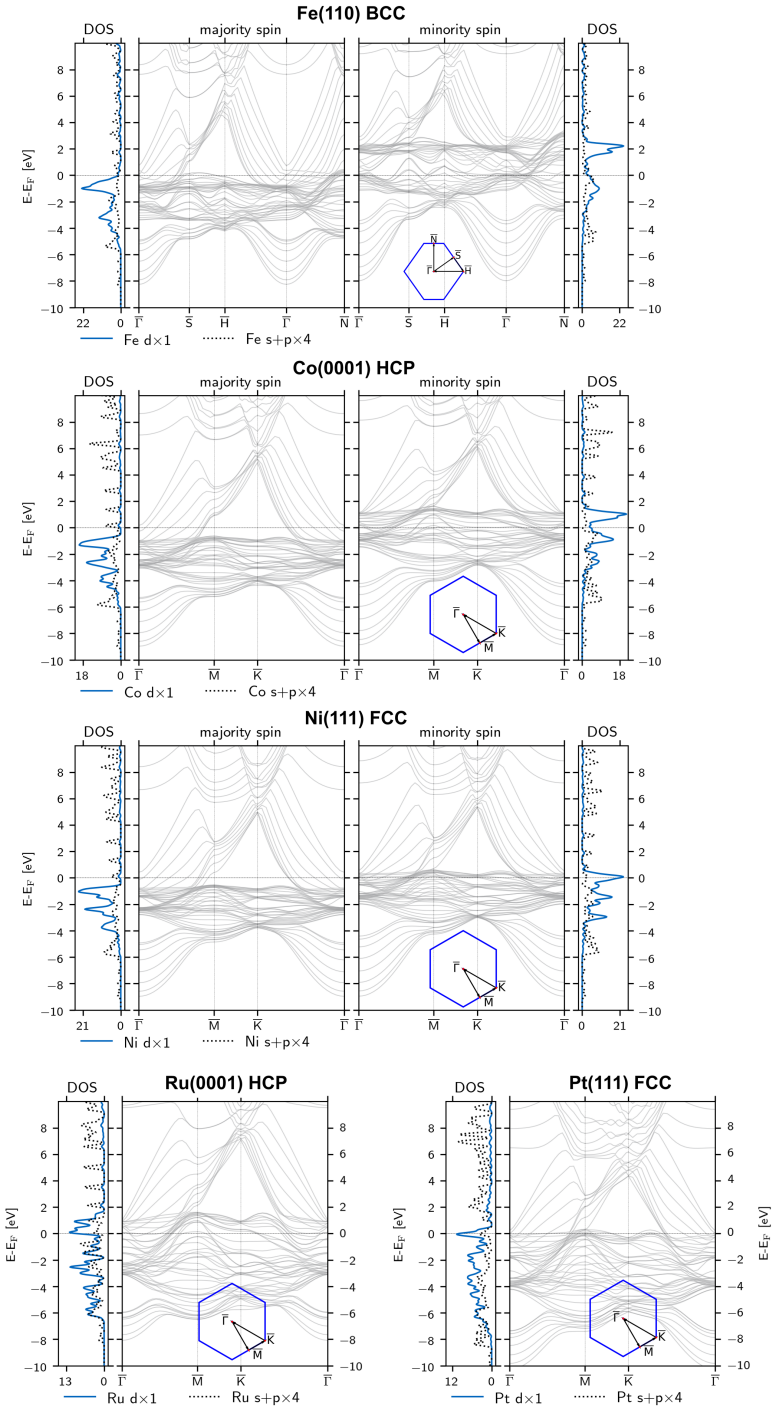

Figure E3: Conventional adiabatic $\mathbf{k}_{||}$ band structure of the primitive cell of the surfaces, revealing projected band gaps at $\mathbf{k}$ = Γ. The extracted band gap onsets are summarized in Table C1. Cells contain 8 layers of metal atoms and the Light Tier1 basis is used. A 3x3x1 k-grid has been used in the projected-DOS calculation, which contains 0.1eV Gaussian broadening. The DOS is in units of [states/eV/cell]. This Figure has been reused with permission from Reference [2] and has been submitted for publication. After it is published, it will be found at The Journal of Chemical Physics.

Bibliography

[1] S. Ghan, C. Kunkel, K. Reuter, and H. Oberhofer, Journal of Chemical Theory and Computation **16**, 7431 (2020) (cit. on pp. i, 3, 4, 6, 7, 20, 24–26, 32, 43–53, 69).

[2] S. Ghan, E. Diesen, C. Kunkel, K. Reuter, and H. Oberhofer, The Journal of Chemical Physics **158**, 234103 (2023) (cit. on pp. i, 7, 8, 31, 35, 56, 59–61, 63, 64, 66, 67, 71–77, 81–89, 91–93, 98–110, 113–115).

[3] P. Kratzer and J. Neugebauer, Frontiers in Chemistry **7**, 1 (2019) (cit. on pp. 1–3, 7, 9, 12, 13).

[4] R. Hoffmann and J.-P. Malrieu, Angewandte Chemie International Edition **59**, 12590 (2020) (cit. on p. 1).

[5] V. L. Deringer, A. L. Tchougreeff, and R. Dronskowski, The Journal of Physical Chemistry A **115**, 5461 (2011) (cit. on pp. 1, 3).

[6] S. Maintz, V. L. Deringer, A. L. Tchougreeff, and R. Dronskowski, Journal of Computational Chemistry **34**, 2557 (2013) (cit. on pp. 1, 3, 4).

[7] S. Maintz, V. L. Deringer, A. L. Tchougréeff, and R. Dronskowski, Journal of Computational Chemistry **37**, 1030 (2016) (cit. on pp. 1–4, 13).

[8] R. S. Mulliken, The Journal of Chemical Physics **23**, 1833 (1955) (cit. on pp. 1–3, 37).

[9] T. Hughbanks and R. Hoffmann, Journal of the American Chemical Society **105**, 3528 (1983) (cit. on pp. 1–3).

[10] R. Hoffmann, *Solids and surfaces, a chemists view of bonding in extended structures* (Wiley-VCH Inc, 1989) (cit. on pp. 1–3, 5).

[11] R. Hoffmann, Rev. Mod. Phys. **60**, 601 (1988) (cit. on pp. 1–3, 5).

[12] R. Dronskowski and P. E. Bloechl, The Journal of Physical Chemistry **97**, 8617 (1993) (cit. on pp. 2–4).

[13] S. Steinberg and R. Dronskowski, Crystals **8**, 10.3390/cryst8050225 (2018) (cit. on pp. 2–4, 13).

[14] B. M. Comer, J. Li, F. Abild-Pedersen, M. Bajdich, and K. T. Winther, The Journal of Physical Chemistry C **126**, 7903 (2022) (cit. on pp. 2, 4).

[15] G. S. Michelitsch and K. Reuter, J. Chem. Phys. **150**, 074104 (2019) (cit. on pp. 2, 57).

[16] M. Kick, K. Reuter, and H. Oberhofer, Journal of Chemical Theory and Computation **15**, 1705 (2019) (cit. on p. 2).

[17] T. Giovannini and H. Koch, Journal of Chemical Theory and Computation **17**, 139 (2021) (cit. on p. 2).
[18] J. Kügel, M. Karolak, A. Krönlein, J. Senkpiel, P.-J. Hsu, G. Sangiovanni, and M. Bode, Phys. Rev. B **91**, 235130 (2015) (cit. on pp. 2, 70).
[19] M. Karolak, T. O. Wehling, F. Lechermann, and A. I. Lichtenstein, Journal of Physics: Condensed Matter **23**, 085601 (2011) (cit. on p. 2).
[20] A. Nilsson and L. G. Pettersson, in *Chemical bonding at surfaces and interfaces*, edited by A. Nilsson, L. G. Pettersson, and J. K. Nørskov (Elsevier, Amsterdam, 2008), pp. 57–142 (cit. on pp. 2, 5).
[21] A. Nilsson and L. G. M. Pettersson, Surface Science Reports **55**, 49 (2004) (cit. on p. 2).
[22] F. L. Hirshfeld, Theoretica chimica acta **44**, 129 (1977) (cit. on p. 3).
[23] G. Henkelman, A. Arnaldsson, and H. Jónsson, Computational Materials Science **36**, 354 (2006) (cit. on p. 3).
[24] I. Kondov, M. Čížek, C. Benesch, H. Wang, and M. Thoss, J. Phys. Chem. C **111**, 11970 (2007) (cit. on pp. 3, 4, 6, 7, 19, 21–23, 25, 54, 55, 69).
[25] J. Li, M. Nilsing, I. Kondov, H. Wang, P. Persson, S. Lunell, and M. Thoss, J. Phys. Chem. C **112**, 12326 (2008) (cit. on pp. 3, 4, 6, 19, 21, 22).
[26] H. Oberhofer, K. Reuter, and J. Blumberger, Chem. Rev. **117**, 10319 (2017) (cit. on pp. 4, 19, 21).
[27] M. Müller, P. M. Echenique, and D. Sánchez-Portal, Journal of Physical Chemistry Letters **11**, 7141 (2020) (cit. on pp. 4, 6, 7, 57, 59, 80, 90, 105, 106).
[28] D. Sánchez-Portal, D. Menzel, and P. M. Echenique, Phys. Rev. B **76**, 235406 (2007) (cit. on pp. 4, 6–8, 57–59, 67, 68, 70, 80, 90).
[29] M. Pastore and F. De Angelis, Journal of the American Chemical Society **137**, 5798 (2015) (cit. on pp. 4, 6).
[30] M. P. Bahlke, M. Schneeberger, and C. Herrmann, The Journal of Chemical Physics **154**, 144108 (2021) (cit. on pp. 4, 16, 70).
[31] M. P. Bahlke, P. Wahl, L. Diekhöner, and C. Herrmann, Journal of Applied Physics **125**, 142910 (2019) (cit. on p. 4).
[32] T. Van Voorhis, T. Kowalczyk, B. Kaduk, L.-P. Wang, C.-L. Cheng, and Q. Wu, Annu. Rev. Phys. Chem. **61**, 149 (2010) (cit. on pp. 4, 6, 19, 21, 53, 54).
[33] D. Sánchez-Portal, Progress in Surface Science **82**, 313 (2007) (cit. on pp. 4, 6–8).
[34] M. D. Newton, Chem. Rev. **91**, 767 (1991) (cit. on pp. 5, 21).
[35] R. J. Cave and M. D. Newton, Chem. Phys. Lett. **249**, 15 (1996) (cit. on p. 5).
[36] R. J. Cave and M. D. Newton, J. Chem. Phys. **106**, 9213 (1997) (cit. on pp. 5, 19, 54).
[37] J. K. Nørskov, The Journal of Chemical Physics **90**, 7461 (1989) (cit. on pp. 5, 6).
[38] B. Hammer and J. K. Norskov, Nature **376**, 238 (1995) (cit. on pp. 5, 6).
[39] B. Hammer and J. Nørskov, Surface Science **343**, 211 (1995) (cit. on pp. 5, 6, 70).
[40] E. Santos, P. Quaino, and W. Schmickler, Phys. Chem. Chem. Phys. **14**, 11224 (2012) (cit. on p. 5).
[41] B. N. J. Persson and M. Persson, Solid State Communications **36**, 175 (1980) (cit. on p. 5).

[42] P. Saalfrank, Chemical Reviews **106**, 4116 (2006) (cit. on p. 5).
[43] D. Menzel, J. Chem. Phys. **137**, 091702 (2012) (cit. on p. 5).
[44] D. Menzel and R. Gomer, The Journal of Chemical Physics **41**, 3311 (1964) (cit. on p. 5).
[45] J. A. Misewich, T. F. Heinz, and D. M. Newns, Phys. Rev. Lett. **68**, 3737 (1992) (cit. on p. 5).
[46] J. Bardeen, Phys. Rev. Lett. **6**, 57 (1961) (cit. on p. 5).
[47] J. Tersoff and D. R. Hamann, Phys. Rev. B **31**, 805 (1985) (cit. on pp. 5, 37, 70, 104).
[48] J. Tersoff and D. R. Hamann, Phys. Rev. Lett. **50**, 1998 (1983) (cit. on p. 5).
[49] C. J. Chen, Phys. Rev. B **42**, 8841 (1990) (cit. on pp. 5, 37, 68, 70).
[50] C. J. Chen, Phys. Rev. Lett. **69**, 1656 (1992) (cit. on pp. 5, 68, 70, 103, 104).
[51] C. J. Chen, *Introduction to Scanning Tunneling Microscopy* (Oxford University Press, Sept. 2007) (cit. on pp. 5, 68, 70).
[52] D. Menzel, Chem. Soc. Rev. **37**, 2212 (2008) (cit. on pp. 5, 67).
[53] D. Newns, Phys. Rev. **178**, 1123 (1969) (cit. on pp. 5, 6, 14, 31, 36, 40, 69).
[54] F. Abild-Pedersen, J. Greeley, F. Studt, J. Rossmeisl, T. R. Munter, P. G. Moses, E. Skúlason, T. Bligaard, and J. K. Nørskov, Phys. Rev. Lett. **99**, 016105 (2007) (cit. on pp. 5, 6).
[55] J. K. Nørskov, T. Bligaard, B. Hvolbæk, F. Abild-Pedersen, I. Chorkendorff, and C. H. Christensen, Chem. Soc. Rev. **37**, 2163 (2008) (cit. on pp. 5, 16).
[56] S. Saini, J. Halldin Stenlid, and F. Abild-Pedersen, npj Computational Materials **8**, 163 (2022) (cit. on p. 5).
[57] T. Bligaard and J. Nørskov, in *Chemical bonding at surfaces and interfaces*, edited by A. Nilsson, L. G. Pettersson, and J. K. Nørskov (Elsevier, Amsterdam, 2008), pp. 255–321 (cit. on pp. 5, 16, 17).
[58] A. Gross, *Theoretical surface science, a microscopic perspective* (Springer, 2003) (cit. on pp. 5, 14, 36, 40).
[59] A. Cao and J. K. Nørskov, ACS Catalysis **13**, 3456 (2023) (cit. on pp. 5, 6).
[60] Y. Ogura, K. Sato, S.-i. Miyahara, Y. Kawano, T. Toriyama, T. Yamamoto, S. Matsumura, S. Hosokawa, and K. Nagaoka, Chem. Sci. **9**, 2230 (2018) (cit. on p. 5).
[61] M. Hattori, S. Iijima, T. Nakao, H. Hosono, and M. Hara, Nature Communications **11**, 2001 (2020) (cit. on p. 5).
[62] L. Xu, K. G. Papanikolaou, B. A. J. Lechner, L. Je, G. A. Somorjai, M. Salmeron, and M. Mavrikakis, Science **380**, 70 (2023) (cit. on p. 5).
[63] A. Vojvodic, J. K. Nørskov, and F. Abild-Pedersen, Topics in Catalysis **57**, 25 (2014) (cit. on pp. 5, 6, 16, 70).
[64] A. Cao, V. J. Bukas, V. Shadravan, Z. Wang, H. Li, J. Kibsgaard, I. Chorkendorff, and J. K. Nørskov, Nature Communications **13**, 2382 (2022) (cit. on pp. 5, 6).
[65] S. Vijay, G. Kastlunger, K. Chan, and J. K. Nørskov, J. Chem. Phys. **156**, 231102 (2022) (cit. on pp. 5, 6).
[66] D.-Q. Liu, M. Kang, D. Perry, C.-H. Chen, G. West, X. Xia, S. Chaudhuri, Z. P. L. Laker, N. R. Wilson, G. N. Meloni, M. M. Melander, R. J. Maurer, and P. R. Unwin, Nature Communications **12**, 7110 (2021) (cit. on pp. 5, 6).

[67] S. Bhattacharjee, U. V. Waghmare, and S.-C. Lee, Scientific Reports **6**, 35916 (2016) (cit. on p. 5).
[68] Q. Wu and T. Van Voorhis, J. Chem. Phys. **125**, 164105 (2006) (cit. on pp. 6, 21).
[69] K. Senthilkumar, F. C. Grozema, F. M. Bickelhaupt, and L. D. A. Siebbeles, J. Chem. Phys. **119**, 9809 (2003) (cit. on pp. 6, 21, 29, 43).
[70] C. Schober, K. Reuter, and H. Oberhofer, J. Chem. Phys. **144**, 054103 (2016) (cit. on pp. 6, 19, 21, 29, 43, 44, 52, 53).
[71] Z. Futera and J. Blumberger, J. Phys. Chem. C **121**, 19677 (2017) (cit. on pp. 6, 8, 19, 21, 22, 43, 69).
[72] J. Li, I. Kondov, H. Wang, and M. Thoss, J. Phys. Chem. C **114**, 18481 (2010) (cit. on pp. 6, 19, 21, 22).
[73] J. Li, H. Wang, P. Persson, and M. Thoss, J. Chem. Phys. **137**, 22A529 (2012) (cit. on pp. 6, 19).
[74] A. Kubas, F. Hoffmann, A. Heck, H. Oberhofer, M. Elstner, and J. Blumberger, J. Chem. Phys. **140**, 104105 (2014) (cit. on pp. 6, 7, 20, 21, 24, 26, 43, 47, 69).
[75] A. Kubas, F. Gajdos, A. Heck, H. Oberhofer, M. Elstner, and J. Blumberger, Phys. Chem. Chem. Phys. **17**, 14342 (2015) (cit. on pp. 6, 50).
[76] C.-P. Hsu and R. A. Marcus, The Journal of Chemical Physics **106**, 584 (1997) (cit. on p. 6).
[77] A. G. Borisov, J. P. Gauyacq, E. V. Chulkov, V. M. Silkin, and P. M. Echenique, Phys. Rev. B **65**, 235434 (2002) (cit. on pp. 6, 7).
[78] A. Föhlisch, P. Feulner, F. Hennies, A. Fink, D. Menzel, D. Sánchez-Portal, P. M Echenique, and W. Wurth, Nature **436**, 373 (2005) (cit. on p. 6).
[79] W. Wurth and D. Menzel, Chemical Physics **251**, 141 (2000) (cit. on pp. 7, 56, 59, 63, 67, 93).
[80] A. Föhlisch, D. Menzel, P. Feulner, M. Ecker, R. Weimar, K. Kostov, G. Tyuliev, S. Lizzit, R. Larciprete, F. Hennies, and W. Wurth, Chemical Physics **289**, 107 (2003) (cit. on p. 7).
[81] J. Gauyacq, A. Borisov, and G. RaSeev, Surface Science **490**, 99 (2001) (cit. on p. 7).
[82] S. Vijayalakshmi, A. Föhlisch, F. Hennies, A. Pietzsch, M. Nagasono, W. Wurth, A. Borisov, and J. Gauyacq, Chem. Phys. Lett. **427**, 91 (2006) (cit. on pp. 7, 32, 57, 59, 67, 80).
[83] J. P. Gauyacq and A. G. Borisov, Phys. Rev. B **69**, 235408 (2004) (cit. on pp. 7, 57, 67, 80).
[84] W. Kohn and L. J. Sham, Phys. Rev. **140**, A1133 (1965) (cit. on p. 9).
[85] P. Hohenberg and W. Kohn, Phys. Rev. **136**, B864 (1964) (cit. on p. 9).
[86] R. Stowasser and R. Hoffmann, Journal of the American Chemical Society **121**, 3414 (1999) (cit. on pp. 9, 13).
[87] J. P. Perdew and S. Kurth, "Density functionals for non-relativistic coulomb systems in the new century," in *A primer in density functional theory*, edited by C. Fiolhais, F. Nogueira, and M. A. L. Marques (Springer Berlin Heidelberg, Berlin, Heidelberg, 2003), pp. 1–55 (cit. on p. 9).

[88] J. P. Perdew, K. Burke, and M. Ernzerhof, Phys. Rev. Lett. **77**, 3865 (1996) (cit. on pp. 10, 43, 57).
[89] V. Blum, R. Gehrke, F. Hanke, P. Havu, V. Havu, X. Ren, K. Reuter, and M. Scheffler, Computer Physics Communications **180**, 2175 (2009) (cit. on pp. 11–13, 37, 39, 40, 43, 57).
[90] I. Y. Zhang, X. Ren, P. Rinke, V. Blum, and M. Scheffler, New J. Phys. **15**, 123033 (2013) (cit. on pp. 11, 12, 43, 57).
[91] H. J. Monkhorst and J. D. Pack, Phys. Rev. B **13**, 5188 (1976) (cit. on pp. 12, 36, 39, 57).
[92] G. Aissing and H. J. Monkhorst, Int. J. Quantum Chem. **43**, 733 (1992) (cit. on pp. 12, 39).
[93] E. Gull, A. J. Millis, A. I. Lichtenstein, A. N. Rubtsov, M. Troyer, and P. Werner, Rev. Mod. Phys. **83**, 349 (2011) (cit. on p. 14).
[94] H. Shinaoka, E. Gull, and P. Werner, Computer Physics Communications **215**, 128 (2017) (cit. on p. 14).
[95] P. W. Anderson, Phys. Rev. **124**, 41 (1961) (cit. on p. 14).
[96] A. Nilsson, L. G. M. Pettersson, B. Hammer, T. Bligaard, C. H. Christensen, and J. K. Nørskov, Catalysis Letters **100**, 111 (2005) (cit. on p. 15).
[97] R. E. Warburton, A. V. Soudackov, and S. Hammes-Schiffer, Chemical Reviews **122**, 10599 (2022) (cit. on pp. 16, 36).
[98] E. F. Valeev, V. Coropceanu, D. A. da Silva Filho, S. Salman, and J.-L. Brédas, J. Am. Chem. Soc. **128**, 9882 (2006) (cit. on pp. 21, 29, 32, 45).
[99] B. Baumeier, J. Kirkpatrick, and D. Andrienko, Phys. Chem. Chem. Phys. **12**, 11103 (2010) (cit. on pp. 21, 29, 32, 44).
[100] J. Li, H. Li, P. Winget, and J.-L. Bredas, J. Phys. Chem. C **119**, 18843 (2015) (cit. on pp. 21, 22).
[101] Y. Mao, A. Montoya-Castillo, and T. E. Markland, J. Chem. Phys. **151**, 164114 (2019) (cit. on pp. 21, 22, 52).
[102] A. Biancardi, S. C. Martin, C. Liss, and M. Caricato, J. Chem. Theory Comput. **13**, 4154 (2017) (cit. on p. 21).
[103] C.-H. Yang, C. Yam, and H. Wang, Phys. Chem. Chem. Phys. **20**, 2571 (2018) (cit. on pp. 21, 22, 52, 55).
[104] H. Feshbach, Annals of Physics **19**, 287 (1962) (cit. on p. 22).
[105] W. Domcke, Physics Reports **208**, 97 (1991) (cit. on p. 22).
[106] V. Prucker, O. Rubio-Pons, M. Bockstedte, H. Wang, P. B. Coto, and M. Thoss, J. Phys. Chem. C **117**, 25334 (2013) (cit. on p. 22).
[107] I. Mayer, Int. J. Quantum Chem. **90**, 63 (2002) (cit. on p. 22).
[108] P.-O. Löwdin, J. Chem. Phys. **18**, 365 (1950) (cit. on pp. 22, 27, 32).
[109] T. H. Dunning, J. Chem. Phys. **90**, 1007 (1989) (cit. on pp. 24, 43).
[110] T. B. Grimley, Journal of Physics C: Solid State Physics **3**, 1934 (1970) (cit. on p. 32).
[111] C. Kittel and C.-y. Fong, *Quantum theory of solids* (Wiley, 1987) (cit. on p. 36).
[112] S. Gosavi and R. A. Marcus, Journal of Physical Chemistry B **104**, 2067 (2000) (cit. on p. 36).

[113] E. Fermi, *Nuclear physics: a course given by enrico fermi at the university of chicago* (University of Chicago Press, 1950) (cit. on p. 37).
[114] A. D. Becke, J. Chem. Phys. **98**, 5648 (1993) (cit. on p. 43).
[115] J. P. Perdew, M. Ernzerhof, and K. Burke, J. Chem. Phys. **105**, 9982 (1996) (cit. on p. 43).
[116] C. Adamo and V. Barone, J. Chem. Phys. **110**, 6158 (1999) (cit. on p. 43).
[117] Z.-Q. You, Y.-C. Hung, and C.-P. Hsu, J. Phys. Chem. B **119**, 7480 (2015) (cit. on pp. 43, 44, 52).
[118] L. Gallandi, N. Marom, P. Rinke, and T. Körzdörfer, J. Chem. Theory Comput. **12**, 605 (2016) (cit. on pp. 43, 44, 52).
[119] J. Spencer, L. Scalfi, A. Carof, and J. Blumberger, Faraday Discuss. **195**, 215 (2016) (cit. on p. 43).
[120] C. Kunkel, C. Schober, J. T. Margraf, K. Reuter, and H. Oberhofer, Chem. Mater. **31**, 969 (2019) (cit. on p. 43).
[121] O. Lamiel-Garcia, K. C. Ko, J. Y. Lee, S. T. Bromley, and F. Illas, J. Chem. Theory Comput. **13**, 1785 (2017) (cit. on p. 43).
[122] C. R. Harris, K. J. Millman, S. J. van der Walt, R. Gommers, P. Virtanen, D. Cournapeau, E. Wieser, J. Taylor, S. Berg, N. J. Smith, R. Kern, M. Picus, S. Hoyer, M. H. van Kerkwijk, M. Brett, A. Haldane, J. F. del R'ıo, M. Wiebe, P. Peterson, P. G'erard-Marchant, K. Sheppard, T. Reddy, W. Weckesser, H. Abbasi, C. Gohlke, and T. E. Oliphant, Nature **585**, 357 (2020) (cit. on p. 44).
[123] P. Virtanen, R. Gommers, T. E. Oliphant, M. Haberland, T. Reddy, D. Cournapeau, E. Burovski, P. Peterson, W. Weckesser, J. Bright, S. J. van der Walt, M. Brett, J. Wilson, K. J. Millman, N. Mayorov, A. R. J. Nelson, E. Jones, R. Kern, E. Larson, C. J. Carey, İ. Polat, Y. Feng, E. W. Moore, J. VanderPlas, D. Laxalde, J. Perktold, R. Cimrman, I. Henriksen, E. A. Quintero, C. R. Harris, A. M. Archibald, A. H. Ribeiro, F. Pedregosa, P. van Mulbregt, A. Vijaykumar, A. P. Bardelli, A. Rothberg, A. Hilboll, A. Kloeckner, A. Scopatz, A. Lee, A. Rokem, C. N. Woods, C. Fulton, C. Masson, C. Häggström, C. Fitzgerald, D. A. Nicholson, D. R. Hagen, D. V. Pasechnik, E. Olivetti, E. Martin, E. Wieser, F. Silva, F. Lenders, F. Wilhelm, G. Young, G. A. Price, G.-L. Ingold, G. E. Allen, G. R. Lee, H. Audren, I. Probst, J. P. Dietrich, J. Silterra, J. T. Webber, J. Slavič, J. Nothman, J. Buchner, J. Kulick, J. L. Schönberger, J. V. de Miranda Cardoso, J. Reimer, J. Harrington, J. L. C. Rodríguez, J. Nunez-Iglesias, J. Kuczynski, K. Tritz, M. Thoma, M. Newville, M. Kümmerer, M. Bolingbroke, M. Tartre, M. Pak, N. J. Smith, N. Nowaczyk, N. Shebanov, O. Pavlyk, P. A. Brodtkorb, P. Lee, R. T. McGibbon, R. Feldbauer, S. Lewis, S. Tygier, S. Sievert, S. Vigna, S. Peterson, S. More, T. Pudlik, T. Oshima, T. J. Pingel, T. P. Robitaille, T. Spura, T. R. Jones, T. Cera, T. Leslie, T. Zito, T. Krauss, U. Upadhyay, Y. O. Halchenko, and Y. Vázquez-Baeza, Nat. Methods. **17**, 261 (2020) (cit. on pp. 44, 57).
[124] A. A. Voityuk, A. J. Stasyuk, and S. F. Vyboishchikov, Phys. Chem. Chem. Phys. **20**, 23328 (2018) (cit. on p. 47).
[125] D. Hait and M. Head-Gordon, J. Phys. Chem. Lett. **9**, 6280 (2018) (cit. on p. 49).
[126] A. J. Cohen, P. Mori-Sánchez, and W. Yang, Science **321**, 792 (2008) (cit. on p. 49).

[127] H. Sun, S. Ryno, C. Zhong, M. K. Ravva, Z. Sun, T. Körzdörfer, and J.-L. Bredas, J. Chem. Theory Comput. **12**, 2906 (2016) (cit. on p. 52).
[128] M. A. Rohrdanz, K. M. Martins, and J. M. Herbert, J. Chem. Phys. **130**, 054112 (2009) (cit. on p. 52).
[129] O. A. Vydrov, J. Heyd, A. V. Krukau, and G. E. Scuseria, J. Chem. Phys. **125**, 074106 (2006) (cit. on p. 52).
[130] L. Gallandi and T. Körzdörfer, J. Chem. Theory Comput. **11**, 5391 (2015) (cit. on p. 52).
[131] T. Pacher, C. A. Mead, L. S. Cederbaum, and H. Köppel, J. Chem. Phys. **91**, 7057 (1989) (cit. on p. 54).
[132] L. S. Cederbaum, H. Köppel, and W. Domcke, Int. J. Quantum Chem. **20**, 251 (1981) (cit. on p. 54).
[133] T. Pacher, L. S. Cederbaum, and H. Köppel, J. Chem. Phys. **89**, 7367 (1988) (cit. on p. 54).
[134] T. Pacher, L. S. Cederbaum, and H. Köppel, Adv. Chem. Phys., 293 (2007) (cit. on p. 54).
[135] T. Pacher, H. Köppel, and L. S. Cederbaum, J. Chem. Phys. **95**, 6668 (1991) (cit. on p. 54).
[136] F. Blobner, R. Han, A. Kim, W. Wurth, and P. Feulner, Phys. Rev. Lett. **112**, 086801 (2014) (cit. on pp. 56, 58, 59, 63, 76, 84, 85, 88, 93).
[137] O. Karis, A. Nilsson, M. Weinelt, T. Wiell, C. Puglia, N. Wassdahl, N. Mårtensson, M. Samant, and J. Stöhr, Phys. Rev. Lett. **76**, 1380 (1996) (cit. on pp. 56, 59, 63, 67, 93).
[138] A. Tkatchenko and M. Scheffler, Phys. Rev. Lett. **102**, 073005 (2009) (cit. on p. 57).
[139] B. P. Pritchard, D. Altarawy, B. Didier, T. D. Gibson, and T. L. Windus, Journal of Chemical Information and Modeling **59**, 4814 (2019) (cit. on p. 57).
[140] M. Leetmaa, M. Ljungberg, A. Lyubartsev, A. Nilsson, and L. Pettersson, Journal of Electron Spectroscopy and Related Phenomena **177**, 135 (2010) (cit. on p. 57).
[141] T. Sundermann, N. Müller, U. Heinzmann, W. Wurth, J. Bauer, R. Han, A. Kim, D. Menzel, and P. Feulner, Surface Science **643**, 190 (2016) (cit. on p. 59).
[142] C. Keller, M. Stichler, G. Comelli, F. Esch, S. Lizzit, W. Wurth, and D. Menzel, Phys. Rev. Lett. **80**, 1774 (1998) (cit. on p. 67).
[143] C. Keller, M. Stichler, G. Comelli, F. Esch, S. Lizzit, D. Menzel, and W. Wurth, Phys. Rev. B **57**, 11951 (1998) (cit. on p. 67).
[144] L. Gross, N. Moll, F. Mohn, A. Curioni, G. Meyer, F. Hanke, and M. Persson, Phys. Rev. Lett. **107**, 086101 (2011) (cit. on p. 68).
[145] F. Gajdos, S. Valner, F. Hoffmann, J. Spencer, M. Breuer, A. Kubas, M. Dupuis, and J. Blumberger, Journal of Chemical Theory and Computation **10**, 4653 (2014) (cit. on p. 97).

Acknowledgments

Many thanks go to Thao for keeping me human, to my band The Munyks for their patience, to Isar Funk Sessions for the inspiration, to Martin for the LaTeX template, to my family for their support from afar, and finally to my numerous lovely colleagues for the vibes over the years.

Berlin, May 2023

Simiam Ghan